UNIVERSITÀ
DI PARMA

UNIVERSITÁ DEGLI STUDI DI PARMA
DIPARTIMENTIO DI INGEGNERIA E ARCHITETTURA

DOTTORATO DI RICERCA IN
INGEGNERIA CIVILE

CICLO XXXV

Predictive model for Carbonation Corrosion Phenomena in Reinforced Concrete Elements

Coordinatore:
Chiar.mo Prof. Andrea SPAGNOLI

Tutore:
Chiar.mo Prof. Francesco FREDDI

Dottorando:
Lorenzo MINGAZZI

Abstract

Deterioration and damage of concrete present important threats to the integrity and serviceability of reinforced concrete structures. Environmental phenomena such as intake of carbon dioxide, chloride and sulphate attacks, freeze-thaw cycles and alkali-aggregate reactions are degradation phenomena which negatively impact the durability of the material [1, 2]. Being the most commonly used construction material worldwide [3], it became evident with time that more in depth investigation of the environmental threats affecting concrete elements were required.

To this extent, in recent years non-destructive structural health monitoring systems became more and more relevant as they provide valuable information on the actual condition of the structure [4, 5, 6]. Additionally, the data collected from the monitoring systems can be eventually employed as a reference dataset to develop forecasting models applicable in the organization of long-term maintenance schedule for an effective and efficient upkeep of reinforced concrete structures.

Within this context, the present work aims to expand the computational model previously presented in [7] which describes the degradation of reinforced concrete elements affected by carbonation corrosion phenomena.

Starting from the environmental condition, the carbonation process of the concrete cover is described using a system of coupled transport-diffusion-reaction partial differential equations. Here, changes in the moisture content of the specimen are described and their effects on the rate of carbon dioxide diffusion and reaction with the calcium hydroxide from the cement paste are considered [8, 9]. Due to the carbonation process, calcium carbonate is formed and the material properties of the concrete changes. Moreover, a key aspect of the concrete carbonation process is the change in the pH of the pore water to more neutral values.

Once the carbonation front reaches the concrete near the reinforcement bars, the lower pH value causes the dissolution of the steel protective passive layer, triggering the start of the corrosion process which results in the formation of rust deposits over the rebar surface. Two different types of corrosion mechanism are considered: a pure interfacial reaction step which is governed only by the oxygen concentration at the rebar surface, and a pure diffusion step which is observed when rust deposits are formed and only a limited supply of oxygen reaches the rebar, thus creating a limiting value on the corrosion current density [10]. The corrosion current density is evaluated via the electrochemical kinetics equations which allow to determine the iron dissolution and oxygen consumption rates starting from the available reactant concentrations at the metal surface [11]. Eventually, the amount of rust formed on the rebar is evaluated accordingly to the iron dissolution rate.

As rust deposits form over the rebar surface, overpressures are generated on the surrounding concrete. Once the tensile resistance of concrete is reached, cracks nucleate and propagate until cracking and spalling of the cover are observed. The rupture of the concrete cover is modelled using the phase field method for brittle fracture due to its capability

to accurately reproduce the traction-compression anisotropy rupture behaviour of concrete providing accurate results [12, 13].

The developed model set a starting point as a tool for the prediction of the degradation process of the carbonation induced corrosion cracking of reinforced concrete. The numerical nature of the model allows to simulate a wide variety of environmental effects as well as different concrete compositions. The various processes of the model are firstly validated against results from the literature and the complete model is used to simulate the degradation process of representative reinforced concrete elements.

Contents

List of Figures

List of Tables

Chapter 1

Introduction

1.1 Degradation of concrete structures

Reinforced concrete represents the most common material used for building worldwide [3]. The union of steel and concrete allowed to obtain a material which presents high performances, overcoming the weaknesses of concrete and steel when used individually. In fact, the poor performances of concrete to resist tensile and shear stresses are greatly enhanced by the presence of embedded steel, while at the same time, concrete provides protection to the steel bars from various types of degradation mechanism [19, 20].

Figure 1.1: Usage of reinforced concrete in buildings. A) National Museum of Western Art by Le Corbusier, Tokyo, Japan; B) The Royal National Theatre by Denys Lasdun, London, United Kingdom; C) Suzhou Intangible Cultural Heritage Museum by Vector Architects, Suzhou, China; D) Torre Velasca by Studio BBPR, Milan, Italy.

This synergistic interaction between the two materials made it so that reinforced concrete

was considered an almost eternal material, up until the 1970s [21]. However, it became apparent with time that reinforced concrete structures present a limited service life due to the effects of the environmental threats affecting them. Therefore, compliance to the current standards [22, 23] during the design and manufacturing processes of reinforced concrete elements is a key factor to obtain adequate protection to steel bars for a period of time which greatly exceeds the typical minimum required service life for ordinary structures.

The main responsible for protection of steel rebars in a reinforced concrete element is the concrete cover. It is defined as the least distance between the surface of embedded reinforcement and the outer surface of concrete. The concrete cover must have a minimal thickness to ensure the formation of a proper bond between concrete and steel as well as to provide sufficient protection to steel from various hazards affecting the material. Its design should account for various harmful degradation processes such as freeze and thaw cycles [24], attack by acid and pure water [25], sulphate attack [26, 27], alkali silica reaction [28], chloride attack [29] and carbonation [30, 31]. All of the above mentioned deterioration processes, compromise the protection that concrete provides to rebars thus causing corrosion of steel bars, which is the main cause of durability failure in reinforced concrete structures [32]. In fact, rebar corrosion is responsible for highly dangerous phenomena such as loss of the bond at steel-concrete interface, cracking and/or spalling of concrete cover and lower ductility. All of this mechanisms lead to a significant reduction of the bearing capacity of a reinforced concrete structure, raising serious safety issues as the structural integrity of the construction is compromised [33].

a) b)

Figure 1.2: Example of corrosion of rebars in reinforced concrete structures. a) examples of concrete spalling from [14]; b) concrete cover spalling induced by corrosion of rebars from [15]

1.2 Corrosion of steel in concrete

Concrete presents an highly alkaline environment (pH $\sim$ 13) which forms during the hydration process of the cement. In this setting, steel produces stable compounds of iron oxydes and hydroxides which form a passive layer of very limited thickness (few nanometers) that protects steel from corrosion. While mechanical damage to the steel bars do not affect

the passive layer, presence of chloride ions and/or carbonation of concrete cause its dissolution leaving rebars susceptible to corrosion [34, 21].

Based on the status of the passive layer, is possible to distinguish two main stages of the service life of a reinforced concrete structure as proposed by [16] and schematized in fig. 1.3: a first initiation stage followed by a propagation stage.

1 - The initiation stage considers the time required for depassivation of rebar. Duration of the initiation phase is heavily tied to the depth of concrete cover, which should be designed accounting for environmental threats that could affect the structure. Concentration, period of exposure and the rate of ingress of aggressive agents are also fundamental aspects that affects the duration of this phase.

2- The propagation stage considers the time that elapses between the start of the corrosion process and the end of the service life of the structure.

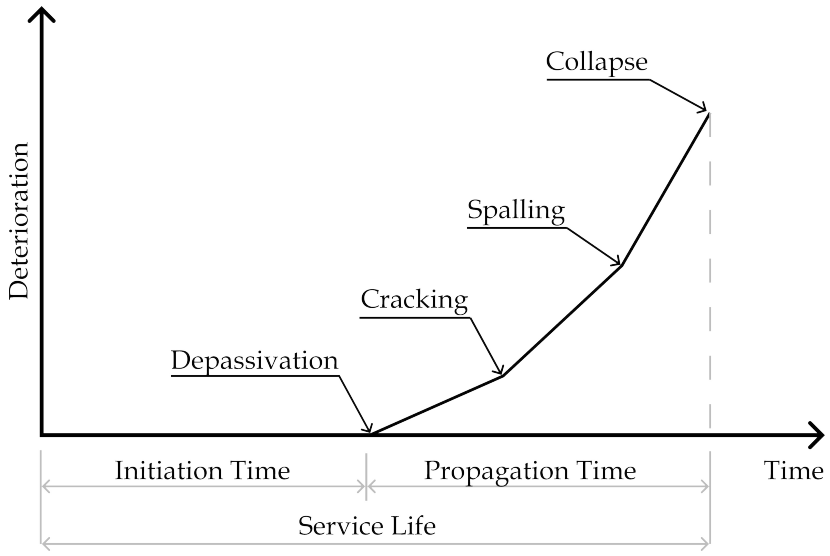

Figure 1.3: Initiation and propagation phases and the corresponding degradation stages in reinforced concrete from [16]

.

Based on the aggressive agent, the depassivation process of steel rebars and the type of corrosion process changes. In a carbonated concrete, the reaction between the carbon dioxide with the alkaline elements of cement paste cause the pH of pore water to drop to more neutral values where the passive layer is no longer stable. This depassivation process affects the whole surface of steel rebar in contact with the carbonated concrete, causing a generalised corrosion process [35, 36]. On the other hand, chloride ions penetration through concrete cover cause the depassivation of rebars if a critical concentration is reached over the metal surface. Therefore, due to the spatial differences in the chloride ions concentration, pitting corrosion processes are observed where severe and localised corrosion affect the rebars [37, 38].

1.3 Carbonation induced corrosion

Focus is put on the carbonation corrosion phenomena affecting reinforced concrete elements. This degradation process is currently receiving increasing attention due to the constant increase of carbon dioxide concentration in the atmosphere [39].

Carbonation of concrete is a chemical process which involves the diffusion of carbon dioxide (CO_2) in the environment through the concrete pores and its reactions with elements of the cement paste. The initial step of the carbonation mechanism consists in the intake and diffusion of carbon dioxide through concrete pores. As the CO_2 diffuses within concrete, it dissolves in the pore water forming an acidic solution that can react with the solid hydration products of the cement paste. For a standard Ordinary Portland Cement (OPC) concrete [40], the main hydrate in cement paste reacting with carbon dioxide is calcium hydroxide. The following reaction, that takes place in the concrete pore water, defines the carbonation process

$$CO_2 + Ca(OH)_2 \rightarrow CaCO_3 + H_2O \tag{1.1}$$

Carbonation rate is affected by numerous factors. Carbon dioxide concentration heavily impacts the rate at which the carbonation of concrete is observed. An increase of the carbonation rate is associated with the increase of carbon dioxide content in the external air. Laboratory tests have shown that one week exposure of the specimen in an accelerated carbonation setting at 4% of CO_2 cause the same carbonation penetration as one year in a natural environment [41, 42]. Another important factor controlling the rate of the carbonation process is the moisture content in the concrete pores. Since the carbonation of concrete involves an initial diffusion stage, presence of water in the concrete pores hinders the diffusion of the gaseous CO_2. However, water is required for the carbonation reaction of eq. 1.1 to take place. As a result, carbonation rates are reported to increase noticeably within the relative humidity range of 60% to 80% percent [16] due to the optimal balance between penetration rate of the CO_2 and the reaction rates in the pore water.

Due to the carbonation chemical reaction, the concrete porosity and mechanical properties change [43]. The most important change however, is the reduction of the pore water pH value to more neutral values (~ 9). The alkaline environment which allows the passivation of the rebars changes, causing the dissolution of the passive layer, thus leaving the steel bars vulnerable to corrosion. Water and oxygen presence in the proximity of the rebar surface triggers the corrosion mechanism. The corrosion rate is therefore governed by the moisture content in concrete and by the oxygen availability at steel surface. Due to the corrosion process, steel is consumed and corrosion products are formed over the rebar surface [44].

Rust presents a higher volume compared to steel, leading to the formation of overpressures on the concrete surrounding the rebar. Long duration of the corrosion process leads to an increase of rust deposits volume which results in the growth of the internal stresses over time. Once the pressures reaches the tensile strength of concrete, cracks nucleates on the concrete cover. Eventually, once fractures propagate to affect the whole cover depth, a direct path connecting the steel rebar to the external hazards is formed. The corrosion rates rise noticeably, bolstering the rupture process of concrete cover until spalling is observed, leaving steel rebars completely exposed to the environment.

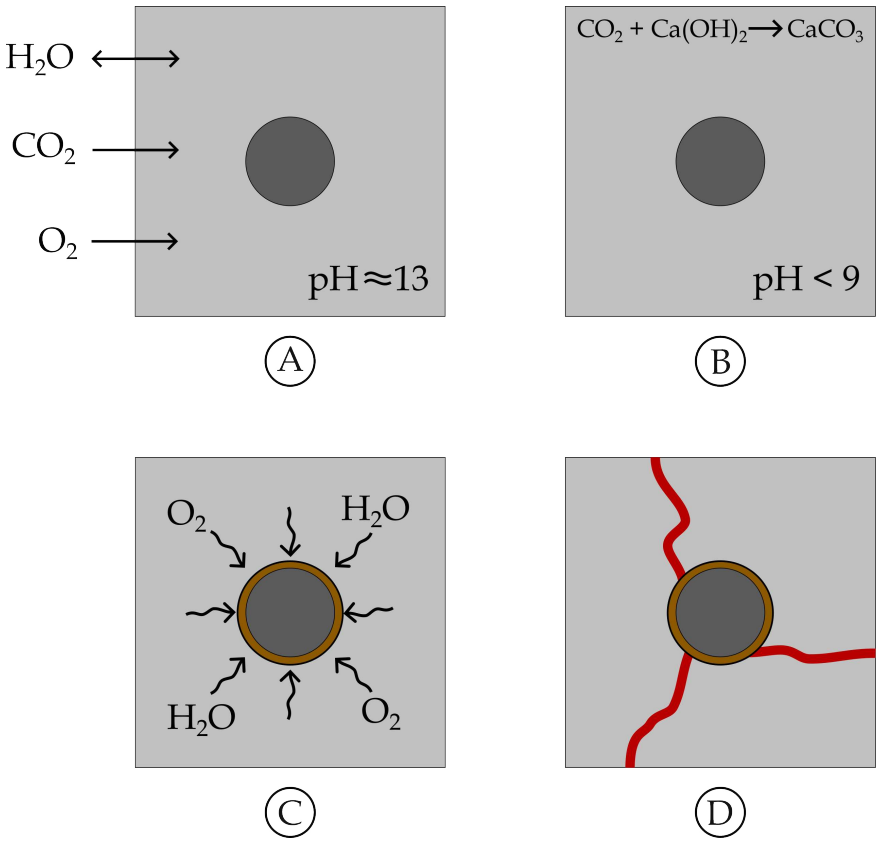

Figure 1.4: Summary of the carbonation corrosion phenomena. A) Intake of carbon dioxide, oxygen and moisture; B) Reaction process and reduction of pH value of concrete pore water; C) Corrosion process of steel rebar; D) Formation of cracks within concrete cover due to corrosion.

1.4 Numerical models for carbonation corrosion phenomena

To investigate and analyse every aspect of the carbonation corrosion phenomena many analytical and numerical models have been developed throughout the years. The possibility to describe via a set of mathematical equations the physical processes that cause the degradation mechanisms of reinforced concrete, permits to create tools which can provide valuable knowledge on the damaging effects of corrosion.

In [8, 45] a concrete carbonation model which accounts for the diffusion and reaction processes of carbon dioxide in concrete has been presented. From this, [46, 47, 48] improved the model by coupling carbonation with the moisture transport equations presented in [49, 50, 51] and temperature variations. Other models for carbonation have also been presented in [52, 53, 54]. Additionally, in [55] carbonation of underground concrete structures affected by a pressure gradient of pure CO_2 is analysed while in [56] a model to predict the penetration of carbonation reaction fronts in concrete is presented. Corrosion models for steel rebars embedded in concrete are presented in [57, 58, 59, 60]. In [61], effects on the corrosion rate due to humidity and temperature variations are considered. The carbonation induced corrosion process is described in [62, 18] while [63] analysed the mechanism of corrosion of steel

in carbonated concrete in cyclic wetting/drying exposure. Models describing the complete degradation phenomena, accounting for the full carbonation induced corrosion cracking of reinforced concrete, have also been studied in [64, 65, 66, 67]. A peridynamics model for the description of the concrete cover cracking due to corrosion has been given in [68] while a model describing the corner cracking of a reinforced concrete element is detailed in [69].

Starting from the numerical model previously presented in [70, 71], this work aims to expand the description of the carbonation corrosion cracking in reinforced concrete elements. Addition of moisture transport, variations of the oxygen content on the rebar surface during the corrosion process and an accurate description of the rust deposits formation have been added into the formulation to improve the previous models, creating a numerical algorithm which can describe accurately the carbonation corrosion phenomena in reinforced concrete elements. First, a coupled system of transport-diffusion-reaction equations is solved to define the evolution of the moisture content and the carbon dioxide diffusion within the concrete cover. Eventually, as the carbonation front advances through the concrete cover and approaches the steel rebar, the lowering of pH within the concrete pores causes dissolution of the passive layer which results in the initiation of corrosion process. Via the usage of electrochemical kinetics equations the corrosion current density value is defined on depassivated regions of steel rebar. Additionally, starting from the value of the current density, the amount of oxygen consumed and rust produced at the steel surface are defined. Lastly, the volume expansion produced by the formation of rust deposits is used as a loading parameter for the mechanical problem to evaluate the evolution of damage in the concrete cover, modelled with the phase field approach to brittle fracture.

The choice of the phase field approach to model the rupture process of the concrete cover is the result of the great capabilities of the method to accurately describe cracks within solids [12]. The phase field model to fracture is a variational approach based on the Griffith's theory [72] in which cracks are represented as a localized degradation of the material strength in broken areas. Fractures are introduced in a smeared manner as bands of non-zero thickness within a continuous scalar-valued phase field which can be seen as a damage parameter. The width of the damage bands is controlled by a scalar parameter that, if reduced to zero, allows to recover the sharp crack topology in a Γ-convergence sense [73]. Nucleation and evolution of cracks within the domain are described via the minimization of a two field functional which depends on the displacement field of the solid and the damage field.

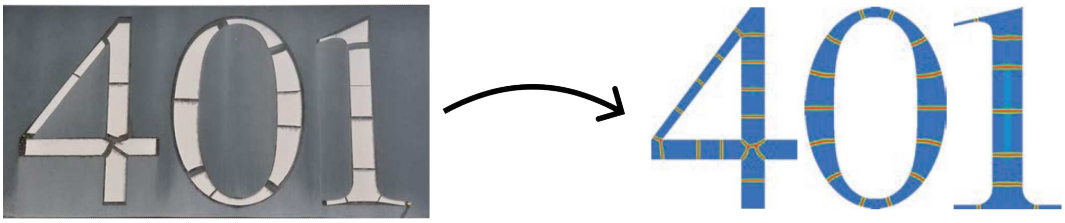

Figure 1.5: Application of the phase field model to reproduce the crack pattern on vinyl stickers at École Polytechnique, Palaiseau, France [17].

Numerous efforts have been made to extend the capability of the phase field model to describe a wide variety of rupture behaviours such as: cohesive fracture [74, 75], traction-compression anisotropy [76, 13, 77, 78], shear fracture [79, 80, 13, 81], composite materials [82, 83, 84, 85], ductile material [86, 87, 88, 89, 90, 91] and hydraulic fracturing

[92]. Additionally, in recent years, numerous applications of the phase field model to describe rupture in concrete have been presented. In [93], damage to concrete due to the coupled action of calcium leeching and fracture has been presented. Early-age fracture in cement-based materials have been analysed in [94]. Cracking in concrete induced by the intake of chloride ions has been described using the phase field approach in [95, 96]. Meso-scale phase field models which analyse the effects of the aggregate to the crack pattern in the concrete cover have been studied in [97, 98].

1.5 Research scope and objectives

The main goal of this work is the development of an innovative and reliable predictive model capable to describe the carbonation corrosion phenomena in reinforced concrete elements.

The model is based on the numerical implementation of the equations governing the various processes that characterize the carbonation induced corrosion. This approach permits to capture the effects on the degradation mechanisms given by the changes of the external environmental conditions (carbon dioxide concentration, relative humidity). Additionally, the synergistic interactions between the various physical-chemical and mechanical processes that characterise the carbonation corrosion phenomena are also considered. A thoroughly discussion on the effects of studied phenomena is provided, giving an overview on the most critical aspects to account while modelling degradation processes of reinforced concrete elements. A novel approach to describe the corrosion of rebar is presented. Pointwise numerical evaluation of the corrosion current density permits to define a non-uniform distribution of rust deposits which depends only on moisture and oxygen content in proximity to the steel surface. Moreover, as rust deposits are formed, the reduction of the cross section is tracked and the corrosion current density is evaluated on the new steel surface underlying the corrosion products. Based on the presence and thickness of the rust layer, two possible corrosion mechanisms are defined: an initial pure interfacial reaction step in which the corrosion rate is governed only by the oxygen and moisture content at the steel surface and a pure diffusion step in which the corrosion rate is governed by the diffusion process of oxygen and moisture through rust. The usage of the phase field model to describe cracking of the concrete cover, provides an accurate depiction of the degradation mechanism as a direct and strong correlation between the expansion of the rust deposits and the rupture of the cover is achieved.

The thesis is organized as follows. In section 2 the processes that characterize the carbonation corrosion phenomena of reinforced concrete elements are presented and the corresponding governing equations are detailed. Eventually, in section 3, the phase field approach to brittle fracture is introduced. The standard formulation which describes evolution of the rupture phenomena as an energy minimization process is presented. Also, the split functional used for the description of the concrete asymmetrical rupture behaviour is explained and representative examples of both standard and modified functional are analysed and compared. In section 4, details on the numerical aspects of the developed model are given. The finite element implementation of the governing equations is reported. Section 5 starts with the validation of the model by comparing the numerical results for each process with values from the literature. Eventually, two representative examples analysing the complete process are studied to prove the capability of the model to describe the carbonation corrosion phenomena in reinforced concrete. Lastly, section 6 reports the conclusions of the work by

providing additional comments on the capabilities of the developed model as well as outlining some interesting opportunities for possible future extensions to the model.

Chapter 2

Mathematical models for physical-chemical damage

2.1 Physical-chemical problems

Carbonation corrosion phenomena represents one of the main deterioration mechanism affecting the durability of concrete. It is a complex process in which the carbon dioxide present in the air of the surrounding environment penetrates the concrete element causing important modification to the material properties, ultimately leading to the corrosion of the reinforced bars.

Modelling the carbonation corrosion of concrete elements requires the analysis of the different mechanisms which impact the overall degradation process:

1 - Carbon dioxide diffusion-reaction: carbon dioxide is the cause for which the concrete carbonation process occurs. Its diffusion within concrete and chemical reactions with the elements of cement paste are the initial steps of the deterioration mechanism;

2 - Moisture transport: presence of water within concrete pores heavily impact diffusion and reaction process of carbon dioxide. In fact, a minimum amount of water is required for the chemical reactions to occur but an excess of water reduces the diffusion of carbon dioxide;

3 - Corrosion of steel rebar: as a result of the carbonation process, steel rebars embedded in reinforced concrete suffer the effects of corrosion due to the presence of oxygen and water within concrete, forming rust deposits on the metal surface;

4 - Oxigen diffusion: oxygen represent one of the main elements in the corrosion process of steel rebars. Its concentration on metal surface regulates the rate of the rebar corrosion;

5 - Cracking of concrete cover: formation of rust deposits on steel rebar causes overpressures on the surrounding concrete. Once the concrete tensile resistance is reached, cracking and eventually spalling of the concrete cover is observed.

In order to develop an accurate and reliable predictive model, the governing equations that describe each process should account for the effects of the other phenomena. Throughout the chapter, each sub-problem is presented and the interactions with the other processes analysed.

A reinforced concrete element of domain Ω is considered. The concrete portion of the element is referred as Ω_c while the steel rebar and the rust deposits are referred as Ω_s and Ω_r respectively. The boundary between concrete and the outer environment is marked as Γ_c, the outer boundary of steel rebar is marked as Γ_s while the interface between rust and concrete is marked as Γ_r. A standard Ordinary Portland Cement (OPC) concrete [40] is taken into account in which every element can be present in gaseous (g), aqueous (aq) or solid (s) form.

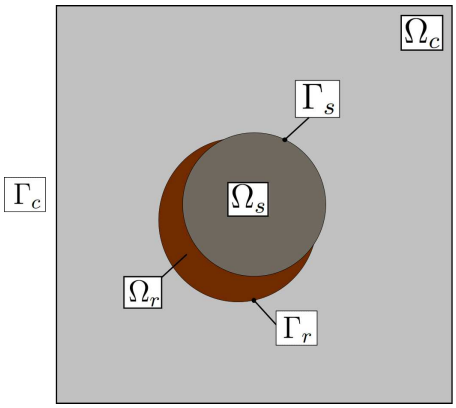

Figure 2.1: Reinforced concrete reference element and the corresponding domains.

2.2 Carbonation of concrete process

The first step of the carbonation corrosion phenomena in reinforced concrete elements consists in the carbon dioxide (CO_2) intake from the air of the surrounding environment. Since concrete is a porous material, the CO_2 can enter into the material through the surface pores and slowly diffuse towards the inner portion of the element. Eventually, the presence of carbon dioxide inside the pores triggers a series of chemical reactions between the CO_2 and the components of the cement paste which characterize the concrete carbonation process.

The main effects of the carbonation process on an ordinary portland cement concrete are:

- change of the material mechanical properties;
- reduction of the porosity;
- drop of the pH value of the concrete pore water.

The drop of the pH value of the pore water is probably the most harmful effect caused by the carbonation process on reinforced concrete elements. In fact, in its initial condition, concrete provides a high alkaline environment (pH $\sim$ 13) in which the reinforcement bars develop a protective passive layer which reduce to negligible values the rate of the rebar corrosion. However, as the carbonation front reaches the rebar, the drop of the pH to more neutral values ($\sim$ 9) cause the dissolution of the passive layer, leading to the start of the steel bar corrosion process.

In this section the diffusion-reaction process of the carbon dioxide within concrete is described. Effects of the concrete moisture content on the carbonation process are also discussed. Lastly, equations relating change in the material properties with the advancement of the carbonation process are presented.

2.2.1 Description of the carbonation process

Carbonation of concrete is a process in which the carbon dioxide (CO_2) diffuse through the pores of concrete and react with the calcium hydroxide ($Ca(OH)_2$) of the hardened cement paste producing calcium carbonate ($CaCO_3$). The initial step of the process consists in the intake and diffusion of the carbon dioxide in gaseous form, present in the air of the outer environment, through the surface pores of the concrete element. Eventually, the carbon dioxide within concrete reacts with the calcium hydroxide. However, the CO_2 reacts with the $Ca(OH)_2$ if both the reactants are in aqueous state. Therefore, for the carbonation reaction to occurs, both the carbon dioxide and the calcium hydroxide have to dissolve into the concrete pore water. The dissolution process for the CO_2 is given by the following reaction

$$\begin{aligned} H_2O + CO_2(g) &\rightarrow HCO_3^-(aq) + H^+(aq) \\ HCO_3^-(aq) &\rightarrow CO_3^{2-}(aq) + H^+(aq) \end{aligned} \tag{2.1}$$

while the calcium hydroxide dissolves in the concrete pore water as follows

$$Ca(OH)_2(s) \rightarrow Ca^{2+}(aq) + 2OH^-(aq). \tag{2.2}$$

Eventually, once both the reactants are dissolved into the pore water, calcium carbonate is produced as the result of the following neutralization reaction

$$Ca^{2+}(aq) + 2OH^-(aq) + CO_3^{2-}(aq) + 2H^+ \rightarrow CaCO3(s) + 2H_2O. \tag{2.3}$$

Calcium carbonate however, presents a lower solubility compared to calcium hydroxide, which leads to the rapid deposition of the $CaCO_3$ within the concrete pores. Therefore, as the pores gets progressively clogged by the calcium carbonate, the porosity of the carbonated concrete element lowers, reducing its gaseous and aqueous permeability properties. Since calcium hydroxide from the cement paste is consumed and replaced with calcium carbonate, the material properties of the carbonated concrete element also changes [40]. Additionally, due to the carbonation process the pH value of the concrete pore water drops to more neutral values (pH < 9). This effect is a key element of the degradation process caused by carbonation. In fact, in its non-carbonated state, the pore water present a high alkaline pH value (pH ~ 13) in which the steel bar creates a passive protection layer which prevents corrosion phenomena. However, due to the drop of the pH value the passive layer dissolves, leaving the steel bar highly susceptible to corrosion.

A different carbonation behaviour can be observed if a blended cement paste, such as BFS or fly ash concrete, are affected by the carbonation process. For these type of concrete, the lower content of calcium hydroxide leads to the reaction between the carbon dioxide and the C-S-H phase to be the main aspect of the carbonation process. As a result, slower rates of the neutralization reaction are observed and the porosity of the material increases, leading to a higher gaseous and fluid permeability of the material [99, 9].

To track the evolution of the carbonation process within the specimen, the carbonation front variable φ is introduced. Due to the nature of the carbonation process in which the calcium hydroxide from the cement paste is consumed to produce calcium carbonate, the carbonation front is defined based on the ratio between the remaining and the initial concentration of calcium hydroxide. It is possible to define the carbonation front as follows [9]

$$\varphi = 1 - \frac{[Ca(OH)_2(s)]}{[Ca(OH)_2(s)]^0} \tag{2.4}$$

where $[Ca(OH)_2(s)]$ is the remaining concentration of calcium hydroxide and $[Ca(OH)_2(s)]^0$ is the initial concentration. The carbonation front assumes value equal to 1 where the concrete is fully carbonated while is equal to 0 where the concrete is unaffected by the carbonation.

Since the carbonation front is used to describe the carbonation state of the concrete, it is possible to define a relationship between the evolution of the carbonation process and the changes on the material properties. The variation in the porosity of the concrete from ξ_C to ξ_{CaCO_3} and the change for a generic material property from P_C to P_{CaCO_3} due to the carbonation process are given by the following linear expressions

$$\xi(\varphi) = \xi_C + \varphi(\xi_{CaCO_3} - \xi_C); \quad P(\varphi) = P_C + \varphi(P_{CaCO_3} - P_C) \tag{2.5}$$

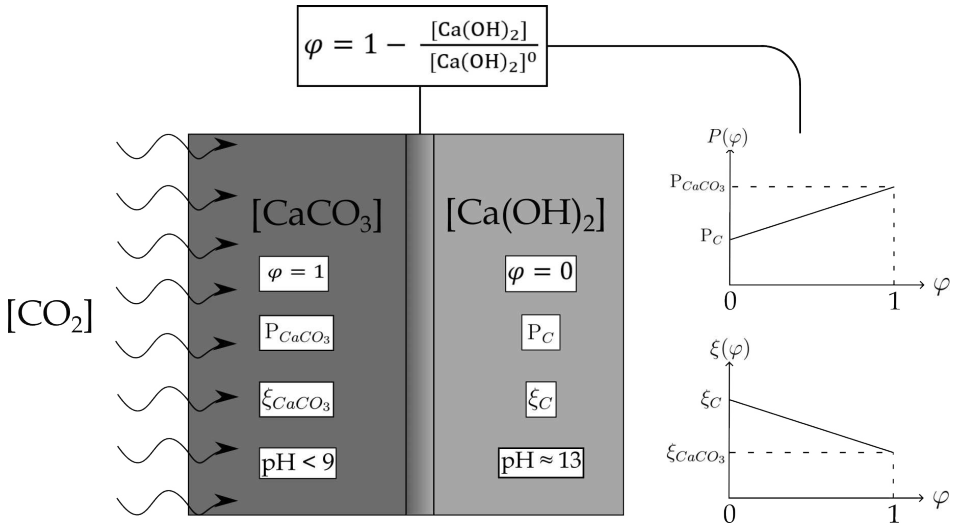

Figure 2.2: Effects of carbonation on concrete.

2.2.2 Mathematical model of the carbonation process

The modelling of the carbonation process therefore requires the analysis of the diffusion-reaction of the carbon dioxide, the dissolution and reaction of the calcium hydroxide and lastly the formation of the calcium carbonate. The starting point of the model consists in the diffusion and reaction of the carbon dioxide within the concrete cover. The diffusion-reaction process of the CO_2 is governed by the second Fick's law of diffusion where the reaction term is added to account for the neutralization reaction with the dissolved calcium hydroxide. Following the model proposed by [8] the diffusion-reaction equation of the CO_2 is the following

$$\frac{\partial}{\partial t}\left[\xi(\varphi)\left(1-f\right)[CO_2]\right] = \nabla \cdot \left(D_{CO_2}(\xi(\varphi), h, \alpha)\nabla\left[CO_2\right]\right) - \xi(\varphi) f_w \mathfrak{r}_n \quad in\ \Omega_c. \tag{2.6}$$

The diffusion equation for the carbon dioxide highlights the various interaction between the different phenomena. First, on the left hand side, carbon dioxide concentration is

multiplied by the term $\xi(\varphi)$ which accounts for the porosity variation due to the carbonation process and by the term $(1-f)$ which refers to the fraction volume of the gas-phase within the pores, being f the volume fraction of the pores corresponding to the liquid phase. The right hand side contains the diffusion and the reaction terms. Starting from the expression of the diffusion coefficient presented in [45], the coefficient $D_{CO_2}(\xi(\varphi), h, \alpha)$ has been modified according to [7] to accounts for the effects of the porosity changes, the relative humidity h and the damage state of the material α as follows

$$\begin{aligned} D_{CO_2}(\xi(\varphi), h, \alpha) &= A(\xi(\varphi))B(h)C(\alpha) \\ &= \xi(\varphi)^{1.8}(1-h)^{2.2}\left[1.42\cdot 10^{-6}(1-\alpha)^m + 10^5\alpha^m\right]. \end{aligned} \tag{2.7}$$

The diffusion coefficient can be separated as the product of three components. First, the carbonation state of the concrete is accounted in $A(\xi(\varphi))$ via the relationship between the porosity and the carbonation front. The second term, $B(h)$, presents the relationship between the carbon dioxide diffusion and the relative humidity, highlighting how the diffusion process is eased for lower values of the relative humidity while high values of relative humidity slow the diffusion process significantly. Lastly, $C(\alpha)$ accounts for the presence of cracks within the material and follows the expression presented in [100]. For the undamaged state ($\alpha = 0$), the expression yields the standard value presented in [45] while for fully broken material ($\alpha = 1$) a value of $\sim 10^5$ is considered to model an almost instantaneous diffusion process of the carbon dioxide through cracks. While presence of water within cracks could inhibit the movement of the gas, fully developed fractures create openings with the outer environment and based on the external condition (temperature, pressure, relative humidity, ecc...) different behaviours can be observed [101]. Throughout the work, a constant environmental temperature of 25°C is considered which allows to assume that the water present in the cracks evaporates leading to a free diffusive behaviour. The coefficient $m = 10$ has been used to control the non-linear trend of variation of the diffusion coefficient between the broken and sound portion of the concrete.

The reaction term of eq. 2.6 accounts for the neutralization reaction between the CO_2 and the $Ca(OH)_2$. Since carbon dioxide diffuse in gaseous state but the reaction occurs in the concrete pore water, the reaction rate r_n is multiplied by the term $\xi(\varphi)f_w$ which describes the portion of the pores partially filled with water, being f_w the corresponding volume fraction of the pores. The equation for the neutralization rate r_n is given in [8] and reads

$$r_n = HRTk_2\left[OH^-\right]_{eq}\left[CO_2(g)\right]\left[Ca(OH)_2(aq)\right] \tag{2.8}$$

where H is the Henry constant for the dissolution of CO_2(g) in water, R is the universal gas constant, T is the absolute temperature, k_2 is the reaction rate constant constant between the carbon dioxide and the calcium hydroxide, $[OH^-]_{eq}$ is the equilibrium concentration of the OH^- at saturation while $[CO_2(g)]$ and $[Ca(OH)_2(aq)]$ are the carbon dioxide and calcium hydroxide concentration respectively.

The relative humidity has a crucial role in the diffusion-reaction process of the carbon dioxide [102, 103] as described by eq. (2.6) and eq. (2.8). In fact, as observed in [54] the carbonation process of concrete has higher rates for relative humidity in the range between 60% and 80%. If the relative humidity assumes values higher than 80%, the carbon dioxide cannot diffuse through the pores of the concrete element as shown in Fig. 2.3(b). On the contrary, if the relative humidity is lower than 60%, the amount of pore water present in the concrete is not enough to allow sufficient carbon dioxide and calcium hydroxide to dissolve,

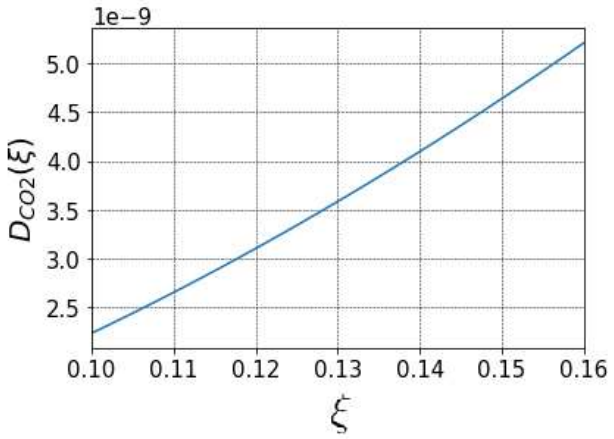

a)

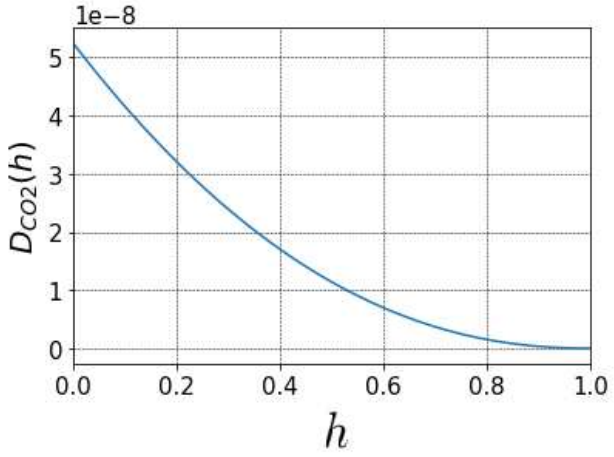

b)

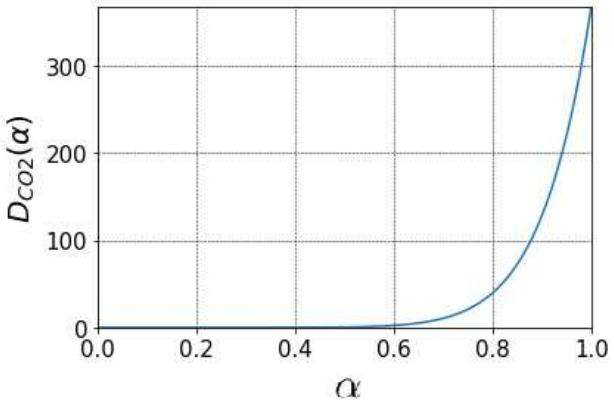

c)

Figure 2.3: Influence on the CO_2 diffusion coefficient from the various terms of eq. (2.7): a) porosity (h = 0.6; $\alpha = 0$), b) relative humidity ($\xi = 0.16$; $\alpha = 0$), c) damage ($\xi = 0.16$ and h = 0.6)

greatly reducing the rate at which the reaction occurs. This particular effect is accounted by the coefficients f, f_k and f_w which express the degree of saturation of the pores. As reported in [45], the degree of saturation can be computed starting from the pore size distribution of the specimen assuming hygrothermal equilibrium between the pores and the environment. Under this condition, starting from the value of the absolute temperature and the value of environmental relative humidity, it is possible to identify the Kelvin diameter d_K. Pores smaller than d_K are completely filled with water due to their small dimension while pores exceeding this value present a continuous film of water covering their walls. The value of the volume fraction of pores completely filled (f_k) and partially filled (f_w) with water can be evaluated following

$$f_k = \int_{-\infty}^{\log d_K} f_d d(\log d) \tag{2.9}$$

$$f_w = \frac{2Cxd_w}{[1+(C-1)x](1-x)} \int_{\log d_K}^{\infty} \frac{1}{d}(1-x^{d/2d_w}) f_d d\log d \tag{2.10}$$

where f_d is the value of the probability density function corresponding to the pores of diameter equal to d, x is given by $h/100$, C is the BET-constant which can be assumed approximately equal to 100 for non-carbonated concrete and equal to 1 for carbonated concrete and d_w is the molecular diameter of water equal to $3 \cdot 10^{-4} \mu$m. Lastly, the degree of saturation of the specimen which corresponds to the volume fraction of the total liquid phase of the pores, is obtained as the sum of the volume fraction of the pores completely filled with water and the volume fraction of the pores partially filled with water.

$$f = f_k + f_w. \tag{2.11}$$

Fig. 2.4 reports the curves for the pore size distribution on fully hydrated hardened non carbonated OPC concrete for a water-cement ratio of 0.5, showing the effects of the relative humidity on the degree of saturation of the pores.

After the analysis of the diffusion-reaction process of the carbon dioxide, the attention is put on the changes to the calcium hydroxide concentration. As a result of the hydration process, calcium hydroxide is produced in solid form in the cement paste and eventually, it dissolves in the concrete pore water at rate r_d. Experimental studies have shown that for a standard fully hydrated OPC concrete, the amount of calcium hydroxide produced as result of the hydration process is approximately ∼30% by weight [104, 105, 8]. The mass balance equation for the solid portion of the calcium hydroxide accounts for its dissolution in the concrete pore water while the mass balance for the liquid phase accounts for both its production from the solid phase as well as for its diffusion through the pore water. Following [8], the mass balance equations are therefore expressed as

$$\frac{\partial}{\partial t}[Ca(OH)_2(s)] = -r_D \qquad in\ \Omega_c \tag{2.12}$$

$$\frac{\partial}{\partial t}\left(\xi(\varphi) f[Ca(OH)_2(aq)]\right) = \nabla \cdot \left(D_{Ca(OH)_2}(\xi(\varphi), h, \alpha)\nabla[Ca(OH)_2(aq)]\right) \tag{2.13}$$

$$-\xi(\varphi) f_w r_n + r_D \qquad in\ \Omega_c \tag{2.14}$$

where $[Ca(OH)_2(s)]$, $[Ca(OH)_2(aq)]$ are the solid and aqueous concentration of the calcium hydroxide respectively, r_d is the dissolution rate of the solid calcium hydroxide and

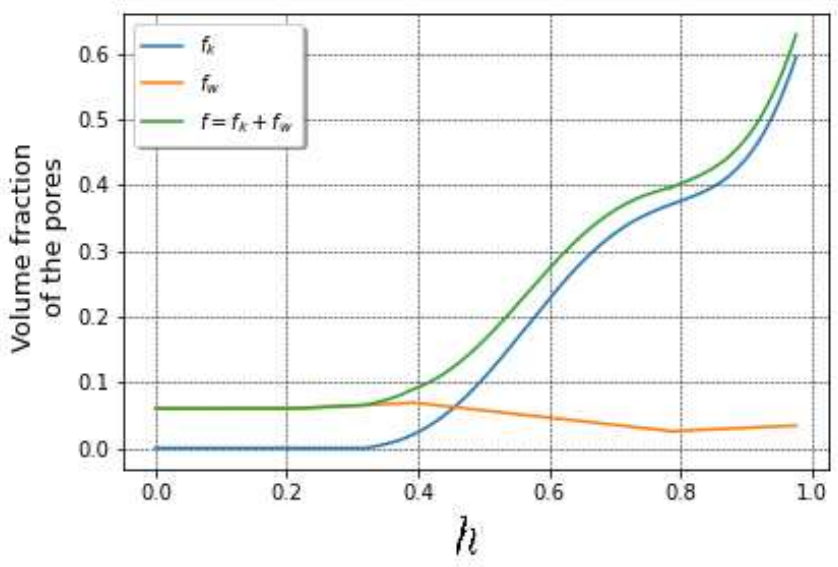

Figure 2.4: Plot of the different volume fractions of the pores corresponding to the liquid phase: fraction of the pores completely filled f_k, fraction of the pores partially filled f_w, fraction of the pores of the total liquid phase f.

$D_{Ca(OH)_2}(\xi(\varphi), h, \alpha)$ is the diffusion coefficient through the pore water of the calcium hydroxide. The dissolution rate r_d is expressed with good approximation by

$$r_d = 0.5\xi(\varphi) f_w k_s a_s [Ca(OH)_2(s)] \bar{V}_{CH}([OH^-]_{eq} - [OH^-]) \tag{2.15}$$

where k_s is the mass transfer coefficient for the solid calcium hydroxide, a_s is the specific area of the pores in contact with water [45] and $\bar{V}_{CH}$ is the molar volume of the solid calcium hydroxide. Should be noted that, as reported in [8], the diffusion term of eq. 2.14 assumes small values such that can be neglected for values of the relative humidity smaller than 90%, therefore equations 2.12 and 2.14 can be added together. This allows to define the evolution of the calcium hydroxide in its entirety, solid and dissolved, via a single mass balance equation given by

$$\frac{\partial}{\partial t}[Ca(OH)_2] = -\xi(\varphi) f_w r_n \quad in\ \Omega_c \tag{2.16}$$

Lastly, the formation of the calcium carbonate is modelled as a reaction equation in which the production of the $CaCO_3$ is described as the result of the neutralization reaction from the carbon dioxide and the calcium hydroxide as follows

$$\frac{\partial}{\partial t}[CaCO_3] = \xi(\varphi) f_w r_n \quad in\ \Omega_c \tag{2.17}$$

A key aspect of the carbonation process is the lowering of the pH value of the concrete pore water from high alkaline values of approximately ∼13 to more neutral values. Based on the stoichiometry of the chemical reaction reported in eq. 2.2 it is possible to determine the OH^- molar concentration, which can be used to determine the value of the pH following the relationship provided in [8] which states

$$pH = 14 + \log(2 \cdot 10^3 [Ca(OH)_2]) \quad in\ \Omega_c \tag{2.18}$$

The passive layer, which is formed around the steel rebar during the hydration process of the concrete as a result of the the high alkaline environment provided by the hydrated cement paste, dissolves as the pH lower to more neutral values leading to the initiation of the corrosion process as water and oxygen are present in the proximity of the steel rebar.

Summing up, the complete system which governs the carbonation process is the following

$$\frac{\partial}{\partial t}\left[\xi(\varphi)\left(1-f\right)[CO_2]\right] = \nabla \cdot \left(D_{CO_2}(\xi(\varphi), h, \alpha)\nabla\left[CO_2\right]\right) - \xi(\varphi) f_w \mathtt{r}_n \qquad in\ \Omega_c \tag{2.19}$$

$$\frac{\partial}{\partial t}[Ca(OH)_2] = -\xi(\varphi) f_w r_n \qquad in\ \Omega_c \tag{2.20}$$

$$\frac{\partial}{\partial t}[CaCO_3] = \xi(\varphi) f_w r_n \qquad in\ \Omega_c \tag{2.21}$$

$$\varphi = 1 - \frac{[Ca(OH)_2]}{[Ca(OH)_2]^0} \qquad in\ \Omega_c \tag{2.22}$$

$$pH = 14 + \log(2 \cdot 10^3 [Ca(OH)_2]) \qquad in\ \Omega_c \tag{2.23}$$

To complete the model, appropriate initial and boundary conditions are required for eqs. 2.19 - 2.20 - 2.21. First, for eq. 2.19 a constant concentration is applied to the external boundary of the concrete cover and a no flux condition is applied to the steel domain boundary since carbon dioxide cannot diffuse through steel. The initial concentration of the carbon dioxide within the concrete element is assumed equal to zero. Therefore the following initial and boundary conditions are applied to the mass balance equation of CO_2

$$[CO_2](\Omega_c, 0) = 0 \tag{2.24}$$

$$[CO_2](\Gamma_c, t) = \overline{[CO]}_2 \tag{2.25}$$

$$\nabla[CO_2](\Gamma_s, t) = 0 \tag{2.26}$$

where $\overline{CO}_2$ is the concentration of carbon dioxide in air equal to 412 ppm [106]. For the calcium hydroxide an initial concentration equal to $Ca(OH)_2^0$ is considered while the initial concentration of the carbon dioxide is set to zero as it is the result of the neutralization reaction 2.21. Therefore, the following condition for the $Ca(OH)_2$ and the $CaCO_3$ initial concentration are set to complete the model

$$[Ca(OH)_2](\Omega_c, 0) = [Ca(OH)_2]^0 \tag{2.27}$$

$$[CaCO_3](\Omega_c, 0) = 0 \tag{2.28}$$

2.3 Moisture transport

Moisture content in reinforced concrete greatly impact its long term performance and durability [107, 108]. Not only the material properties of concrete are affected but the behaviour of the material with respect to time-dependant phenomena such as creep,

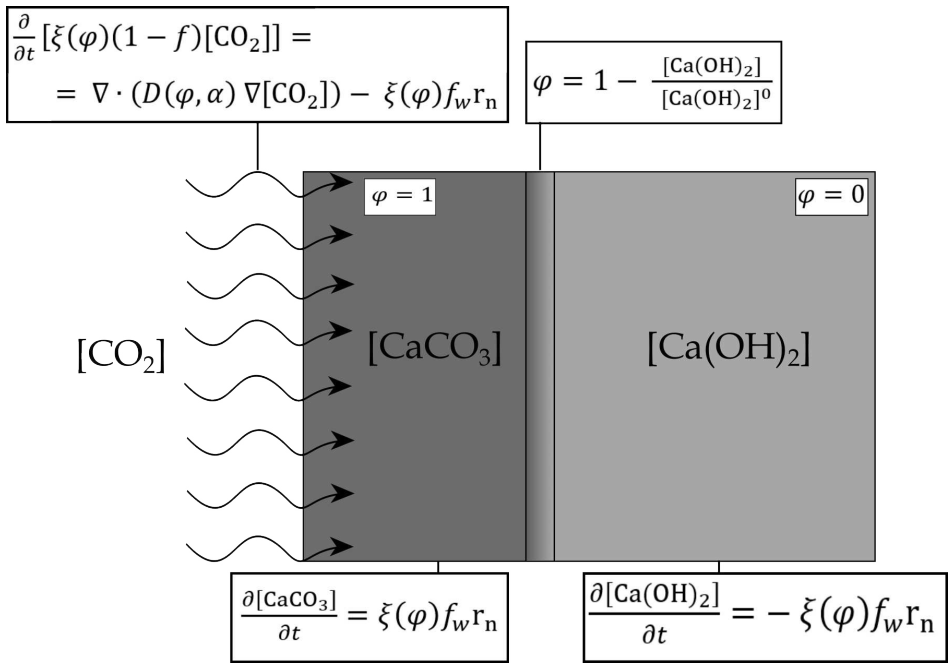

Figure 2.5: Carbon dioxide diffusion-reaction system

shrinkage, fire resistance [109, 110, 111] changes. Moreover, as previously presented, it heavily affects the carbonation process of concrete elements as it plays a key factor in both the diffusion of the carbon dioxide through the pores of the concrete as well as the neutralization reaction between the CO_2 and the $Ca(OH)_2$ [112, 113]. Therefore, an accurate description of its transport through the concrete is required in order to obtain a model which can correctly represent the deterioration process of concrete carbonation.

2.3.1 Mathematical model for the moisture transport in concrete

Concrete is a material in which the pore size distribution has a wide range of values and the diffusivity of moisture heavily depends on the pore structure. A moisture transport model which describes the moisture transport by accounting the relationship between the water movement within the concrete pores and the concrete pore structure has been presented in [114, 50, 51]. Moisture in concrete travels from regions with higher to lower water content. Therefore, the water flux within concrete J_w can be express in terms of the water content gradient ∇W as

$$J_w = -D_w \nabla W \tag{2.29}$$

which lead to the following mass balance equation

$$\frac{\partial W}{\partial t} = \frac{\partial (W_e + W_n)}{\partial t} = \nabla \cdot (D_w \nabla W) \tag{2.30}$$

where W is the water content per unit volume, obtained as the sum of the evaporable water content W_e and the non-evaporable water content W_n, and with D_w being the moisture diffusivity.

However, the formulation for the moisture transport expressed in term of water content per unit volume presents some drawbacks [50]:

- if changes to the evaporable water content due to the hydration process are considered, the term $\partial W_n/\partial t$ does not have negligible values until the hydration process has completely ceased;

- if variations of temperature are considered, ∇W or ∇W_e cannot always be considered driving forces for moisture transport within the concrete.

In order to overcome the mentioned problems and better analyse the process, the use of pore relative humidity h instead of the water content per unit volume is introduced. In fact, the drop in the pore relative humidity due to self dessication during the hydration period is small such that can be neglected. Additionally, even for changes in temperature, the gradient of the relative humidity still provides a driving force for the moisture transport. Moreover, the environmental conditions are usually expressed in terms of relative humidity instead of water content. By applying a change of variable to eq. 2.30 it is possible to write the mass balance equation in term of the pore relative humidity h as follows

$$\frac{\partial W}{\partial t} = \frac{\partial W}{\partial h}\frac{\partial h}{\partial t} = \nabla \cdot (D_h \nabla h) \quad in\ \Omega_c \tag{2.31}$$

where D_h represent the permeability or humidity diffusivity of the material and $\partial W/\partial h$ represent the moisture capacity. It is therefore necessary to define the value of both the coefficients in order to describe the moisture transport within the concrete pores.

In order to define the moisture capacity $\partial W/\partial h$, a relationship between W and h is required. The relationship which correlates the water content and the relative humidity is given by the Brunauer-Emmet-Teller (BET) isotherm model [115, 50] derived from the statistical thermodynamics of absorption. In particular, the modified BSB model has been used as it is a modified BET model which is applicable to relative humidity values ranging form 0.05 to 1 [116]. The application of the model is possible because the diffusive process of moisture through the concrete pores is slow enough that the various phases of water within the pores can be considered in thermodynamic equilibrium at any time. Since the absorption of water in concrete is heavily affected by the pore structure of the material, the BSB model considers the different parameters which have effects on the pore distribution such as water/cement ratio, curing time, temperature, type of cement, additives to the concrete mix, sand-cement ratio and gravel-cement ratio. Following [50] only the effects of water/cement ratio, curing time and temperature are considered. The relationship between the water content and the pore relative humidity at a fixed temperature is therefore given by

$$W(h) = \frac{CkV_m h}{(1-kh)[1+(C-1)kh]} \tag{2.32}$$

where C and k are two parameters of the BSB model and V_m represents the monolayer capacity.

The monolayer capacity V_m is defined as the mass of adsorbate (water) required to cover the adsorbent (concrete pore surface) with a single molecular layer. It depends form the curing time t_e and the initial water/cement ratio w/c of the specimen and its expression is given as follows

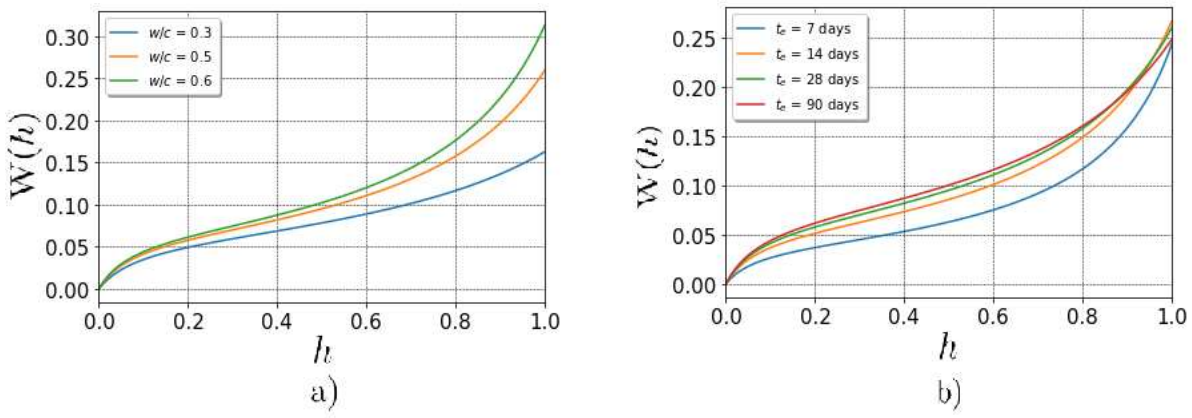

Figure 2.6: Plot of W(h): a) changes due to w/c ratio b) changes due to t_e

$$V_m(w/c, t_e) = \begin{cases} (0.068 - \frac{0.22}{t_e})(0.85 + 0.45w/c) & \text{if } t_e > 5 \text{ days and } 0.3 < w/c < 0.6 \\ 0.024(0.85 + 0.45w/c) & \text{if } t_e \leq 5 \text{ days} \\ 0.985(0.068 - \frac{0.22}{t_e}) & \text{if } w/c \leq 0.3 \\ 1.12(0.068 - \frac{0.22}{t_e}) & \text{if } w/c \geq 0.6 \end{cases} \tag{2.33}$$

The parameter k is introduced to account that the number of absorbed layer is finite [116, 50]. The definition of the parameter is therefore based on the number of adsorbed layers at the saturation state n which depends, similarly to the monolayer capacity, from the curing time t_e and the initial water/cement ratio w/c. Starting from the determination of n then the parameter k is expressed as

$$k = \frac{(1 - 1/n)C - 1}{C - 1} \tag{2.34}$$

where n is defined as

$$n(w/c, t_e) = \begin{cases} (2.5 + \frac{15}{t_e})(0.33 + 2.2w/c) & \text{if } t_e > 5 \text{ days and } 0.3 < w/c < 0.6 \\ 5.5(0.33 + 2.2w/c) & \text{if } t_e \leq 5 \text{ days} \\ 0.99(2.5 + \frac{15}{t_e}) & \text{if } w/c \leq 0.3 \\ 1.65(2.5 + \frac{15}{t_e}) & \text{if } w/c \geq 0.6 \end{cases} \tag{2.35}$$

Lastly, parameter C is defined as

$$C = \exp\frac{855}{T} \tag{2.36}$$

Only the absorption process has been considered while presenting the relationship between the concrete pore moisture and the relative humidity. An expression for the desorption process should be used instead to describe the drying process. However, as reported in [51], the shape of the curve has more influence compared to the exact value assumed by each curve. Experimental results have shown that both curves have a comparable shape [117, 118, 115, 51] in practical range of H. Additionally, eq. 2.32 is valid for both adsorption

and desorption processes. Finally, by differentiating eq. 2.32 with respect to the relative humidity it is possible to obtain the moisture capacity as

$$\frac{\partial W}{\partial h} = \frac{CkV_m + Wk[1 + (C-1)kh] - Wk(1-kh)(C-1)}{(1-kh)[1 + (C-1)kH]} \,. \tag{2.37}$$

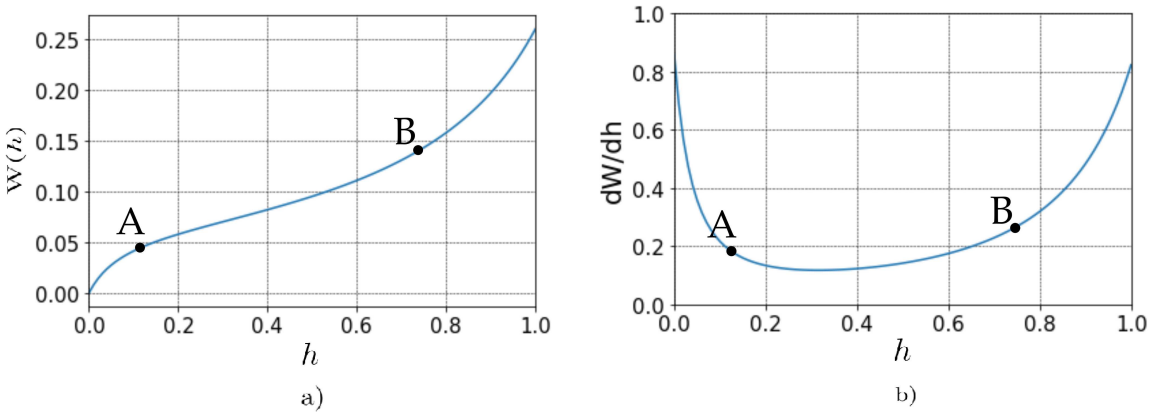

Figure 2.7: a) W(h); b) moisture capacity. Both curves are obtained for $w/c = 0.5$, $t_e = 28$ days and T = 298,15 K.

From fig. 2.7 it is possible to identify two curvature changes points which defines three different areas in the graph of the moisture content - relative humidity relationship. Point A in fig. 2.7 represent the point in which the monolayer capacity is reached and the moisture capacity becomes almost constant. Point B marks the start of the capillary condensation, which causes a steep increase of the moisture capacity.

The second parameter required to define the moisture transport process is the diffusivity parameter D_h. This parameter strongly depends on the pore structure and should accounts for the different diffusion processes which can take place based on the pore size dimension and irregularities. The model presented in [114, 51, 18, 62] does not separates the various diffusion processes but provides an expression for the diffusion coefficient which predicts the general behaviour of water transport. The moisture diffusion coefficient is defined as

$$D_h = D_{h,ref} F_1(h) F_2(T) F_3(t_e) F_4(\xi(\varphi)) \tag{2.38}$$

where $D_{h,ref}$ is the diffusion coefficient value for the reference conditions of the specimen and $F_1(h), F_2(T), F_3(t), F_4(\xi(\varphi))$ are three correction functions which accounts for the effects of the current humidity, the temperature, equivalent curing time and porosity. The value for $D_{h,ref}$ typically ranges from $1.157 \cdot 10^{-10}$ to $4.630 \cdot 10^{-10}$ m^2/s with water/cement ratio ranging from 0.45 to 0.8 [49, 114]. The first function $F_1(h)$ accounts for the influence of the current pore relative humidity due to the fact that the amount of water within the pores modifies the diffusion mechanism. Its expression has been given in [49, 114, 119] as follows

$$F_1(h) = \delta_0 + \frac{1-\delta_0}{1 + (\frac{1-h}{1-h_c})^m} \tag{2.39}$$

where δ is a parameter which characterizes the ratio between the minimum and the maximum value of the moisture diffusion coefficient and can be assumed equal to 0.05, h_c represents the value of the relative humidity at which D_h assumes a median value between its maximum and

minimum values and has been found to be 0.75 for different concrete and cement pastes, m is a coefficient which characterizes the spread of the drop in D_h and its value can range between 6 and 16. An intermediate value of $m = 10$ has been assumed during the simulations.

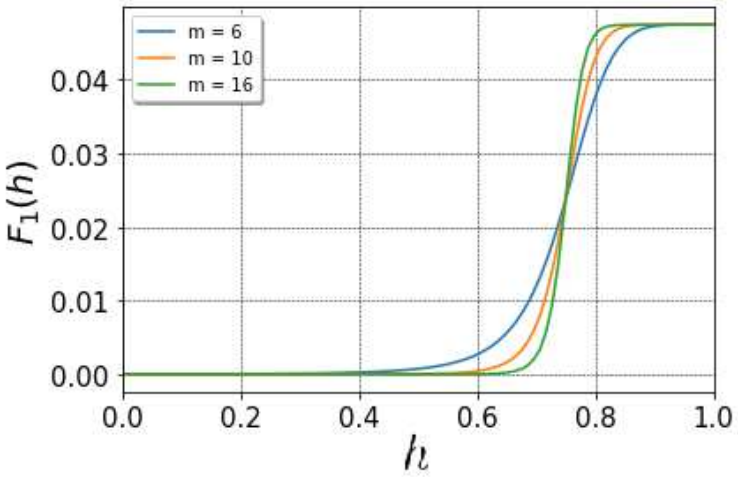

Figure 2.8: Influence of the parameter m on $\mathrm{F}_1(h)$

The second function $F_2(T)$ relates the coefficient D_h to the temperature of the specimen. Its expression has been given in [119, 46, 47] as follows

$$F_2(T) = \exp\left[\frac{U}{R}\left(\frac{1}{T_{ref}} - \frac{1}{T}\right)\right] \tag{2.40}$$

where U is the activation energy of the moisture diffusion process, R is the universal gas constant, T_{ref} is the reference temperature corresponding to $D_{h,ref}$ and is taken equal to 296 K. Literature provides typical values for the ratio U/R which ranges from 2700 K [119, 47] up to 4700 K [46].

The diffusivity coefficient depends on the equivalent curing time t_e through the function $F_3(t_e)$ presented in [46] as follows

$$F_3(t_e) = 0.3 + \sqrt{\frac{13}{t_e}} \tag{2.41}$$

The equivalent curing time is defined in [114] as the equivalent hydration period of the concrete and it expression reads

$$t_e = t_0 + \int_{t_0}^{t} \beta_T \beta_h dt \tag{2.42}$$

where t_0 is the time of first exposure of concrete and β_T, β_h are two empirical functions which relates the equivalent curing time with the effects of temperature and pore relative humidity. The expression for these two functions are given in [114] as follows

$$\beta_T = \exp\left[\frac{U}{h}\left(\frac{1}{T_{ref}} - \frac{1}{T}\right)\right] \tag{2.43}$$

$$\beta_h = [1 + (7.5 - 7.5h)^4]^{-1} \tag{2.44}$$

The expression of β_T resemble the expression for $F_2(T)$, however here the U_h is the activation energy required for the start of the hydration process of the concrete and the value of the ratio U_h/R can be obtained following the expression given in [46]

$$\frac{U_h}{R} = 4600 \left[\frac{30}{T - 263}\right]^{0.39} \tag{2.45}$$

The last parameter affecting the moisture diffusivity coefficient is given by

$$F_4(\xi(\varphi)) = 1 - \frac{\xi_{CaCO_3}}{\xi_{CO_2}}\varphi \tag{2.46}$$

where ξ_{CaCO_3} and ξ_{CO_2} are the porosity of the carbonated and non carbonated concrete respectively and φ the carbonation front. This term accounts for the reduction in the moisture transport given by the change in the porosity due to the carbonation process. Following a similar approach compared to [120, 121], the proposed equation apply a reduction to D_h proportional to the reduction of the porosity within the specimen due to the pore clogging associated with the carbonation process.

Lastly, to complete the formulation for the moisture transport, appropriate initial and boundary conditions are required. An initial value for the moisture content equal to h^0 is set in the concrete domain:

$$h(\Omega_c, 0) = h^0 \ . \tag{2.47}$$

A Neumann Boundary condition, which accounts for the environmental values of relative humidity, is applied to the external faces of the concrete cover which simulates the exchange of humidity between concrete and the external air. Therefore, the following condition is applied to Γ_c

$$J_h(\Gamma_c, t) = B_h(h - \overline{h}_{en}) \tag{2.48}$$

where B_h is the surface moisture transfer coefficient, h is the pore relative humidity at the concrete surface and h_{en} is the environmental relative humidity. The value of h_{en}, has been defined starting from the reports of relative humidity of the city of Parma. In particular, the average value for each month has been computed from the previous 5 years and reported in table 2.1. During the numerical analysis, the outer relative humidity value changes according to the time of the simulation.

Month	h_{en}
January	0.55
February	0.60
March	0.65
April	0.70
May	0.75
June	0.80
July	0.80
August	0.85
September	0.85
October	0.75
November	0.70
December	0.65

Table 2.1: Value of the environmental relative humidity for each month.

2.4 Corrosion process in reinforced concrete elements

Corrosion of the reinforcement bar in reinforced concrete elements represents one of the most dangerous degradation mechanism affecting the serviceability and durability of reinforced concrete structures. Due to corrosion, the material performances diminish noticeably. Reduction of the bearing capacity, loss of ductility, debonding of the steel-concrete interface, cracking and spalling of the concrete cover are some of the most severe degradation processes experienced by reinforced concrete due to corrosion [122, 123, 124, 16].

The causes for the corrosion process to occur in reinforced concrete elements are mainly two: chloride ions and carbon dioxide intake [122]. Throughout this work, only the carbonation induced corrosion is considered. Here, the corrosion process is triggered by the drop in pH of the concrete pore water caused by the carbonation reactions. In fact, once the pH reaches more neutral values the protective layer surrounding the rebar dissolves, leaving the steel highly susceptible to corrosion. Since water and oxygen are present in the vicinity of the depassivated rebar, the corrosion mechanism initiates.

2.4.1 Kinematics of the corrosion process

Corrosion is an electrochemical process in which a metallic material undergoes a degradation mechanism involving chemical and physical processes caused by exposure to an aggressive environment. As a result of this phenomenon, a loss of mass in the metallic material is observed and this mass is transformed in deposits of wast material [11].

The overall process can be viewed as the interaction between two separate chemical reactions, and anodic process in which the metal oxidation release electrons and a cathodic reduction which consumes them. It is important to analyse both the anodic and cathodic processes and define the overall corrosion process based on their relation. The corrosion of steel in reinforced concrete structures can be seen as the interaction between the two following processes:

- Anodic half-cell reaction: oxidation of the steel rebar

$$2Fe \rightarrow 2Fe^{2+} + 4e^{-} \tag{2.49}$$

- Cathodic half-cell reaction: reduction of the oxygen

$$O_2 + 2H_2O + 4e^{-} \rightarrow 4OH^{-} \tag{2.50}$$

For the corrosion cell to form, it is necessary for the metal to be in an environment which can act as an electrolyte in which transport of the electrons from the anodic to the cathodic site can take place. For the corrosion of steel in reinforced concrete elements, this environment consists in the pore water present in the surrounding of the steel rebar which act as a medium for the electrons to be transferred between the steel and the oxygen [11].

In a carbonated concrete element, the corrosion process initiates when the carbonation front reaches the rebar surface, and due to the drop of the pH value the protective passive layer dissolves. The depassivation process is uniform along the length of the rebar due to the homogeneous advancement of the carbonation front within the concrete element. As a result, a uniform corrosion process of the bar is observed in which a high number of microcells are formed along the bar length, where anode and cathodes areas form in close proximity and continuously exchange electrons between each other [11, 125].

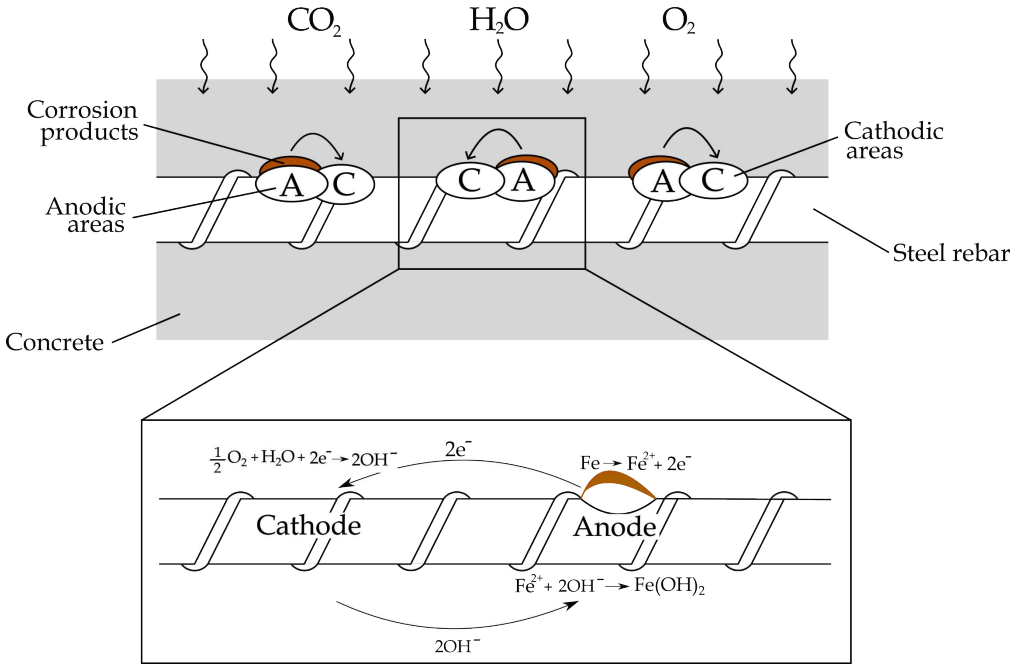

Figure 2.9: Microcell system

Additionally, since the process is developed in a microcell corrosion system, the dissolved iron of eq. 2.49 and the hydroxides from eq. 2.50 are consumed locally [126] leading to the complete corrosion reaction [127]

$$\begin{aligned} Fe^{2+} + 2OH^{-} &\rightarrow Fe(OH)_3 \\ 4Fe(OH)_2 + O_2 + 2H_2O &\rightarrow 4Fe(OH)_3 \\ 4Fe(OH)_3 &\rightarrow 2Fe_2O_3 \cdot H_2O + 4H_2O \end{aligned} \tag{2.51}$$

The complete corrosion process, form the electrochemical perspective, can be subdivided in four processes which occurs at the same rate

1 - electrons released by the anodic reaction generates an anodic current I_a;

2 - electron flow through the electrolyte I_{el};

3 - electrons consumed by the cathodic reaction generates to the cathodic current I_c;

4 - current flows from the cathodic to the anodic site through the metal I_m;

therefore $I_a = I_c = I_m = I_{el} = I_{corr}$ where I_{corr} is usually employed to describe the current density defining the rate of the corrosion process.

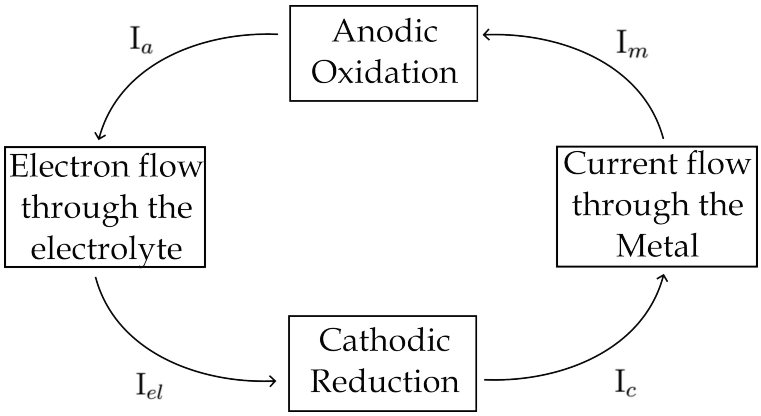

Figure 2.10: Electrochemical mechanism of the corrosion process

Is important to notice that all the processes happens at the same rate, therefore the corrosion rate will be governed by the slowest process between the metal dissolution (anodic control), the cathodic reduction (cathodic control) or the flow of electrons through the electrolyte due to resistances from the medium (ohmic controlled). However, since a microcell corrosion system develops in which the anodic and cathodic areas are in close proximity, both the current transport in the electrolyte and in the metal occur almost instantaneously. Therefore, it is possible to neglect the ohmic drop, which is usually experienced where the anode and the cathode areas are separated between each other and the flux of electrons has to travel some distance to reach the cathode causing a loss of current [125].

2.4.2 Electrochemical kinetics equations

The corrosion process of the steel rebar has been modelled using the electrochemical kinetics equations. As previously presented, corrosion in a carbonated concrete is characterized by a microcell system in which electrons released by the anode are locally consumed by the cathode. The parameters which can be used to characterize an electrochemical reaction are the equilibrium potential E_0 and the equilibrium current density i_0. The equilibrium condition of a single element is achieved when its cathodic and anodic processes occurs at the same rate and therefore

$$i_a = i_c = i_0 \quad at \quad E = E_0 \tag{2.52}$$

Starting from the equilibrium condition, if the metal is brought to a potential E, the current density shifts to $i \neq i_0$ and it is possible to define the overvoltage as the difference between the potential E and the equilibrium potential E_0.

$$\eta = E - E_0 \tag{2.53}$$

As the microcells are formed, electrons are exchanged from the anode to the cathode causing a shift of the electric potential away form equilibrium for both the reactions. This change in potential is known as polarization. Two overvoltages are therefore defined, one for the anode and one for the cathode.

$$\begin{aligned} \eta_a &= E_a - E_{0,Fe} > 0 \\ \eta_c &= E_c - E_{0,O2} < 0 \end{aligned} \tag{2.54}$$

The degree of polarization of each half-cell is what defines the kinetics of the corrosion process. The behaviour of each semi-reaction, defined in terms of the change of electrochemical potential and current density, are described via the Evans diagram. These diagrams reports the polarization curves for each half-cell reaction and provide information on the type of corrosion attack, presence of corrosion rate-controlling mechanisms and allows to identify the corrosion electrochemical potential E_{corr} and the corrosion current density i_{corr}. The values for E_{corr} and i_{corr} are defined as the elecrochemical potential and the current density corresponding to the intersection point of the anodic and cathodic polarization curves. Fig. 2.11 reports the Evans diagram for the steel corrosion due to oxygen cathodic reduction.

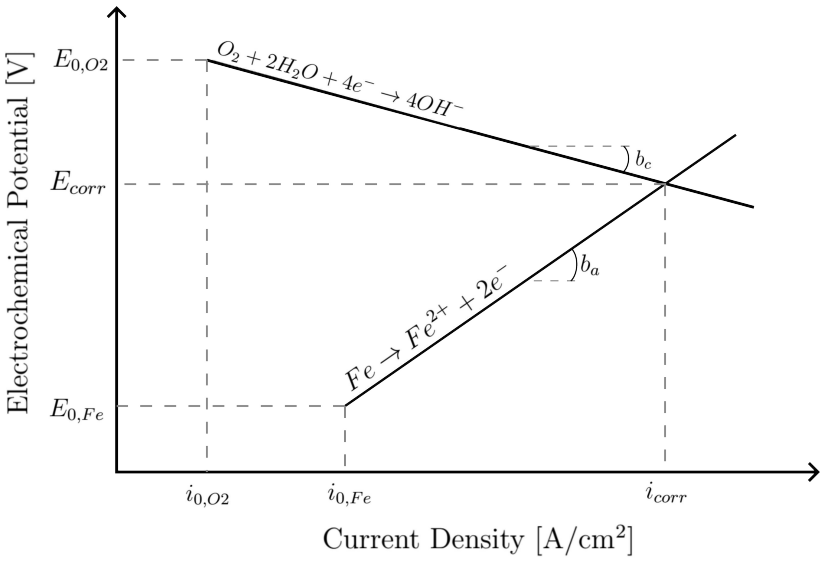

Figure 2.11: Evans Diagram for the iron corrosion in abundance of oxygen

where $E_{0,Fe}$ and $E_{0,O2}$ are the equilibrium electrochemical potential for the iron and for the oxygen, $i_{0,Fe}$ and $i_{0,O2}$ are the equilibrium current density for the iron and for the oxygen while E_{corr} and i_{corr} are the corrosion electrochemical potential and current density. As the corrosion process continues, oxygen on the rebar surface is consumed and its concentration gradually reduces, thus creating a limiting current density which depends on the actual oxygen content on the rebar surface. The Evans diagram describing the corrosion process with low oxygen supply is reported in Fig. 2.12.

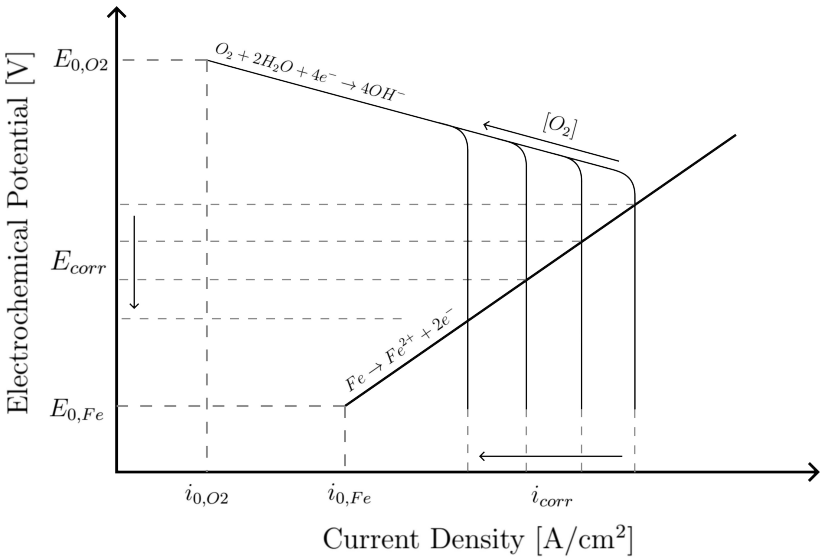

Figure 2.12: Evans Diagram for the iron corrosion with limited oxygen

The expression of the polarization curves plotted in the Evans diagram is given by the Butler-Volmer equation, which provides an expression for the current density as a function of the electrochemical overpotential for each semi-reaction. The Butler-Volmer equation for the anodic process is given as follows

$$i_a = i_{0,Fe} \exp\left(2.3 \frac{E_{corr} - E_{0,Fe}}{b_a}\right) \tag{2.55}$$

where $i_{0,Fe}$ is the iron exchange current density at the equilibrium condition, E_{corr} is the corrosion potential, $E_{0,Fe}$ is the iron equilibrium potential and β_a is the tafel activation slope for the anodic reaction. Similarly, for the cathodic process, the value of the current density is given by

$$i_c = i_{0,O2} \frac{[O_2]_r}{[O_2]_b} \exp\left(2.3 \frac{E_{0,O2} - E_{corr}}{b_c}\right) \tag{2.56}$$

where $i_{0,O2}$ is the exchange current density at the equilibrium condition for the cathodic reduction, E_{corr} is the corrosion potential, $E_{0,O2}$ is the equilibrium potential of the cathodic reaction and β_c is the tafel activation slope for the cathode. Additionally, the ratio between the oxygen molar concentration at the rebar surface $[O_2]_r$ and the molar concentration in the bulk of the pore water $[O_2]_b$ is introduced to account for the limit in the current density due to the reduction of the oxygen content at the rebar surface.

As previously stated, the corrosion process takes place at a rate governed by the slower process between the anodic dissolution, the cathodic reduction, the electrons flow and the current flow in the metal. Since we consider a microcell corrosion system, the electron flow and the current flow can be considered almost instantaneous and the only limiting rate can be observed between the anodic and the cathodic rates. In any case, the corrosion equilibrium condition is achieved when

$$i_a = i_c = i_{corr} \quad at \quad E = E_{corr} \tag{2.57}$$

It is therefore possible to identify the corrosion potential by substituting eqs. 2.55 and 2.56 into 2.57 obtaining

$$E_{corr} = \frac{1}{b_a + b_c}\left[\frac{b_a \cdot b_c}{2.3}\ln\left(\frac{i_{0,O2}}{i_{0,Fe}}\frac{[O_2]_r}{[O_2]_b}\right) + b_c E_{0,Fe} + b_a E_{0,O2}\right] \tag{2.58}$$

Once the corrosion current density and the corrosion electrical potential are defined, it is possible to derive the amount of oxygen consumed as well as the amount of iron dissolved due to corrosion via the Faraday law. In particular, the Faraday law relates the amount of mass of the chemical species consumed for a given corrosion current density during a given time interval according to the following relation

$$\Delta m = \frac{i_{corr} PA}{zF}\Delta t \tag{2.59}$$

where i_{corr} is the corrosion current density, PA is the atomic or molecular mass of the reactant, z are the number of electrons consumed by the half cell reaction, F is the Faraday constant and Δt is the considered time interval. Starting from eq. 2.59, the change in radius of the steel rebar due to the formation of rust deposits can be obtained using the iron molar mass PA_{Fe}, iron density ρ_{Fe}, the iron to rust density ratio $\gamma = \gamma_{Fe}/\gamma_{Fe_2O_3}$ and the iron to rust molar mass ratio $\beta = PA_{Fe}/PA_{Fe_2O_3}$ as follows

$$\Delta r = \frac{i_{corr} PA_{Fe}}{z_{Fe} F \rho_{Fe}}\left(\frac{\gamma}{\beta} - 1\right)\Delta t \tag{2.60}$$

From the value of the radius expansion, is possible to obtain the value of the corresponding strain as the ratio between Δr and the initial radius of the rebar r. Therefore, being $\mathbb{I} \in \mathbb{R}^d$ $(d = 1, 2, 3)$ the identity tensor of rank d, the strain associated with the rust formation is given by

$$\boldsymbol{\varepsilon}_0 = \frac{\Delta r}{r}\mathbb{I} \tag{2.61}$$

Lastly, the amount of oxygen consumption at the steel surface due to the cathodic reduction can be obtained as follows

$$J_{O_2} = \frac{i_{corr}}{z_{O_2} F} \tag{2.62}$$

2.5 Oxygen diffusion

During the corrosion process the oxygen is consumed at the steel surface. Initially, the oxygen utilized in the cathodic process is taken from the initial supply present in the concrete pores [128, 129]. Eventually, as the corrosion process progress, the oxygen on the rebar surface is consumed. For the corrosion process to continue, new oxygen needs to reach the metal surface. Therefore, diffusion of oxygen through concrete represents an important aspect to consider in order to describe the real behaviour of the corrosion mechanism. Additionally, due to the corrosion process, rust deposits forms and temporary halt the oxygen and water access to the rebar surface, thus limiting the corrosion rate. However, since iron oxide is a porous material [10], oxygen and water slowly penetrate through it until the underlying metal surface is reached, increasing the corrosion to its previous higher rate.

It is therefore possible to identify two different corrosion mechanisms based on the oxygen molar concentration on the rebar surface. If the oxygen supply is in abundance over the steel rebar, the corrosion rate is controlled by the oxygen concentration at the cathode, defining a cathodic reduction controlled corrosion. Eventually, due to the cathodic reaction, oxygen is consumed and rust is produced. Therefore, as the oxygen concentration on the bar surface reduces, the corrosion current density drops to a limit value which is governed by the thickness of the rust layer and by the diffusion rate of the oxygen through it, defining a diffusion controlled corrosion. The alternation between these two different oxygen control mechanisms is an important aspect to consider in order to obtain a realistic model describing the steel rebar corrosion process [130, 131, 128, 132, 133].

2.5.1 Mathematical model for oxygen diffusion

Following a similar approach to the carbon dioxide diffusion of eq. 2.6, the diffusion of the oxygen diffusion through the concrete can be described as

$$\frac{\partial}{\partial t}\left[\xi(\varphi)\left(1-f\right)\left[O_2\right]\right] = \nabla\cdot\left(D_{O_2}(\xi(\varphi),h,\alpha)\nabla\left[O_2\right]\right) - J_{O_2} \quad in\ \Omega_c\cup\Omega_r \tag{2.63}$$

The equation accounts for the diffusion process of the oxygen through the concrete with a diffusion coefficient $\mathrm{D}_{O_2}(\xi(\varphi),h,\alpha)$ which accounts for the porosity of the concrete, the relative humidity and the presence of fractures in concrete. Additionally, from eq 2.62, the reaction term which accounts for the oxygen consumption due to the corrosion process J_{O_2} is introduced and applied to the oxygen concentration only on the rebar surface.

Following [45] the oxygen diffusion coefficient can be expressed as

$$D_{O_2}(\xi(\varphi),h,\alpha) = \xi(\varphi)^{1.8}(1-h)^{2.2}\left[1.92\cdot10^{-6}(1-\alpha)^m + 10^5\alpha^m\right] \tag{2.64}$$

The diffusion coefficient is given as a function of the material porosity, the relative humidity and the state of the material in which damage is accounted following [100] where m = 10 is assumed.

Since rust is a porous material, oxygen and water can diffuse through it. In fact, the diffusion of the oxygen through the iron oxide is also considered in the model and accordingly to [10] the diffusive properties of the rust layer can be assumed equal to the one of the carbonated concrete.

An initial concentration of the oxygen within the concrete equal to the environmental concentration is assumed ($O_2^0 = \overline{O_2}$), additionally a Dirichlet boundary condition is introduced for the oxygen diffusion on the external face of the concrete cover as follows

$$\left[O_2\right](\Omega_c,0) = \left[O_2\right]^0 \tag{2.65}$$

$$\left[O_2\right](\Gamma_c,t) = \overline{O_2} \tag{2.66}$$

Since the initial concentration of the oxygen equals the external concentration, the diffusion process of the oxygen is activated once the corrosion process of the rebar initiates as the oxygen is gradually consumed on the rebar surface.

Chapter 3

Phase field models for mechanical damage

Understanding the conditions when crack-induced failures are likely to occur is a crucial part in the design process of structures. The branch of the solid mechanics that focuses on the analysis of material rupture processes, predicting formation and advancement of cracks, is known as fracture mechanics [72, 134, 135, 136, 137]. One of its main subject is the study and definition of the physical criteria which govern the cracking behaviour of materials. Quantitative relationships are developed between the geometry of the cracks, the resistance of the material to their formation and criteria describing the process of fractures propagation through the solid.

Cracks can be seen as the macroscopic representation of the separation and rupture of the bonds between atoms at the microscopic scale. The nature of this separation can be classified in two main mechanisms [138]

- Brittle fracture - rupture of the material is sudden, often catastrophic, and occurs without visible macroscopic deformation. Fracture propagation is usually abrupt and unstable. This typology of fracture involves small amounts of energy dissipation and is characteristic of brittle and quasi-brittle materials such as concrete, rocks, glass, ceramics and metals at low temperatures [139];

- Ductile fracture - rupture of the material follows plastic deformations before ultimate failure. It is usually associated with a stable fracture propagation through the material and this behaviour is typical of metal at room or higher temperatures [140].

Extensive efforts have been made to develop models which can approximate and predict the different rupture behaviour of material using numerical approaches [141, 142, 143]. The possibility to accurately reproduce the material behaviour to crack nucleation and growth via numerical simulations, avoiding long and costly experimental campaigns, represent one of the most appealing feature of the computational fracture mechanics.

Fracture process in solids have been computationally investigated using two main methodologies: discrete [144, 145, 146] and smeared [147, 148, 149] representations. Distinction between these approaches lies in the kinematic description of cracks within the body.

In discrete approaches, fractures are introduced as a discontinuity in the displacement field across the fracture surface. A sharp interface between the two separated portion of the

body is observed. Discrete approaches includes the classical theory of linear elastic fracture mechanics (LEFM) [72, 134] as well as cohesive zone models [150, 151].

In continuous (or smeared) approaches instead, the displacement field remains continuous through cracks. Strong discontinuities within the domain are approximated as strain localizations within a finite thin band. Here, a reduction of stresses is introduced to account for the material degradation process induced by fracture. Popular models which belongs to the smeared approach to fracture are the phase field approach [152] and peridynamics [153].

3.1 Phase field fracture models

Derived from the variational approach to brittle fracture presented in [152], and generalizing Griffith's theory [72], the phase field models is a smeared approach to fracture in which cracks within a body are represented as bands of non-zero thickness in which degradation of the material strength is observed.

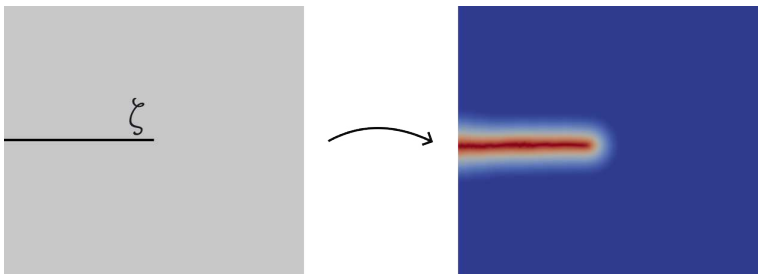

Figure 3.1: Smeared approximation of a crack set ζ via phase field model.

The equilibrium state of a cracked body is derived as the solution of the minimization problem of its total potential energy, which is obtained as the sum of two contributions:

- Elastic energy (Ψ): this term correspond to the elastic energy stored within the body at its equilibrium configuration containing a crack set ζ;
- Surface energy(ψ) this term accounts for the energy required to break the bonds between the atoms of the material thus crating an new crack surface within it. It is therefore proportional to the area of the crack surface.

The total potential energy of the cracked body, in absence of body forces or surface tractions, reads as

$$\Pi(\zeta) = \Psi + \psi \tag{3.1}$$

Evolution of cracks is therefore defined as the minimization of the total potential energy of 3.1 with the addition of an irreversibility condition to avoid self healing of cracks. If two subsequent time $t-1$ and t are considered, the following irreversibility condition is applied to the crack set

$$\zeta^{t-1} \subset \zeta^{t} \tag{3.2}$$

while the governing equations for the total potential energy read as

$$\Pi(\zeta^t) \leq \Pi(\zeta^{t-1}) \quad \forall \zeta^t \supset \zeta^{t-1} \tag{3.3}$$

Eq. 3.3 shows the potential of the phase field approach to fracture. Accounting for the irreversibility condition 3.2, the value of the total potential energy for the current crack set $\Pi(\zeta^t)$ can only be less or equal to its previous value $\Pi(\zeta^{t-1})$. This leads to the definition of the criterion which governs nucleation and propagation of cracks within the material. Cracks nucleation is determined via the comparison between the elastic energy of the undamaged body and the total energy of the body including any possible crack set. If the total potential energy of the cracked body presents a lower value compared to its value in the undamaged state, crack nucleation is observed. Following a similar procedure, comparing the total energy of the body containing a crack set ζ with the total energy of the body containing any possible evolution of that crack set allows to describe the fracture propagation process without requiring any a-priori knowledge of the crack evolution path.

Since rupture of the material is defined via the minimization of an energetic functional, phase field models presents great capabilities to accurately reproduce complex crack topologies as well as fracture nucleation, propagation and more complex fracture processes such as crack branching and merging without the need of ad-hoc conditions for material rupture or a-priori knowledge of possible crack paths.

3.1.1 Phase field approach to brittle fracture

The application of the phase field model for quasi-static brittle fracture is now presented. Let consider a brittle solid $\Omega \in \mathbb{R}_d$ $(d = 1, 2, 3)$ with boundary Γ in which imposed displacements $\bar{\mathbf{u}}$ are applied on the portion Γ^u. Additionally, a crack set $\zeta \in \mathbb{R}^{d-1}$ may occur on the body.

The phase field can be seen as a free discontinuity problem in which cracks introduce displacement discontinuities in the body [154]. Considering the displacement field of the brittle solid $\mathbf{u}$, it is possible to obtain the total energy functional as a function of the symmetric part of the displacement field gradient $\boldsymbol{\varepsilon} = \nabla^s \mathbf{u} = \frac{1}{2}(\nabla \mathbf{u} + \nabla \mathbf{u}^T)$ and the crack set ζ as follows

$$\Pi(\boldsymbol{\varepsilon}, \zeta) = \int_{\Omega \setminus \zeta} \Psi(\boldsymbol{\varepsilon}) \, d\Omega + Gc \, \texttt{meas}(\zeta) \tag{3.4}$$

where $\Psi(\boldsymbol{\varepsilon}) = \frac{1}{2}\mathbb{C}\boldsymbol{\varepsilon} \cdot \boldsymbol{\varepsilon}$ is the quadratic strain energy density with $\mathbb{C}$ the fourth order elasticity tensor of the material, Gc is the fracture toughness and `meas` is the $d-1$ Hausdorff measure [155]. The contribution to the total energy of the second term of eq. 3.4 represents the fracture energy contribution which is proportional to the crack surface length ζ through the fracture toughness Gc. The fracture toughness can be regarded as a material property.

Via the minimization of the energetic functional expressed in 3.4, it is possible to retrieve the pair $(\mathbf{u}^*, \zeta^*)$ which defines the quasi-equilibrium condition for the solid Ω and it is therefore obtained by solving the following free-discontinuity problem

$$(\mathbf{u}^*, \zeta^*) = \text{Arg}\left\{\min\left\{\Pi(\boldsymbol{\varepsilon}, \zeta)\right\}\right\} \tag{3.5}$$

The irreversibility condition on the crack set from eq. 3.2 has to be introduced to prevent healing of cracks within the material between two subsequent time interval t and $t + \Delta t$ such as

$$\zeta(t) \leq \zeta(t + \Delta t) \tag{3.6}$$

In order to numerically implement and study the free-discontinuity problem expressed in 3.5, [156] proposed the so-called regularized variational fracture model in which the energy functional of eq. 3.4 is approximated in a $\Gamma-$convergence sense to an approximated energy functional obtained via the introduction of a scalar field variable, or phase field variable, $\alpha : \Omega \to [0, 1]$ which takes care of the crack surface term. The variable α represents the internal state of the material and it assumes the value $\alpha = 0$ for the sound material while $\alpha = 1$ means that the cohesion of the material is fully lost. The phase field can be seen as a damage variable which describes cracks in a smeared way. However, since cracks are now represented as bands of non-zero thickness in which the phase field rapidly changes value from 0 to 1, a length scale parameter $\ell \in \mathbb{R}^+$ is introduced to govern the width of the transition zone from broken to unbroken material. The parameter ℓ can be considered as a material parameter [157]. Therefore, the surface energy term of eq. 3.4 is approximated as follows

$$Gc\,\texttt{meas}(\zeta) \;\sim\; \psi(\alpha) = \frac{Gc}{c_w} \int_\Omega \left(\frac{w(\alpha)}{\ell} + \ell ||\nabla \alpha||^2 \right) d\Omega \tag{3.7}$$

where $w(\alpha)$ is a strictly increasing function which describes the local damage dissipation during the evolution of the crack set, $|| \cdot ||$ is the standard Euclidean norm and c_w is a normalization coefficient which depends on $w(\alpha)$ as follows

$$c_w = \int_0^1 \sqrt{w(\alpha) d\alpha} \tag{3.8}$$

The strain energy part of the total energy is also modified accordingly to almost vanish in the fully damaged portion of the domain. A strictly decreasing degradation function $g(\alpha)$ is introduced to account for the stiffness degradation of the broken material. Additionally, the coefficient $k_l = o(\ell)$ is added to render coercive the functional and act as a residual stiffness in the fully damaged portion of the domain. Therefore the strain energy reads

$$\Psi(\boldsymbol{\varepsilon}, \alpha) = \int_\Omega (a(\alpha) + k_l) \left(\frac{1}{2} \mathbb{C}\boldsymbol{\varepsilon} \cdot \boldsymbol{\varepsilon} \right) d\Omega \tag{3.9}$$

Lastly, the approximated total energy functional reads as

$$\Pi_l(\boldsymbol{\varepsilon}, \alpha) = \int_\Omega (a(\alpha) + k_l) \left(\frac{1}{2} \mathbb{C}\boldsymbol{\varepsilon} \cdot \boldsymbol{\varepsilon} \right) d\Omega + \frac{Gc}{c_w} \int_\Omega \left(\frac{w(\alpha)}{\ell} + \ell ||\nabla \alpha||^2 \right) d\Omega \tag{3.10}$$

Two different choices for the damage functions originate from the work of Ambrosio and Tortorelli which are widely used in the literature, namely:

- AT1 model [158]: $a(\alpha) = (1 - \alpha)^2$, $w(\alpha) = \alpha$, $c_w = 3/8$
- AT2 model [156]: $a(\alpha) = (1 - \alpha)^2$, $w(\alpha) = \alpha^2$, $c_w = 2$

If a 1D traction setting is considered, it is possible to obtain the analytical expression for the optimal damage profile, which is described over the orthogonal section to a crack within the body. Based on the chosen damage model, two different expression of the damage

profile can be obtained. If x_0 is considered the location where $\alpha = 1$, for the AT1 model the expression of the optimal damage profile is given as

$$\alpha(x) = \begin{cases} \left(1 - \frac{|x-x_0|}{2\ell}\right)^2 & if\ x \in [x_0 - 2\ell; x_0 + 2\ell] \\ 0 & elsewhere \end{cases} \tag{3.11}$$

while for the AT2 model is

$$\alpha(x) = \exp\left(-\frac{|x - x_0|}{\ell}\right) \tag{3.12}$$

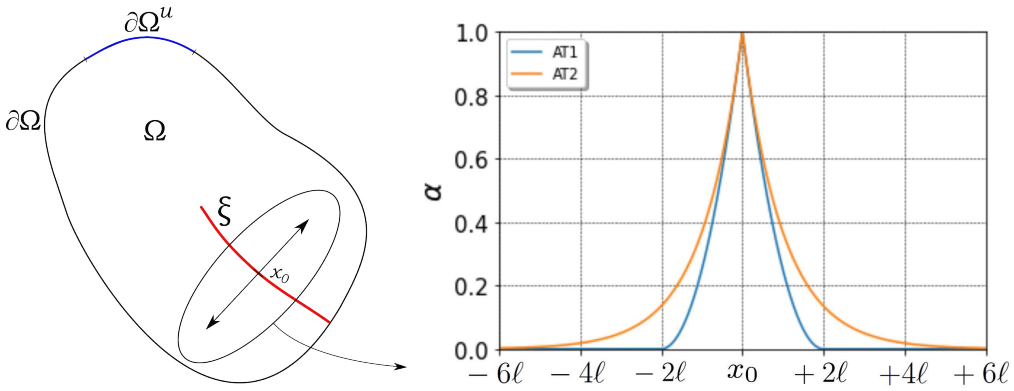

Figure 3.2: Optimal damage profile for the AT1 and the AT2 damage models.

Fig. 3.3 reports the optimal damage profiles for both the AT1 and the AT2 model. For the AT1 model, the phase field assumes a value different from zero in a limited portion of the domain. In particular, the transition zone between the maximum value and zero affects a distance equal to 2ℓ on each side from x_0. The AT2 model presents a continuous profile going from the max value to zero which affects a wider area around the crack location x_0.

Starting from the expression of the approximated total energy functional 3.10, it is possible to define a new minimization problem which, under appropriate boundary conditions, reads as follows

$$(\mathbf{u}^*, \alpha^*) = \text{Arg}\left\{\min\left\{\Pi_l(\boldsymbol{\varepsilon}, \alpha)\right\}\right\}\ \ subjected\ to\ \ \dot{\alpha} \geq 0,\ \ \alpha \in [0, 1] \tag{3.13}$$

The equations governing the minimization problem 3.13 of the approximated functional can be obtained by considering its first derivative with respect to the displacement field and to the phase field giving the following Euler-Lagrange equations, one for the displacement field and one for the phase field

$$\begin{cases} \text{div}\mathbf{T} = 0 & in\ \Omega, \quad (a) \\ \frac{Gc}{c_w}\left(\frac{w(\alpha)'}{\ell} - 2\ell\Delta\alpha\right) + \frac{\partial\Psi_s}{\partial\alpha} = 0 & in\ \Omega, \quad (b) \end{cases} \tag{3.14}$$

where $\mathbf{T}$ is the Cauchy stress tensor and $\frac{\partial\Psi}{\partial\alpha}$ is the crack driving force defined as

$$\mathbf{T} = (a(\alpha) + k_l)\frac{1}{2}\mathbb{C}\boldsymbol{\varepsilon}; \quad \frac{\partial\Psi}{\partial\alpha} = a(\alpha)'\mathbb{C}\boldsymbol{\varepsilon} \cdot \boldsymbol{\varepsilon} \tag{3.15}$$

Lastly, adding the irreversibility condition of eq. 3.6 to the Euler-Lagrange equation 3.14(b), yields the following Karush-Kuhn-Tucker conditions which govern the rupture process of a quasi-brittle solid:

$$\begin{cases} \frac{Gc}{c_w}\left(\frac{w(\alpha)'}{\ell} - 2\ell\Delta\alpha\right) + \frac{\partial\Psi_s}{\partial\alpha} = 0 & (a) \\ \dot{\alpha} \geq 0 & (b) \\ \left(\frac{Gc}{c_w}\left(\frac{w(\alpha)'}{\ell} - 2\ell\Delta\alpha\right) + \frac{\partial\Psi_s}{\partial\alpha}\right)\dot{\alpha} = 0 & (c) \end{cases} \tag{3.16}$$

3.1.2 Phase field model for traction-compression asymmetrical rupture behaviour

Via the modification of the strain energy density of the functional in eq. 3.9 or modifications of the surface energy density of eq 3.7, the phase field approach to brittle fracture allows to investigate a wide variety of material behaviours.

Asymmetric rupture behaviour in traction and compression has been investigated in different works [159, 13, 77, 160]. These approaches consists in an additive split of the elastic energy of eq 3.9 in its positive and negative parts with the damage degradation function acting only on the positive part such that

$$\Psi(\boldsymbol{\varepsilon}, \alpha) = a(\alpha)\Psi^{+}(\boldsymbol{\varepsilon}) + \Psi^{-}(\boldsymbol{\varepsilon}) \tag{3.17}$$

Following [77], the positive and the negative part of the strain energy are obtained via an additive spectral decomposition of the strain tensor in its positive and negative parts as $\boldsymbol{\varepsilon} = \boldsymbol{\varepsilon}^{+} + \boldsymbol{\varepsilon}^{-}$. The split of the strain tensor is performed starting from the following decomposition

$$\boldsymbol{\varepsilon} = \sum_{i=1}^{d} \varepsilon_i \boldsymbol{n} \otimes \boldsymbol{n} \tag{3.18}$$

where ε_i are the ordered eigenvalues ($\varepsilon_i \geq \varepsilon_{i+1}$) with $\boldsymbol{n}_i$ the corresponding eigenvectors. If a plain strain condition with d = 2 is considered, the positive and the negative part of the deformation tensor are defined as follows

$$if\ \varepsilon_2 \geq 0 \tag{3.19}$$

$$\begin{cases} \boldsymbol{\varepsilon}^+ \leftarrow \boldsymbol{\varepsilon} \\ \boldsymbol{\varepsilon}^- \leftarrow 0 \end{cases} \tag{3.20}$$

$$if\ (1-\nu)\varepsilon_1 + \nu\varepsilon_2 > 0\ and\ \varepsilon_2 < 0 \tag{3.21}$$

$$\begin{cases} \boldsymbol{\varepsilon}^+ = \begin{bmatrix} \varepsilon_1 + \frac{\nu}{1-2\nu}\varepsilon_2 & 0 \\ 0 & 0 \end{bmatrix} \\ \boldsymbol{\varepsilon}^- = \begin{bmatrix} -\frac{\nu}{1-2\nu}\varepsilon_2 & 0 \\ 0 & \varepsilon_2 \end{bmatrix} \end{cases} \tag{3.22}$$

$$if\ (1-\nu)\varepsilon_1 + \nu\varepsilon_2 \leq 0 \tag{3.23}$$

$$\begin{cases} \boldsymbol{\varepsilon}^+ \leftarrow 0 \\ \boldsymbol{\varepsilon}^- \leftarrow \varepsilon \end{cases} \tag{3.24}$$

$$\tag{3.25}$$

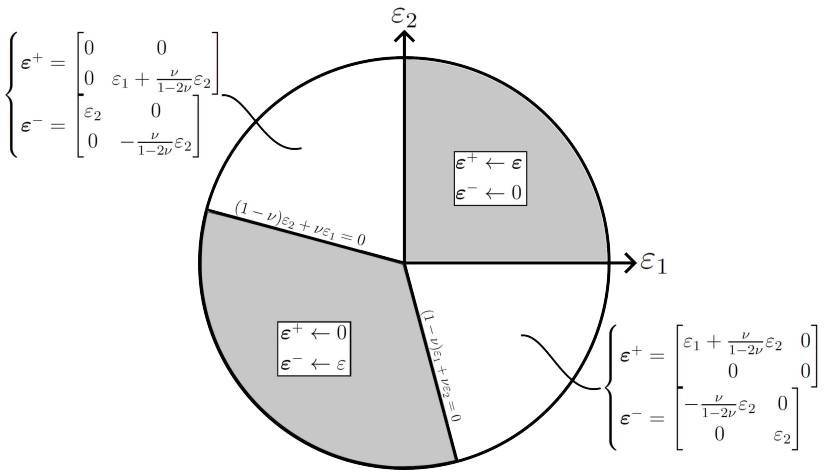

Figure 3.3: Calculation of the traction-compression split for the strain tensor for $\nu = 0.2$.

By substituting the positive and negative strain tensors of eq. 3.19 into the definition of the modified energy functional of eq. 3.17, it is possible to write

$$\Psi^+(\boldsymbol{\varepsilon}^+, \alpha) = (a(\alpha) + k_l)\,\frac{1}{2}\mathbb{C}\boldsymbol{\varepsilon}^+ \cdot \boldsymbol{\varepsilon}^+; \quad \Psi^- = \frac{1}{2}\mathbb{C}\boldsymbol{\varepsilon}^- \cdot \boldsymbol{\varepsilon}^- \ . \tag{3.26}$$

This modification permits to consider the rupture of the material only due to tensile stresses applied to the material. Additionally, an unilateral contact effect is implicitly introduced between two portion of the material divided by a crack under closure. Therefore, while the tensile resistance of the broken material is completely reduced to zero due to the phase field, compressive stresses are still present and transmitted through cracks. From 3.26 it is possible to obtain the Cauchy stress tensor and the crack driving force by differentiating with respect to the strain tensor and to the phase field variable respectively, giving

$$\mathbf{T} = (a(\alpha) + k_l)\frac{1}{2}\mathbb{C}\boldsymbol{\varepsilon}^+ + \frac{1}{2}\mathbb{C}\boldsymbol{\varepsilon}^-; \quad \frac{\partial \Psi}{\partial \alpha} = a(\alpha)'\mathbb{C}\boldsymbol{\varepsilon}^+ \cdot \boldsymbol{\varepsilon}^+ \tag{3.27}$$

Changes to $\mathbf{T}$ and to $\partial\Psi/\partial\alpha$ permit to better observe that only the portion of the domain under tensile load are affected by the degradation of the material stiffness and more importantly cracks can nucleate only due to tensile stresses. Therefore the total potential energy which accounts for the different rupture behaviour of the material between traction and compression reads

$$\begin{aligned}\Pi_l(\boldsymbol{\varepsilon}, \alpha) = \int_\Omega \left[(a(\alpha) + k_l) \left(\frac{1}{2}\mathbb{C}\boldsymbol{\varepsilon}^+ \cdot \boldsymbol{\varepsilon}^+\right) + \left(\frac{1}{2}\mathbb{C}\boldsymbol{\varepsilon}^- \cdot \boldsymbol{\varepsilon}^-\right)\right] d\Omega + \\ + \frac{Gc}{c_w}\int_\Omega \left(\frac{w(\alpha)}{\ell} + \ell||\nabla\alpha||^2\right) d\Omega\end{aligned} \tag{3.28}$$

3.2 Representative examples

3.2.1 Uniaxial traction of bar

A simple traction test of a rectangular domain is presented to analyse the phase field approach to brittle fracture. The standard functional of eq. 3.10 has been considered with AT1 damage functions. Following [161], a rectangular domain of L = 1 mm and H = 0.1 mm is considered. A monotonic increasing horizontal displacement $\bar{\mathbf{u}} = 3t\mathrm{L}$, with $t \in [0, 1]$ a time like parameter, is applied on the right boundary while the left boundary is kept fixed. An additional boundary condition on the phase field is introduced on the left and right domain boundaries to avoid rupture along the constrained borders.

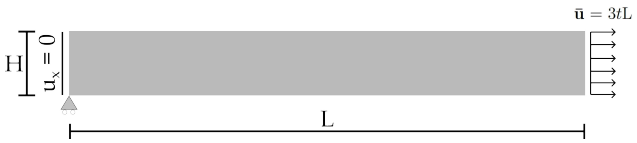

Figure 3.4: Domains considered for the mechanical problem and their respective energetic functional.

The considered material properties are the following: Young modulus E = 1MPa, Poisson's ratio $\nu = 0.3$, fracture toughness $Gc = 1$ N/mm and internal length parameter $\ell = 0.1$ mm. Fig. 3.5(a) reports the results for the damage field while fig. 3.5(b) reports the damage profile obtained from the numerical simulation and the optimal damage profile for the AT1 model.

A shift of the plateau value $\alpha = 1$ equal to $d/2$, where d is the cell size of the mesh elements, is present in the damage profile obtained form the numerical results. The difference between the two profiles can be accounted by the finite element implementation of the model in which fracture is represented by a single band of fully damaged elements. However, the transition zone between the fully damaged elements and the unbroken portion of the material recovers correctly the optimal damage profile covering an area equal to 2ℓ as presented in eq. 3.11.

The energy profiles are presented in fig. 3.6(a). Here it is possible to observe that for the AT1 model the elastic energy increases up to the formation of the crack. An initial pure

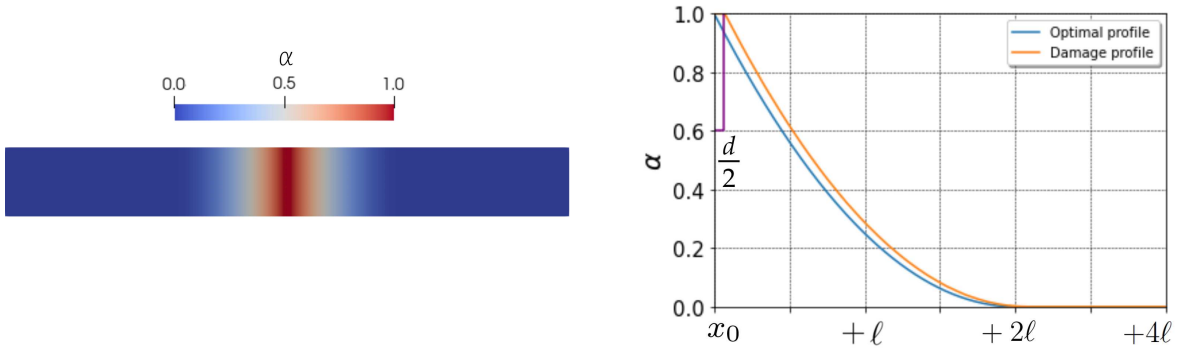

a) b)

Figure 3.5: Uniaxial traction test: a) damage field; b) plot of the damage profile.

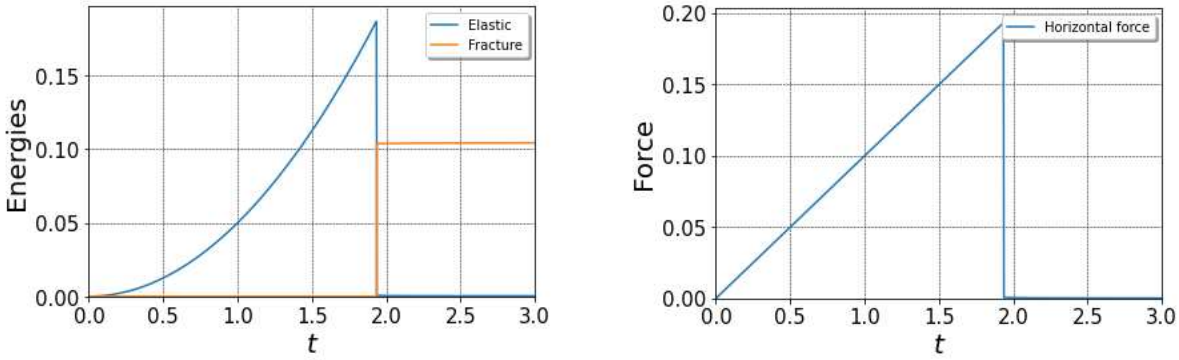

a) b)

Figure 3.6: Uniaxial traction test: a) plot of the elastic and surface energies; b) plot of the forces.

elastic phase without damage is described up to a critical value of the loading parameter t_c equal to $t_c = \sqrt{3G_c/8E\ell} \sim 1.94$ [161]. Once damage in the bar is observed, the elastic energy vanishes and the fracture energy increase to a value corresponding to its theoretical value $\psi_{frac} = GcH = 0.1$. However, it can be noted that the fracture energy assumes a higher value higher once the crack is fully developed. The additional contribution to the fracture energy is given by the fully damaged finite element band. The effective value of the fracture energy $\psi_{frac,eff}$ can be evaluated as follows

$$\psi_{frac,eff} = \psi_{frac} \cdot \frac{1}{\left(1 + \frac{3d}{8\ell}\right)} \tag{3.29}$$

where ψ_{frac} is the value of the approximated fracture energy obtained from the finite element approximation. Additional details can be found in [148, 162, 81, 163]. Lastly, fig. 3.6(b) reports the plot for the horizontal force with respect to the loading parameter. A monotone increase of the force is observed until the fracture appears into the domain leading to the brittle rupture of the material which can be observed as the force goes to zero once fracture is formed.

3.2.2 Standard functional vs split functional: pure bending test

Now the energetic functional which accounts for the traction compression anisotropy of eq. 3.28 is compared with the standard functional for the phase field model for brittle fracture of eq. 3.10. AT1 damage functions have been used. A rectangular domain of L = 1 and H = 0.1 has been studied where displacements were blocked on the left side while on the right side horizontal displacements have been imposed such that the upper portion of the beam is compressed while the lower half of the beam is under traction with the neutral axis placed at $y = 0.5$H. The following linear relationship is used $\bar{\mathbf{u}} = t(0.5 - y/H)$ where y is the coordinate corresponding to the height of the beam and $t \in [0, 0.05]$ a time like parameter controlling the intensity of the applied displacements. The following material properties have been considered: Young's modulus E = 210000 MPa, Poisson's ratio $\nu = 0.3$, fracture toughness $Gc = 2.7$ N/mm and internal length parameter $\ell = 0.035$ mm.

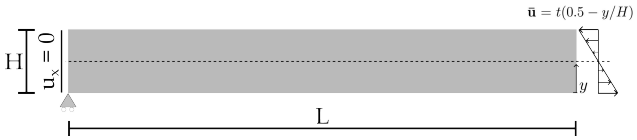

Figure 3.7: Domains considered for the mechanical problem and their respective energetic functional.

Fig. 3.8(a) reports the damage profiles for the pure bending test performed using the standard total energy functional of eq. 3.10 while the damage profile obtained using the traction-compression split is reported in fig. 3.8(b). The damage profile obtained from the standard energetic functional affects both the upper and the lower portion of the beam since compression stresses are accounted into the crack driving force. For the modified functional however, the damage field interests only the lower portion of the beam which is under traction with the upper portion being unaffected by damage

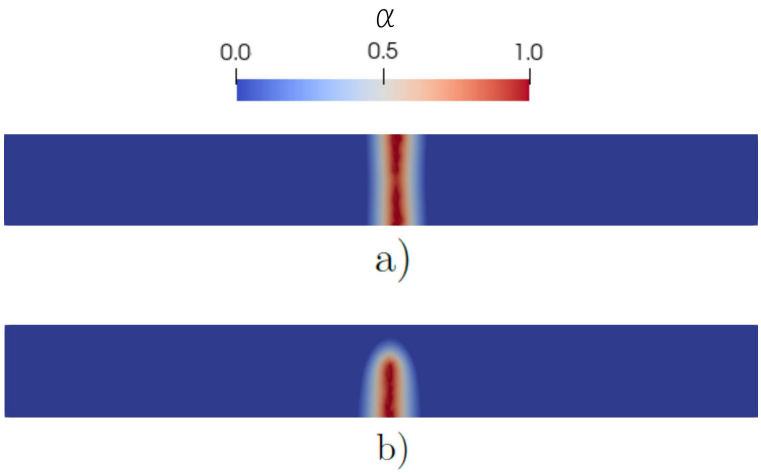

Figure 3.8: Pure bending test: a) damage field for the standard energy functional of eq. 3.10; b) damage field for the splitted energy functional of eq. 3.28.

Fig. 3.9 reports the normalized value of the elastic and fracture energies with respect to their corresponding maximum value for both the standard and the modified total energy

functional. The energy curves for the standard energy functional follows a similar path compared to what has been observed previously in 3.6(a). Here, fracture affects both the portion of the beam under compression and traction, thus leading to the drop of the elastic energy to zero while, at the same time, the surface energy reaches its maximum value and no further evolution of fracture is observed. On the other hand, the energy curves obtained from the modified functional show that only the positive part of the energy is affected by the degradation function, dropping to a lower value once crack is formed. The negative portion of the elastic energy instead, keeps increasing throughout the test since it is not affected by damage.

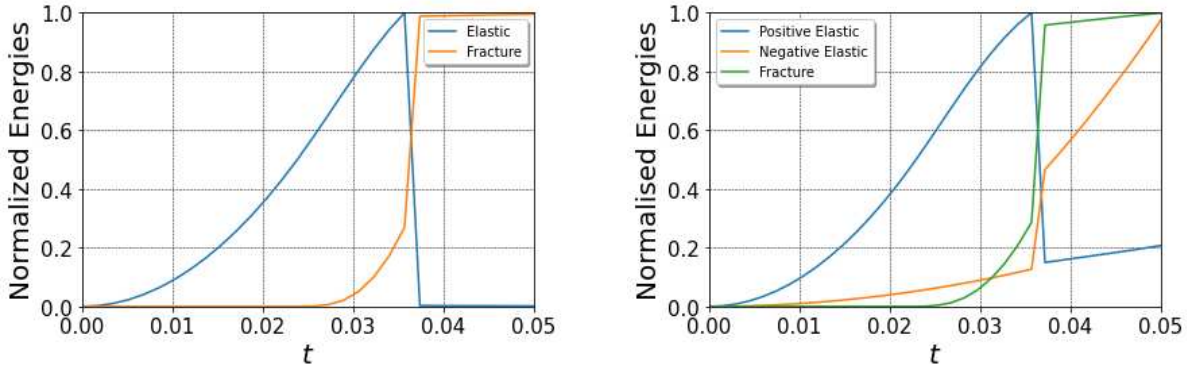

a) b)

Figure 3.9: Normalized energy values for the pure bending test: a) standard energy functional of eq. 3.10; b) splitted energy functional of eq. 3.28.

3.3 Application to the cracking of concrete cover

The application of the phase field to reinforced concrete follows the approach presented in [7]. The total potential energy includes the contributions form the different portion of the domain. In particular, the energetic functional considered in the model is obtained as the sum of the elastic and surface energy for the concrete while for the steel and rust portion of the domain only the elastic energy is considered. The loading parameter that describes the evolution of damage within concrete cover is defined starting from the physical-chemical processes which characterise carbonation corrosion phenomena of reinforced concrete elements. Once the carbonation profile is obtained, it is possible to perform an accurate evaluation of rust distribution over the steel rebar perimeter using eq. 2.60. Eventually, associated strains ε_0 are calculated using eq. 2.61 and introduced in the expression of the potential energy of rust, characterizing the rise of overpressures within concrete cover which leads to formation of cracks.

The energetic functional of each portion of the domain accounts for the different physical processes affecting each material.

- Concrete: the energetic functional considers the split presented in eq. 3.26 to account for the anisotropy rupture behaviour of the concrete. Therefore, to account for the tensile anisotropy behaviour of concrete, the degradation function $a(\alpha)$ is only applied

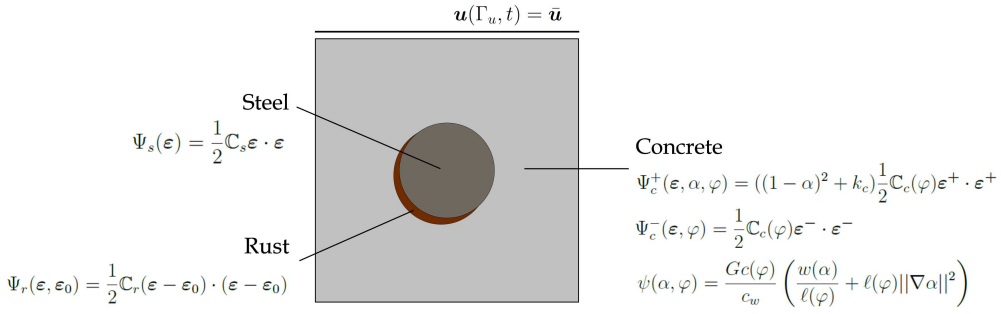

Figure 3.10: Domains considered for the mechanical problem and their respective energetic functional.

to the tensile part of the elastic energy. The changes of the concrete mechanical properties due to the carbonation process are also accounted in the fourth order elasticity tensor $\mathbb{C}_c(\varphi)$, the fracture toughness $G_c(\varphi)$ and the internal length parameter $\ell(\varphi)$. Since, cracks can only nucleate on the concrete cover, the surface energy is defied only over the concrete domain. The concrete energetic functional reads

$$\Psi_c^+(\boldsymbol{\varepsilon}, \alpha, \varphi) = ((1-\alpha)^2 + k_c)\frac{1}{2}\mathbb{C}_c(\varphi)\boldsymbol{\varepsilon}^+ \cdot \boldsymbol{\varepsilon}^+ \tag{3.30}$$

$$\Psi_c^-(\boldsymbol{\varepsilon}, \varphi) = \frac{1}{2}\mathbb{C}_c(\varphi)\boldsymbol{\varepsilon}^- \cdot \boldsymbol{\varepsilon}^- \tag{3.31}$$

$$\psi(\alpha, \varphi) = \frac{Gc(\varphi)}{c_w}\left(\frac{w(\alpha)}{\ell(\varphi)} + \ell(\varphi)||\nabla\alpha||^2\right) \tag{3.32}$$

- Steel: for the steel rebar the considered energetic functional is the classical strain energy

$$\Psi_s(\boldsymbol{\varepsilon}) = \frac{1}{2}\mathbb{C}_s\boldsymbol{\varepsilon} \cdot \boldsymbol{\varepsilon} \tag{3.33}$$

- Rust: the rust portion of the domain accounts for the inelastic deformation $\boldsymbol{\varepsilon}_0$ associated with the formation of the rust deposits due to the corrosion process of the steel rebar. Starting from the rebar expansion given from eq. 2.60, it is possible to obtain the associated deformation by dividing its value by the initial radius of the steel rebar

$$\boldsymbol{\varepsilon}_0 = \frac{\Delta r}{r}\mathbb{I} \tag{3.34}$$

where r is the initial radius of the steel rebar and $\mathbb{I} \in \mathbb{R}$ $(d = 1, 2, 3)$ is the identity tensor of rank d. The energetic functional for the rust domain reads

$$\Psi_r(\boldsymbol{\varepsilon}, \boldsymbol{\varepsilon}_0) = \frac{1}{2}\mathbb{C}_r(\boldsymbol{\varepsilon} - \boldsymbol{\varepsilon}_0) \cdot (\boldsymbol{\varepsilon} - \boldsymbol{\varepsilon}_0) \tag{3.35}$$

Where $\mathbb{C}_c(\varphi)$, $\mathbb{C}_s$ and $\mathbb{C}_r$ are the fourth order elasticity tensor for the concrete, steel and rust respectively. The mechanical parameters for the rust has been taken from [164]. By

adding together the various expression of the energy for each domain (3.30, 3.33, 3.35) the following total potential energy for the reinforced concrete is obtained

$$\begin{aligned}\Pi_{rc}(\boldsymbol{\varepsilon}, \boldsymbol{\varepsilon_0}, \alpha, \varphi) = \int_{\Omega_c} \left[\Psi_c^+(\boldsymbol{\varepsilon}, \alpha, \varphi) + \Psi_c^-(\boldsymbol{\varepsilon}, \varphi)\right] \, d\Omega_c + \int_{\Omega_c} \psi(\alpha, \varphi) \, d\Omega_c + \\ + \int_{\Omega_s} \Psi_s(\boldsymbol{\varepsilon}) \, d\Omega_s + \int_{\Omega_r} \Psi_r(\boldsymbol{\varepsilon}, \boldsymbol{\varepsilon}_0) \, d\Omega_r\end{aligned} \tag{3.36}$$

Lastly, to complete the formulation, appropriate boundary conditions on the displacement field are introduced on the boundaries of the concrete portion of the domain as follows

$$\boldsymbol{u}(\Gamma_u, t) = \bar{\boldsymbol{u}} \tag{3.37}$$

Chapter 4

Numerical model for carbonation corrosion phenomena in reinforced concrete elements

Application of numerical models to the study of different reinforced concrete behaviours proved to be an highly effective method to significantly increase the knowledge and understanding of the material. Different degradation processes have been numerically investigated throughout the years.

Moisture behaviour and transport in concrete has been modelled in [57, 114, 50, 51] in terms of relative humidity while a different approach in which the degree of pore saturation is considered has been presented in [165, 52]. Also, capillary water absorption into mortar samples is numerically investigated in [166] and in [167] movement of moisture through crack in view of their self healing is studied.

Reactive transport processes are also a topic highly studied within the framework of numerical modelling. A model for chloride ions penetration under cyclic drying-wetting loading is presented in [168], while in [169] a self-sufficient framework to investigate the reactive transport processes of chlorides is proposed. Carbonation of concrete is numerically investigated in [53, 54, 8].

Corrosion of the rebar in reinforced concrete structures and elements is studied in [58, 59, 170, 171, 172]. The lost of adherence between the steel and the concrete at their interface due to the formation of rust associated with the corrosion of the reabar has also been investigated in [173]. Numerous investigations were made for the cracking of the concrete cover due to corrosion such as in [174, 175, 176, 177].

Referring to the modeling of cracks within reinforced concrete elements using the phase field approach to fracture, in [178] a chemo-thermo-mechanical model describes the formation of fracture associated with the essication of concrete in young stages. Non-uniform corrosion of the rebar leading to the rupture of the concrete cover is studied in [7, 179, 180]. In [177] the meso scale modelling of concrete is studied in which effects of the aggregates within the mortar on the crack paths are considered.

The current work aims to expanding the model initially presented in [7]. The carbonation induced corrosion process introduced in sec. 2 is coupled with the phase field of fracture presented in sec. 3 to analyse the degradation phenomena affecting reinforced concrete elements due to the effects of the surrounding environment. Via its numerical implementation, the developed method aims to accurately reproduce the rupture of the cover

of reinforced concrete elements due to the corrosion of the rebar. In the following, details on the numerical implementation of the model disclosed in the previous chapters are discussed. The structure of the algorithm and the solution strategies applied for the analysis of each single process are presented.

4.1 The developed model

The developed predictive model for the carbonation corrosion phenomena in reinforced concrete elements investigates the degradation process via the numerical implementation of the physical processes described in sec. 2. The model numerically solves the partial differential equations describing the different physical process via the usage of finite element method (FEM) [181, 182, 183]. The physical domain Ω has been discretized using a mesh of n_e quadrilateral elements of cell size cs. Over each element, a set of linear shape functions is considered to approximate over the discrete mesh the physical quantities. A representative discretization of the physical domain is reported in fig. 4.1, here blue elements correspond to concrete (Ω_c), red elements correspond to rust (Ω_r) while grey elements correspond to steel (Ω_s).

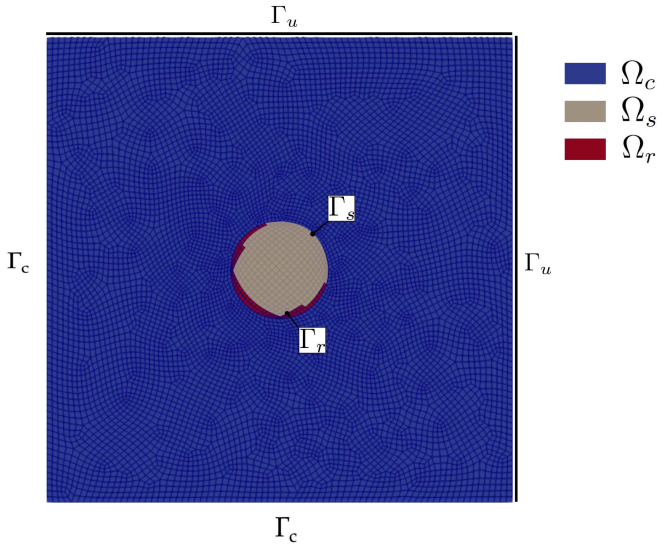

Figure 4.1: Discretization of the physical domain.

The numerical model requires the solution of time dependent partial differential equations which are numerically investigated using a fully implicit finite element scheme in which the time variable is discretized using a central difference scheme [182, 184]. Additionally, the simulated time interval considered during the simulations $[0, \mathrm{T}_{tot}]$ has been subdivided into n_t equally-sized smaller time increments $\Delta t = t^{i+1} - t^i$ with $i = 0, ..., n_t$.

All the numerical simulations have been performed using the open-source finite element computing platform for solving partial differential equations DEAL.II [185, 186].

4.1.1 Initial values setup

The first step of the algorithm consists in the setup of the initial values for each sub-problem at time $t = 0$. Thus, the initial values for the moisture concentration are

applied to the concrete portion of the domain as follows

$$h(\Omega_c, t=0) = h^0 \quad in\ \Omega_c \tag{4.1}$$

Similarly, for time $t = 0$ the carbon dioxide, the calcium hydroxide and the calcium carbonate concentrations are set as follows

$$[CO_2](\Omega_c, t=0) = 0 \qquad in\ \Omega_c \tag{4.2}$$
$$[Ca(OH)_2](\Omega_c, t=0) = [Ca(OH)_2]^0 \qquad in\ \Omega_c \tag{4.3}$$
$$[CaCO_3](\Omega_c, t=0) = 0 \qquad in\ \Omega_c \tag{4.4}$$

Lastly, the initial oxygen concentration is set on the concrete portion of the domain following

$$[O_2](\Omega_c, t=0) = [O_2]^0 \quad in\ \Omega_c \tag{4.5}$$

Once the initial values are set over the domain, the carbonation corrosion phenomena in reinforced concrete elements is described via the numerical solution of the equations previously presented in sec. 2. The procedure used for the numerical solution of each time dependent equation is presented, describing the evolution of carbonation corrosion process from an arbitrary current time step t to the incremental time step $t + 1 = t + \Delta t$. During each time increment, the algorithm models the degradation phenomena in five main stages:

1 - moisture transport;

2 - carbon dioxide diffusion-reaction process;

3 - corrosion of the steel rebar;

4 - oxygen diffusion;

5 - rupture of the concrete cover.

4.1.2 Moisture transport

For each time increment, the initial step of the algorithm consists in the numerical solution of the transport equation given by eq. 2.31 with the appropriate boundary conditions expressed in eq. 2.48.

The evolution through time of the moisture content in concrete is numerically described via the discretization of eq. 2.31 using a fully implicit numerical scheme, in which a central difference scheme has been employed to account for the time variable. Being h^t the value of the relative humidity at the current time t, the discretized equation which provides the value for the relative humidity h^{t+1} at the time increment $t + 1$ reads as

$$\left(\frac{\partial W}{\partial h}\right)^t \frac{h^{t+1} - h^t}{\Delta^t} = \nabla \cdot (D_h^t \nabla h^{t+1}) \quad in\ \Omega_c \tag{4.6}$$

with Neumann boundary conditions

$$J_h(\Gamma_c, t) = B_h(h^t - \overline{h}_{en}) \tag{4.7}$$

In order to solve eq. 4.6, the value for the moisture capacity $\partial W/\partial h$ as well as for the moisture diffusion coefficient D_h have to be calculated. Their value have been numerically evaluated on the Gauss points of each element using the value of the relative humidity h^t at the current time t. Thus, the following expression for the moisture capacity has been used

$$\left(\frac{\partial W}{\partial h}\right)^t = \frac{Ck^tV_m^t + W^tk^t[1+(C-1)k^th^t] - W^tk^t(1-k^th^t)(C-1)}{(1-k^th^t)[1+(C-1)k^th^t]} \tag{4.8}$$

where

$$\begin{aligned} W^t &= W(h^t) \\ k^t &= k(n(w/c, t_e(t,h^t)), C) \\ V_m^t &= V_w(w/c, t_e(t,h^t)) \end{aligned} \tag{4.9}$$

Similarly, the expression for the moisture diffusion coefficient reads as

$$D_h^t = D_{h,ref}F_1(h^t)F_2(T)F_3(t_e(t,h^t))F_4(\xi(\varphi^t)) \tag{4.10}$$

4.1.3 Carbon dioxide diffusion-reaction

Following a similar solution procedure to the one described for the relative humidity equation, the diffusion-reaction process of the carbon dioxide is studied. The carbonation process is described via the numerical implementation of eqs. 2.19-2.20-2.21. The time dependent partial differential equations, describing the evolution in time of the various concentration are discretized using a fully implicit finite element scheme. Again, a central difference scheme has been adopted for the time variable. Starting from the concentration of the carbon dioxide $[CO_2]^t$ at time t, the diffusion-reaction equation used to define the evolution of the carbon dioxide concentration $[CO_2]^{t+1}$ for the incremental time step $t+1$, reads as

$$\begin{aligned} \frac{\xi(\varphi^t)(1-f)\left[[CO_2]^{t+1} - [CO_2]^t\right]}{\Delta t} &= \nabla\cdot(D_{CO_2}(\xi(\varphi^t), h^{t+1}, \alpha^t)\nabla[CO_2]^{t+1}) \\ &\quad - \xi(\varphi^t)f_w^t r_n^t \quad in\ \Omega_c \end{aligned} \tag{4.11}$$

where the porosity value $\xi(\varphi^t)$ and the the damage profile α^t are evaluated over the Gauss points of each elements at the current time t. For the relative humidity the value h^{t+1} obtained from the solution of the moisture transport equation 4.6 is considered. The value of the diffusion coefficient is evaluated as follows

$$\begin{aligned} D_{CO_2}(\xi(\varphi^t), h^{t+1}, \alpha^t) &= A(\xi(\varphi^t))B(h^{t+1})C(\alpha^t) \\ &= \xi(\varphi^t)^{1.8}(1-h^{t+1})^{2.2}\left[1.42\cdot 10^{-6}(1-\alpha^t)^m + 10^5(\alpha^t)^m\right] \end{aligned} \tag{4.12}$$

The values for the reaction coefficients f_w^t and r_n^t at the current time t are calculated using the current value of the carbon dioxide concentration $[CO_2]^t$ and the updated moisture profile h^{t+1} obtained from the solution of eq. 4.6.

$$\begin{aligned} f_w^t &= f_w(h^{t+1}) \\ r_n^t &= HRTk_2\left[OH^-\right]_{eq}[CO_2(g)]^t\left[Ca(OH)_2(aq)\right]^t \end{aligned} \tag{4.13}$$

Once the concentration for the carbon dioxide $[CO_2]^{t+1}$ at the new time increment $t+1$ has been obtained, the evolution for the calcium hydroxide and the calcium carbonate concentration can be calculated as

$$\frac{[Ca(OH)_2]^{t+1} - [Ca(OH)_2]^t}{\Delta t} = -\xi(\varphi^t) f_w(h^{t+1}) r_n([CO_2]^{t+1}) \qquad in\ \Omega_c \tag{4.14}$$

$$\frac{[CaCO_3]^{t+1} - [CaCO_3]^t}{\Delta t} = \xi(\varphi^t) f_w(h^{t+1}) r_n([CO_2]^{t+1}) \qquad in\ \Omega_c \tag{4.15}$$

Lastly, from the calcium hydroxide concentration $[Ca(OH)_2]^{t+1}$ at time $t+1$, the updated values for the carbonation profile φ^{t+1} and the pH^{t+1} values are evaluated following

$$\varphi^{t+1} = 1 - \frac{[Ca(OH)_2]^{t+1}}{[Ca(OH)_2]^0} \qquad in\ \Omega_c \tag{4.16}$$

$$pH^{t+1} = 14 + \log(2 \cdot 10^3 [Ca(OH)_2]^{t+1}) \qquad in\ \Omega_c \tag{4.17}$$

4.1.4 Corrosion of steel rebar

Once the updated value of the pH profile is calculated, it is possible to evaluate the occurrence of corrosion over the steel rebar. To do so, the pH profile within the concrete surrounding the steel rebar is checked over their Gauss points and if its value is below 9, the adjacent elements inside the steel reabar are flagged and the corrosion process begins.

First, following the electrochemical kinetics equations presented in sec. 2.4 the corrosion current density is evaluated over the flagged steel rebar elements outer surface Γ_s as shown in fig. 4.2(a). The corrosion potential is calculated from eq. 2.58 as follows

$$E_{corr}^{t+1} = \frac{1}{b_a + b_c}\left[\frac{b_a \cdot b_c}{2.3} \ln\left(\frac{i_{0,O2}}{i_{0,Fe}} \frac{[O_2]_r^t}{[O_2]_b}\right) + b_c E_{0,Fe} + b_a E_{0,O2}\right] \tag{4.18}$$

where $[O_2]^t$ is the concentration of the oxygen evaluated at the surface of the flagged steel elements at the current time t. From the value of the corrosion potential E_{corr}^{t+1}, considering the relationship from eq. 2.57, the value for the corrosion current density is evaluated as

$$i_c^{t+1} = i_{corr}^{t+1} = i_{0,O2} \frac{[O_2]_r^t}{[O_2]_b} \texttt{exp}\left(2.3 \frac{E_{0,O2} - E_{corr}^{t+1}}{b_c}\right) \tag{4.19}$$

Once the corrosion current density is obtained, the flagged elements are converted into rust, thus changing the corresponding domain from $\Omega_s \rightarrow \Omega_r$. This change also modifies the element mechanical and porosity properties from steel to rust. Rust mechanical properties have been taken from [164]. The porosity properties of rust with respect to water and oxygen diffusion have been considered equal to the properties of carbonated concrete following [10]. Fig. 4.2(b) shows an example of steel to rust elements change after the evaluation of the corrosion current density.

Once rust elements are present in the domain, the steel surface Γ_s can be adjacent to concrete or rust elements. If the interface is between steel and concrete the procedure presented above is employed. Otherwise, if the steel element is adjacent to a rust element, the condition for the metal corrosion is given by the presence of oxygen and water over its surface. To account for this, moisture transport and oxygen diffusion through the rust layer

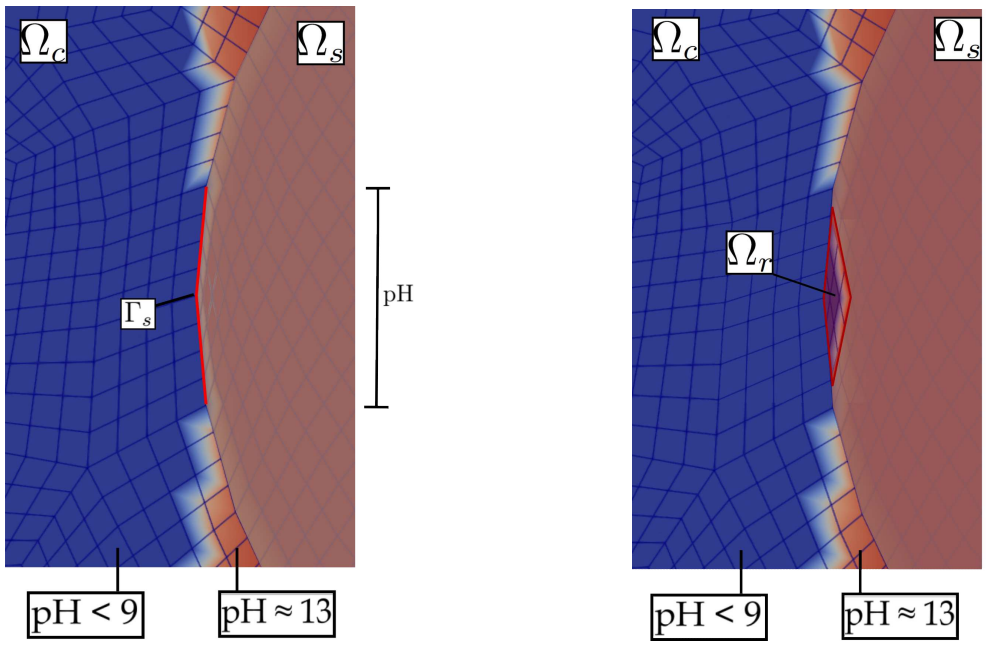

Figure 4.2: Discretization of the corrosion process over the steel rebar: a) portion of the steel rebar surface affected by the corrosion process due to the drop in the pH value of the concrete pore water; b) example of steel to rust elements change following the corrosion process.

become an important process to consider as corrosion changes from a concentration controlled to diffusion controlled. In particular, presence of moisture at the rebar surface is considered as the trigger condition for corrosion to start over the new steel elements while the oxygen concentration becomes the limiting factor for the corrosion rate. The two corrosion trigger mechanisms for different portion of the rebar surface are reported in Fig. 4.3, where for the red portion of Γ_s the value of the pH determines the corrosion initiation while for the green portion corrosion initiation is determined by presence of moisture and oxygen.

Once the value of the corrosion current density i_{corr}^{t+1} is determined, it is possible to calculate the oxygen consumption associated to the cathodic process

$$J_{O_2}^{t+1} = \frac{i_{corr}^{t+1}}{z_{O_2} F} \tag{4.20}$$

as well as the values for the radius expansion Δr and its associated inelastic deformation $\boldsymbol{\varepsilon}_0$ as follows

$$\Delta_r^{t+1} = \Delta r^t + \frac{i_{corr}^{t+1} P A_{Fe}}{z_{Fe} F \rho_{Fe}} \left(\frac{\gamma}{\beta} - 1 \right) \Delta t \tag{4.21}$$

$$\boldsymbol{\varepsilon}_0^{t+1} = \frac{\Delta r^{t+1}}{r_0} \mathbb{I} \tag{4.22}$$

The radius expansion at each time increment is added to its previous value as the time increment Δt is considered on eq. 4.21.

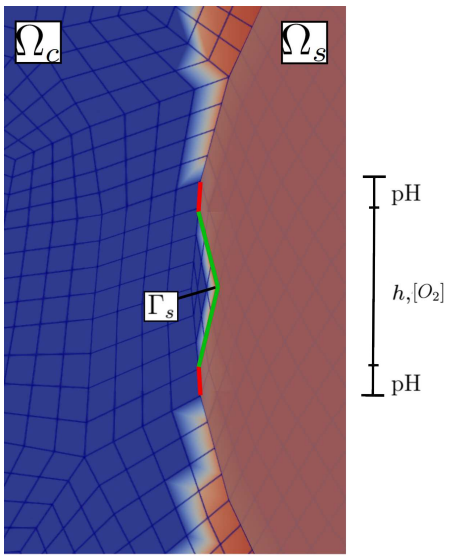

Figure 4.3: Steel surface evolution during the corrosion process.

4.1.5 Oxygen diffusion

The diffusion process of oxygen has been modelled following eq. 2.63 with the appropriate boundary conditions expressed in eq. 2.66. The numerical discretization for the diffusion equation follows a process similar to eqs. 4.6 and 4.11. Therefore, using a central difference scheme for the time variable with a fully implicit finite element scheme, the equation providing the value for the oxygen concentration $[O_2]^{t+1}$ at the time increment $t+1$ is given as follows

$$\begin{aligned} \frac{\xi(\varphi)\,(1-f)\,[[O_2]^{t+1}-[O_2]^t]}{\Delta t} &= \nabla\cdot\left(D^t_{O_2}(\xi(\varphi^{t+1}),h^{t+1},\alpha^t)\nabla\left[O_2^{t+1}\right]\right)+ \\ &\quad - J^{t+1}_{O_2} \qquad in\ \Omega_c\cup\Omega_r \end{aligned} \tag{4.23}$$

Here, the value of the diffusion coefficient is evaluated over the Gauss points of each concrete and rust element using the updated values at the incremental time $t+1$ for the porosity of the concrete $\xi(\varphi)^{t+1}$ and for the relative humidity h^t while for the damage profile the value at the current time α^t is used.

4.1.6 Rupture of the concrete cover

The last step of the algorithm consists in the evaluation of the formation of cracks in the concrete cover due to accumulation of rust over the steel surface. The mechanical problem is studied using the phase field approach to brittle fracture. The modified functional Π_{rc}, accounting for the fracture tension-compression anisotropy split is used. The minimization problem used to evaluate the evolution of the crack set reads as

$$(\mathbf{u}^{t+1},\alpha^{t+1}) = \mathrm{Arg}\left\{\min\left\{\Pi_{rc}(\boldsymbol{\varepsilon},\alpha)\right\}\right\}\ \ subjected\ to\ \ \dot{\alpha}\geq 0,\ \ \alpha\in[0,1] \tag{4.24}$$

The mechanical problem also accounts for the change of the concrete material properties. These changes are considered for the concrete fourth order elasticity tensor $\mathbb{C}^{t+1}$, for the

fracture toughness Gc^{t+1} and for the internal length parameter $\ell(\varphi^{t+1})$ starting from the updated value of the carbonation profile φ^{t+1} given by eq. 4.16

Recalling [187], the minimization of functional (4.24) is numerically challenging because:

1. the dependency of the positive part of the elastic energy of concrete on the damage field renders the energetic functional non-convex thus causing the minimization problem to admit many local minimizers;

2. accounting for damage irreversibility introduces bounded constraints on the damage variable α which necessitate the solution of variational inequalities;

3. damage localization appears in thin bands on the order of ℓ which is noticeably small compared to the whole domain. However, in order to describe correctly the transition zone between broken and unbroken material, sufficiently small cell size has to be adopted, leading to very large problem size.

Solutions to the quasi-static evolution at discrete time steps are obtained from a global energy minimum principle on both variables with an additional irreversibility constraint for the damage variable.

A robust solution strategy can be achieved via a weakly coupling of the equations using an alternate minimization staggered algorithm. This method consists in the separate iterative solution of two sub-problems until convergence is achieved: the displacement problem is solved at a fixed phase-field, and the damage problem is solved at a fixed displacements values [188].

The algorithm bases on the fact that the functional is convex separately in u and α if the other variable is kept constant. Solution $(\mathbf{u}^{t+1}, \alpha^{t+1})$ at load increment $t+1$ is obtained in an iterative procedure

$$\begin{aligned} \mathbf{u}^{t+1} &= \mathrm{Arg}\left\{\min\left\{\Pi_{rc}(\boldsymbol{\varepsilon}, \alpha^t)\right\}\right\} && u-\text{problem} \\ \alpha^{t+1} &= \mathrm{Arg}\left\{\min\left\{\Pi_{rc}(\boldsymbol{\varepsilon}^{t+1}, \alpha)\right\}\right\} && \alpha-\text{problem} \end{aligned} \tag{4.25}$$

until convergence. The staggered algorithm is summarized in Algorithm 1. Convergence is reached when the change of the damage field in the iteration is below a certain tolerance. Alternative stopping criterion can be adopted [189].

Algorithm 1 *Alternate minimization*

Determination of a stationary point of (4.24)
Given $(\mathbf{u}^t, \alpha^t)$, the state at the current loading step t. Set $(\mathbf{u}_0, \alpha_0) = (\mathbf{u}^t, \alpha^t)$
while *not converged*
    $i = i + 1$
    Find $\mathbf{u}_i$: $\mathrm{Arg}\left\{\min\left\{\Pi_{rc}(\boldsymbol{\varepsilon}, \alpha_{i-1})\right\}\right\}$
    Find α_i : $\mathrm{Arg}\left\{\min\left\{\Pi_{rc}(\boldsymbol{\varepsilon}_i, \alpha)\right\}\right\}$
Set $(\mathbf{u}^{t+1}, \alpha^{t+1}) = (\mathbf{u}_i, \alpha_i)$

Lastly, the irreversibility condition can be introduced in the formulation using different methods:

- introducing a history variable which tracks and store through time of the maximum crack driving force at each point of the domain [188];

- via the addition of a penalization term which penalize healing of the material and the evolution of the damage field if it exceed the upper bound $\alpha = 1$ [190];

- numerically introduced in the damage sub-problem solver [191].

Here, the condition is introduced via the addition of a lower bound α_{lb} to the damage field and numerically enforced in the solver. To do so, the PETSc SNES [192] package has been used where the SNESVINEWTONRSLS method (reduced space active set solvers for variational inequalities based on Newton's method) permits to solve variational inequalities by setting a lower and an upper bound. The upper bound is set equal to $\alpha = 1$ while the lower bound is updated at the end of each time step by setting $\alpha_{lb} = \alpha^{t+1}$.

4.1.7 The complete process

The complete process describing the algorithm developed to investigate the carbonation corrosion induced degradation phenomena is summarized in fig. 4.4. For a given time t, the flowchart reports the full procedure adopted in the numerical model to solve equation presented previously for the time increment $t + 1$.

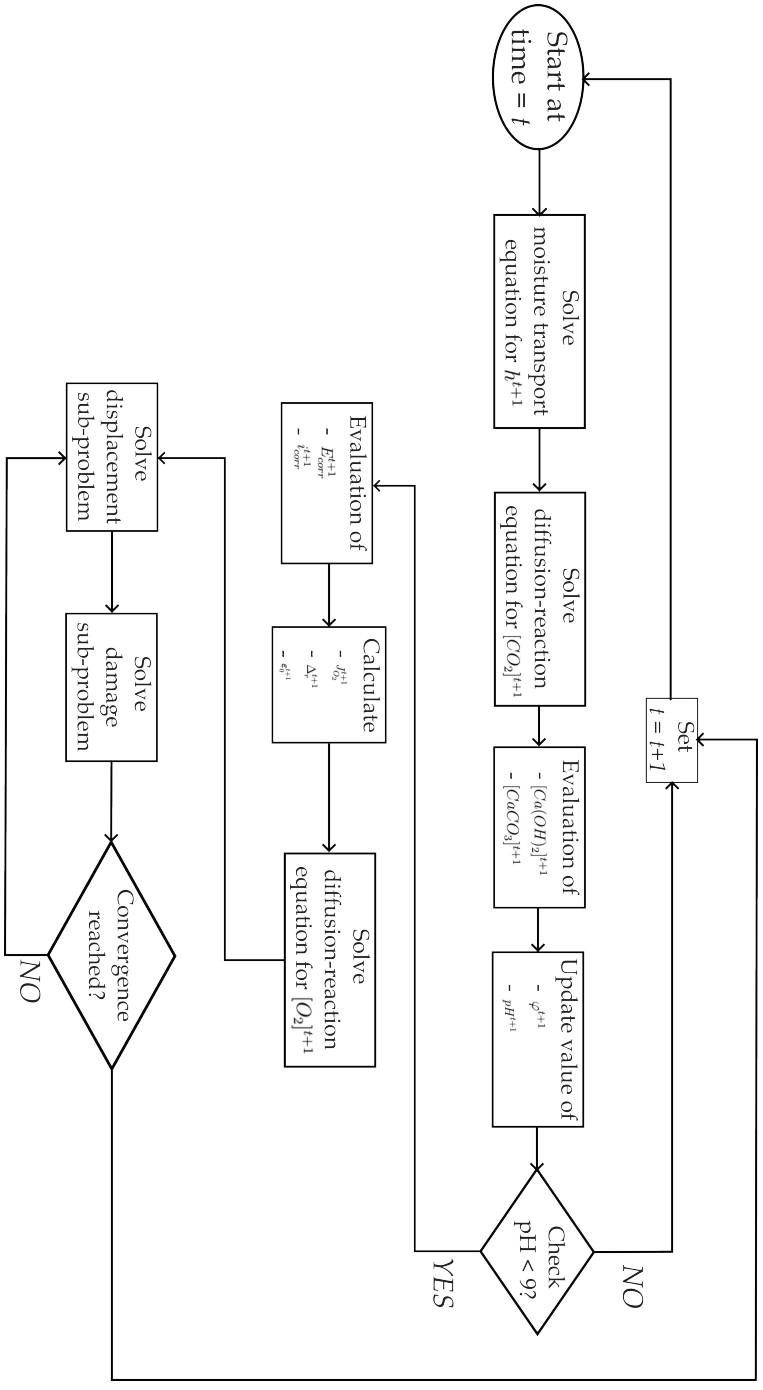

Figure 4.4: Flowchart of the predictive model for carbonation corrosion phenomena in reinforced concrete elements.

Chapter 5

Numerical results

The developed model is now applied to the analysis of reinforced concrete elements affected by carbonation corrosion phenomena. Initially, each process is analysed and the results are compared to experimental and numerical values obtained from the literature. Eventually, two representative examples are investigated. For the first test, a corner rebar from a reinforced concrete element is analysed. A square domain with a single centred steel rebar is considered in which carbon dioxide, moisture and oxygen enter from two adjacent sides. In the second test, a square domain with four reabars placed near each corner of the section is considered. Similarly to the corner rebar test, two sides of the specimen are exposed to the outer environment from which carbon dioxide, moisture and oxygen can enter the concrete cover.

5.1 Model validation

First, comparisons between the results obtained from the numerical simulation of each process and experimental and/or numerical results obtained from the literature are performed to validate the capacity of the proposed model to reproduce correctly the various physical processes.

5.1.1 Carbonation process

The results obtained from the numerical model developed for the carbonation process are now compared against numerical and experimental values obtained from the literature. Both the experimental results from the accelerated carbonation test presented in [8] as well as for the natural carbonation process presented in [41] are compared with the results obtained from the developed model.

Accelerated carbonation test

Following [8], a rectangular domain of L = 300 mm and H = 100 mm of OPC concrete with $w/c = 0.5$ ratio is considered. The test is performed at a constant room temperature of 30°C, constant environmental relative humidity of $\overline{h}_{en} = 65\%$ and external concentration of carbon dioxide equal to $\overline{[CO_2]} = 50\%$ of the air content. The carbon dioxide enters the specimen from the left and right sides while top and bottom boundaries are coated in epoxy resins such that a monodimensional diffusion of CO_2 within the specimen is observed. The

test setup is reported in fig. 5.2(a). During the simulations only half of the domain has been discretized due to the symmetry of the test setup. A mesh of L = 150 mm and H = 100 mm made of 15000 quadrilateral elements has been considered. The total time for the simulation has been set equal to T_{tot} = 25 days, divided into equally-sized time steps Δt = 1 hour. The carbonation front advancement at each day obtained from the numerical model is reported in fig. 5.1(b) while the values corresponding to the maximum depth for which $\varphi = 1$ is observed are reported in table 5.1. The results obtained from the numerical simulation are in good agreement with both the experimental as well as the numerical reference values.

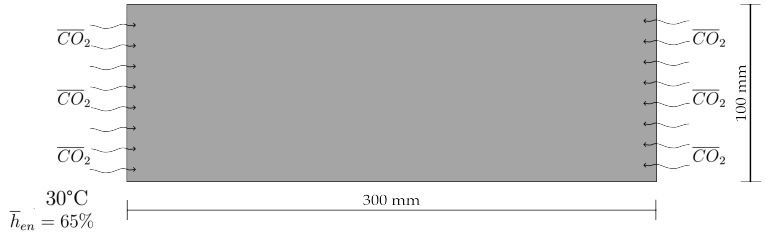

a)

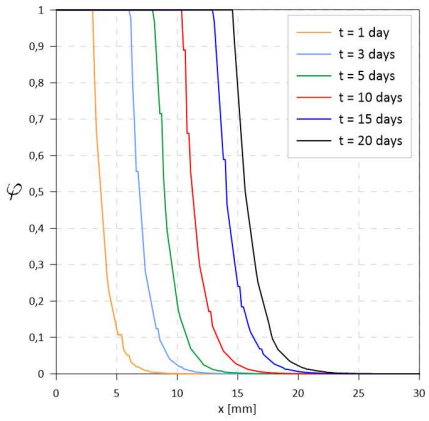

b)

Figure 5.1: Accelerated carbonation test: a) test setup; b) carbonation front plots at t = 1, 3, 5, 10, 15, 20 days.

Day	Experimental results [mm] [8]	Numerical results [mm] [8]		Numerical results [mm]	
1	3	3.5	(16.66%)	3	(∼)
3	5	5.5	(10%)	6	(20%)
5	8	7	(12.5%)	7.9	(1.25%)
10	10	8.9	(11%)	10.5	(5%)
15	12	11.5	(4.16%)	12.7	(5.83%)
20	15	14	(6.66%)	15	(∼)

Table 5.1: Results comparison for the carbonation process. Values in parentheses correspond to the relative error with respect to the experimental results.

Natural carbonation test

The natural carbonation process is now investigated. In [41] are reported the results for the carbonation depth of concrete under natural carbonation after 2 years of testing at room temperature of 22±2 °C and constant environmental relative humidity of $\overline{h}_{en}$ = 55±5 %. Two cylindrical specimen of base diameter of 75 mm and heigh of 150 mm of standard OPC concrete with water/cement ratio of 0.69 (specimen A) and 0.49 (specimen B) are used for the testing. After two years the carbonation depths reported in [41] read as 7 mm (4.95 mm/year$^{0.5}$) for the specimen A and 5 mm (3.54 mm/year$^{0.5}$) for the specimen B.

Numerical simulations have been performed to test the results obtained from the model with the experimental results from the literature. During the simulations a rectangular domain of dimension 150 x 75 mm has been considered. The outer concentration of the carbon dioxide has been set as $\overline{[CO_2]} = 0.03\%$ of the air content, temperature equal to 22 °C and environmental relative humidity of $\overline{h}_{en} = 55\%$. Fig. 5.2(a) reports the test setup used for the numerical simulations. First the simulation considering a concrete with w/c = 0.69 (specimen A) followed by the same setup but with the value of the water/concrete ratio set as w/c = 0.49 (specimen B).

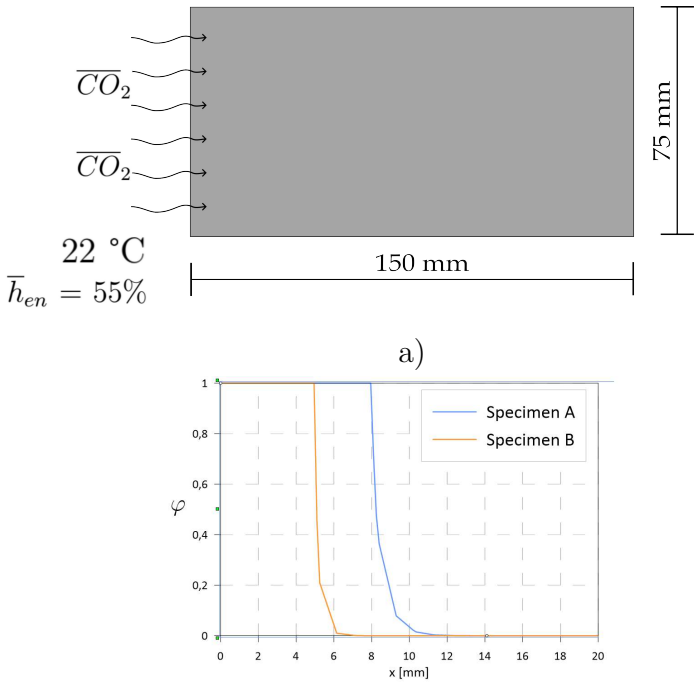

Figure 5.2: Natural carbonation test: a) test setup; b) carbonation front plots at T = 2 years.

The domain has been discretized using 11250 quadrilateral elements while the simulated time was $T_{tot} = 2$ years, divided into equally spaced intervals of $\Delta t = 1$ day. The carbonation profiles at the end of the simulations are reported in fig. 5.2(b). The depth of the carbonation fornt has been taken as the maximum depth where $\varphi = 1$. The simulations results are reported in table 5.2 showing good agreement with the experimental results.

Specimen	Experimental result [mm] [41]	Numerical result [mm]
A	7	7.9
B	5	4.95

Table 5.2: Results comparison for the natural carbonation process after 2 years.

5.1.2 Moisture transport in concrete

Moisture content variation within concrete due to changes in the external humidity are analysed via the comparison with experimental results from the literature. Experimental results for the moisture transport in concrete are presented in [193]. A specimen of OPC concrete 100 x 150 x 300 mm with w/c = 0.5 cured at 23°C and 100% RH is considered. After curing, lateral surfaces were sealed with epoxy such that a monodimensional moisture flow through the specimen is observed. Eventually, the specimen was placed in a chamber at controlled temperature of 23 °C while relative humidity was set to three different values: $\overline{h}_{en} = 20\%$ for 30 days, $\overline{h}_{en} = 5\%$ for 10 days an lastly to $\overline{h}_{en} = 70\%$ for 30 days. The test setup is reported in fig. 5.3(a). For the numerical simulation a rectangular domain of L = 100 mm and H = 150 has been considered which has been discretized using a mesh of 240000 quadrilateral elements. The initial concentration for the concrete has been set to $h_0 = 100\%$. External temperature is set to 23 °C while the external relative humidity is set as

$$\begin{cases} \overline{h}_{en} = 20\% & if\ t < 30\ days \\ \overline{h}_{en} = 5\% & if\ 30 \leq t < 40\ days \\ \overline{h}_{en} = 70\% & if\ t \geq 40\ days \end{cases} \tag{5.1}$$

The simulated time is equal to $T_{tot} = 70$ days and has been divided into smaller equally-sized time increments of $\Delta t = 1$ hour. The value of the relative humidity over time at a depth of x = 8 mm are reported in fig. 5.3(b). Starting from its initial value of $h = 100\%$, the moisture content sharply decrease as the specimen release humidity in the outer environment. A reduction in the rate of dessication is observed approximately at week ten up to week thirty, when the outer environmental moisture content changes to 5%. Here, the dessication rate slightly increase and the moisture content of the specimen reaches a value of approximately 50%. After week forty, when the value of $\overline{h}_{en}$ increases to 70%, the moisture content within the specimen slowly increase until an almost equilibrium condition between the specimen and the environment moisture content is reached at the end of the simulation. The profile obtained from the numerical test show good agreement with the experimental results reported in [193].

5.1.3 Corrosion current density

The corrosion process of the steel rebar is now analysed. Results of the corrosion current density are compared with the experimental values from [194]. The test setup consists of a 100 mm cube specimen of standard OPC concrete with a water/cement ratio of 0.55 containing a central steel rebar. The specimen is initially subjected to accelerated carbonation with a 4% CO_2 content at 20 °C and $\overline{h}_{en} = 55\%$ relative humidity and eventually transferred to a

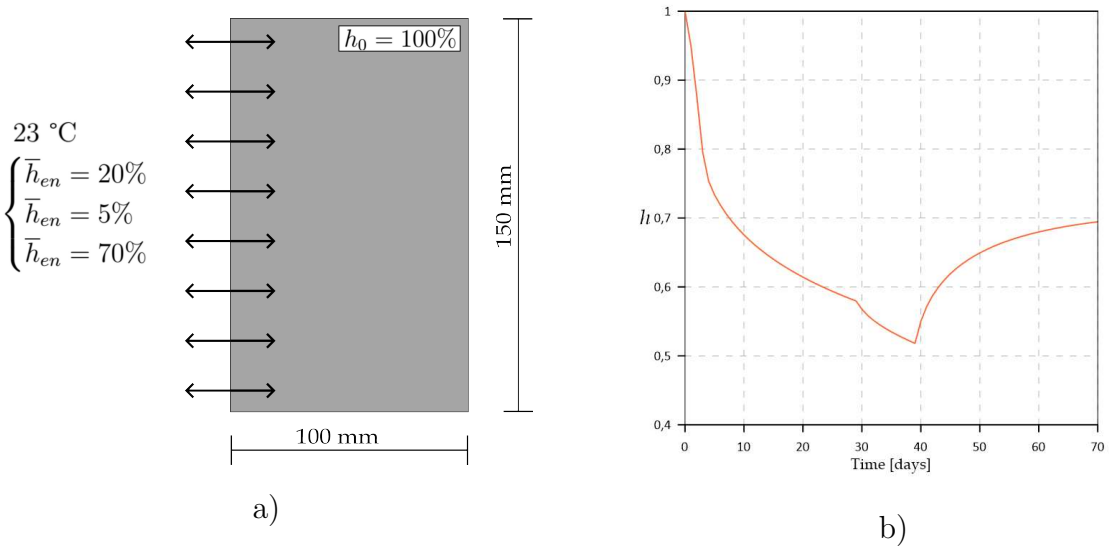

Figure 5.3: Moisture transport test: a) moisture transport setup; b) moisture content over time at x = 8 mm from the external face.

high humidity chamber ($\overline{h}_{en} = 95\%$) to induce corrosion of the reinforcement bars and the current density value is recorded over a time period of 24 weeks.

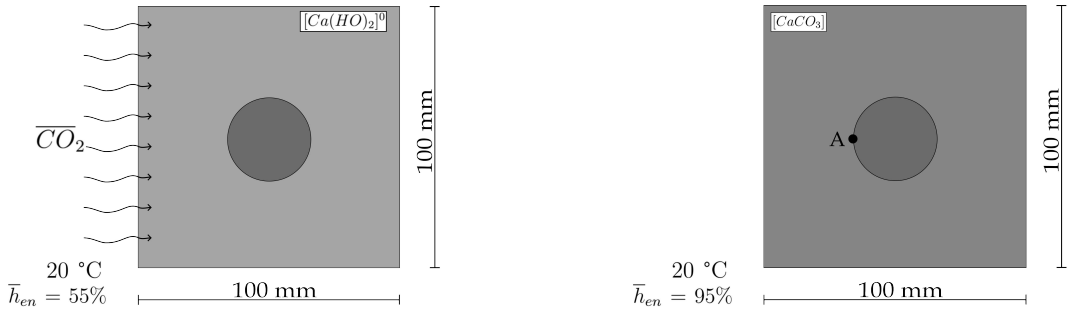

Figure 5.4: Corrosion test: a) advanced carbonation setup; b) corrosion test. Point A represent the location from which the corrosion current density values are taken.

The numerical simulation has been performed over a square mesh of 35904 quadrilateral elements. Initially, the advanced carbonation process of concrete is performed considering a $\overline{[CO_2]} = 4\%$ carbon dioxide external concentration, room temperature of 20 °C and external relative humidity $\overline{h}_{en} = 55\%$. Once the carbonation profile reaches the rebar, the environmental relative humidity is set to $\overline{h}_{en} = 95\%$. The parameters used to model the corrosion process are reported in table 5.3. The simulated time is equal to $T_{tot} = 24$ weeks which start after the carbonation process of the concrete has ended. Equally-sized time steps of $\Delta t = 1$ day are considered.

Property	Value	
Anode equilibrium potential ($E_{0,Fe}$)	-0.682	[V]
Anode equilibrium current density ($i_{0,Fe}$)	$1{\cdot}10^{-3}$	[A/m^2]
Anode tafel slope (b_a)	0.340	[V/dec.]
Cathode equilibrium potential ($E_{0,O2}$)	0.350	[V]
Cathode equilibrium current density ($i_{0,O2}$)	$1{\cdot}10^{-4}$	[A/m^2]
Cathode tafel slope (b_c)	0.350	[V/dec.]

Table 5.3: Corrosion parameters [18]

The results from [194] reports corrosion values for the steel rebar before and after the dissolution of the passive layer due to the carbonation process defining a passive and an active corrosion rate. The experimental results report a passive corrosion current density equal to 0.0002 A/m^2 and an active corrosion current density of 0.00823 A/m^2. The numerical values for the corrosion current density have been taken on point A of the rebar as shown in fig. 5.4 and are in good agreement with the experimental results as an initial passive corrosion current density equal to 0.00095 A/m^2 is observed, reaching an active corrosion current density of 0.00893 A/m^2 after the dissolution of the protective passive layer.

5.2 Numerical test: Corner rebar

Now a representative example is analysed in which the degradation process of a corner rebar in a reinforced concrete element is simulated. Carbon dioxide, moisture and oxygen enter the material from the left and bottom side while the top and right side are connected with the other portion of the element. This first simple test aims to investigate the capability of the developed model to investigate the complete carbonation corrosion phenomena on a reinforce concrete element. The interactions between the different processes will be discussed, highlighting the critical aspects and conditions which emphasize the effects of the degradation mechanism.

5.2.1 Test setup

A squared sample of standard OPC concrete with w/c = 0.5 of dimension L, H = 76 mm containing a central rebar of diameter 16 mm is considered. A constant temperature value of 25°C is used throughout the simulations. The physical domain is discretized using a mesh of 35904 quadrilateral elements with an average cell size of 0.2 mm. The material properties from table 5.4 for concrete, steel and rust are considered.

The initial conditions for the carbon dioxide diffusion-reaction process, the moisture transfer and the oxygen diffusion processes are the following

Material property	Value	
Concrete elastic modulus (E_c)	31500	[MPa]
Concrete Poisson modulus (ν_c)	0.2	
Carbonated concrete elastic modulus (E_{CaCO_3}) [71]	35000	[MPa]
Carbonated concrete Poisson modulus (ν_{CaCO_3}) [71]	0.2	
Concrete porosity (ξ_c) [195]	0.16	
Carbonated concrete porosity (ξ_{CaCO_3}) [54]	0.11	
Steel elastic modulus (E_s)	210000	[MPa]
Steel Poisson modulus (ν_s)	0.3	
Rust elastic modulus (E_r) [164]	132000	[MPa]
Rust Poisson modulus (ν_r) [164]	0.25	
Concrete internal length parameter (ℓ_c) [71]	5	[mm]
Concrete release energy rate (Gc_c) [196]	$75{\cdot}10^{-3}$	$[\frac{N}{mm}]$
Carbonated concrete internal length parameter (ℓ_{CaCO_3}) [71]	4	[mm]
Carbonated concrete release energy rate (Gc_{CaCO_3}) [196]	$75{\cdot}10^{-3}$	$[\frac{N}{mm}]$

Table 5.4: Material parameters

$$\begin{aligned} [CO_2](\Omega_c, 0) &= 0 && \left[\frac{mol}{mm^3}\right] \\ [Ca(OH)_2](\Omega_c, 0) &= 1.2 \cdot 10^{-4} && \left[\frac{mol}{mm^3}\right] \\ [CaCO_3](\Omega_c, 0) &= 0 && \left[\frac{mol}{mm^3}\right] \\ h(\Omega_c, 0) &= 60\% \\ [O_2](\Omega_c, 0) &= 9.4 \cdot 10^{-9} && \left[\frac{mol}{mm^3}\right] \end{aligned} \tag{5.2}$$

The Neumann boundary condition for the moisture transport reads as

$$J_h(\Gamma_c, t) = 2.099(\overline{h}_{en} - h) \tag{5.3}$$

with $\overline{h}_{en}$ given as the average value of the environmental moisture content for each month registered in the city of Parma given in table 2.1. The Dirichlet boundary conditions for the carbon dioxide and for the oxygen concentration are

$$\begin{aligned} [CO_2](\Gamma_c, t) &= 416 \cdot 10^{-6} && \left[\frac{mol}{mm^3}\right] \\ [O_2](\Gamma_c, t) &= 9.4 \cdot 10^{-9} && \left[\frac{mol}{mm^3}\right] \end{aligned} \tag{5.4}$$

The parameters used for the corrosion process are reported in table 5.3. Lastly, the following boundary conditions for the mechanical problem are introduced. Vertical displacements are blocked on the top side while the horizontal displacements are blocked in the right side of the domain:

$$\begin{aligned} \mathbf{u}_y(\Gamma_{u,t}, t) &= 0 \\ \mathbf{u}_x(\Gamma_{u,r}, t) &= 0 \end{aligned} \tag{5.5}$$

A constant time interval $\Delta t = 1$ day has been considered throughout the simulation. The analysis has been stopped once spalling of the concrete cover is observed. The specimen geometry and boundary conditions are reported in fig. 5.5

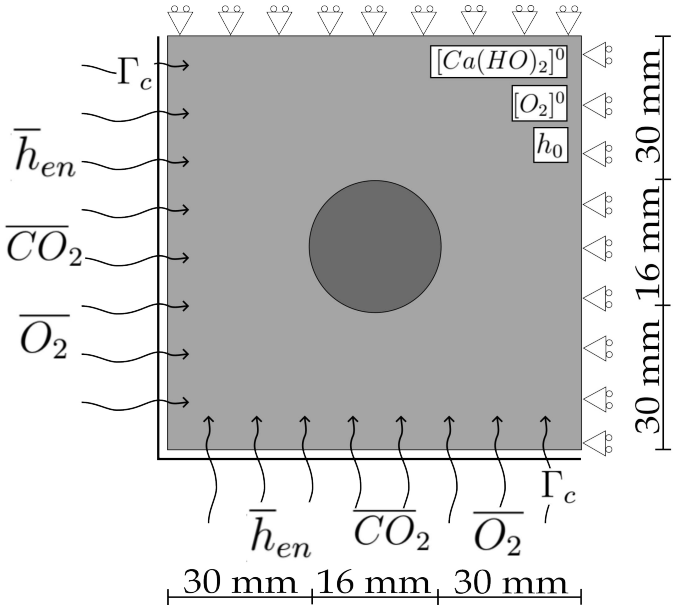

Figure 5.5: Test setup for the corner rebar test.

5.2.2 Numerical results

The results obtained from the numerical simulation for the corner rebar test are reported in figs. 5.6, 5.7, 5.8, 5.9 and 5.10. Each figure reports the results at significant time of the degradation mechanism, namely:

- start of the corrosion process;
- first crack around the rebar;
- crack propagation to the bottom boundary;
- spalling of the left portion of the cover;
- complete spalling of the cover.

The results for the start of the corrosion process are reported in fig. 5.6. Time of the simulation correspond to t = 2885 days ($\sim$ 8 years). Fig 5.6(a) reports the carbon dioxide field within the concrete cover while fig. 5.6(b) shows the carbonation front. The value of the carbonation rate is in good agreement with the experimental values for natural carbonation reported in [41] with an average advancement of approximately 3.73 mm/year. The concrete carbonation process interest the outer portion of the cover and reaches the

bottom left quarter of the rebar accordingly to the initial conditions of the carbon dioxide which enters the concrete from the bottom and left side of the specimen. As visible from fig. 5.6(d), which reports a zoom of the elements in the rust and steel domains, the passive layer of the outer elements corresponding to the direction from which the carbonation profile reaches the central rebar has been dissolved, leading to the formation of rust elements. Fig. 5.6(c) reports the relative humidity. The moisture content of the specimen has increased during the previous months to an average value of 70% inside the concrete pores. As the outer value of the relative humidity is lower, dessication of moisture from the specimen is observed.

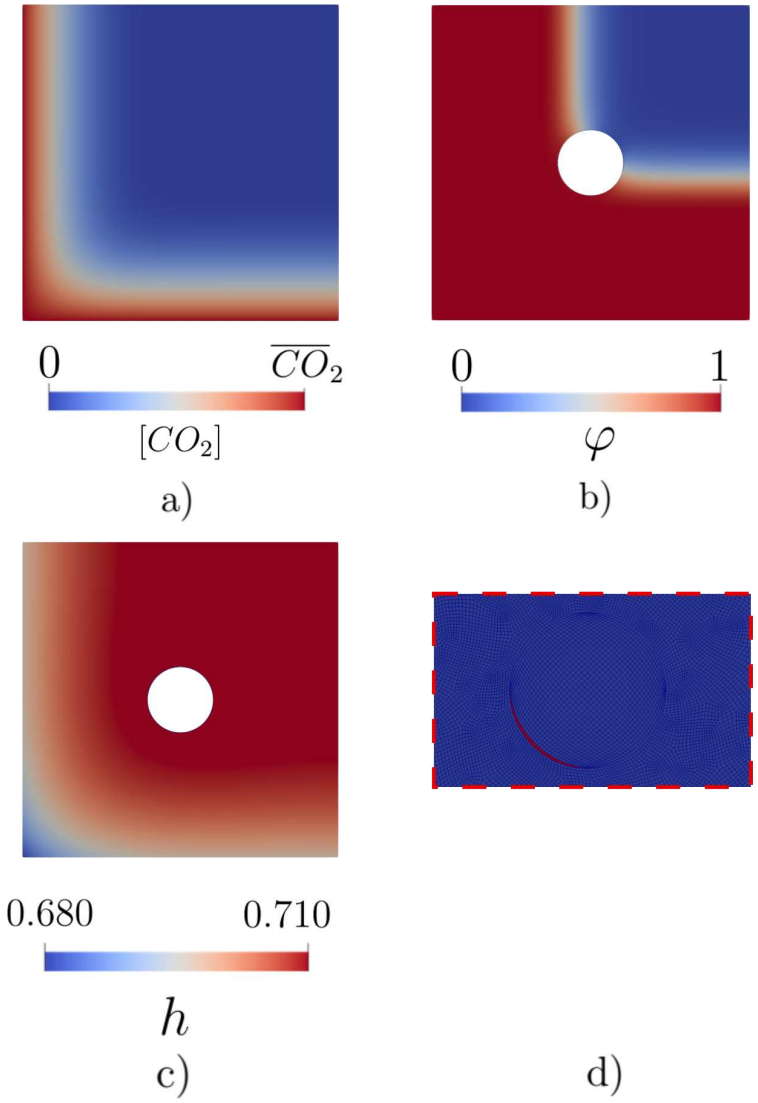

Figure 5.6: Corner rebar test: results at the start of the corrosion process (t = 2885 days). a) Carbon dioxide concentration; b) Carbonation front; c) relative humidity; d) zoom on the elements marked as rust.

The next step reported consists in the crack initiation around the rebar due to the increase in volume of the rust layer (fig. 5.7). The simulated time correspond to t = 5342 days ($\sim$ 14.6 years). The carbon dioxide field is reported in fig. 5.7(a). Fig. 5.7(b) shows the carbonation profile and it can be noted that the carbonation process has slowed its penetration rate within

the concrete cover compared to 5.6(b). The lower rate is directly related to the reduction of the material porosity due to the carbonation process as well as to the longer distance to be covered by the diffusion of the carbon dioxide to reach non-crabonated areas of the specimen. Fig. 5.7(d) reports the rust elements within the rebar while 5.7(e) shows the portion of the steel surface affected by the corrosion current density. The maximum value for the corrosion current density reported at this time of the simulation is equal to $i_{corr} = 8.570 \cdot 10^{-3}$ [A/m^2] corresponding to an oxygen concentration at the rebar surface equal to $[O_2]_r = 8.74133 \cdot 10^{-9}$ [mol/mm^2], leading to a value of the ratio with the outer concentration of $[O_2]_r/[O_2]_b = 0.92$. The maximum value for the change in radius is equal to $\Delta_r = 0.1808$ mm. The damage profile is reported in fig. 5.7(f) showing the nucleation of cracks in the portion of concrete surrounding the corroded surface of the steel rebar.

Eventually, the first cracking phenomenon is observed at time t = 6598 days ($\sim$ 18 years). Here, the crack profile reported in fig. 5.8(f) shows that fracture affected the complete depth of the concrete cover as well as the bottom-left half of the concrete surrounding the steel rebar. The displacement field, highlighting the rupture of the concrete cover, is reported in fig. 5.8(g). The carbon dioxide profile from fig. 5.8(a) shows the free diffusive behaviour of the carbon dioxide within the cracks which permits an almost instantaneous introduction of the pollutant within the central section of the section. The carbonation profile, which now almost affects the entirety of the rebar, is reported in 5.8(b) while the moisture content is showed in 5.8(c). Figs. 5.8(d),(e) shows respectively the rust elements as well as the portion of the rebar surface affected by the corrosion process. Here the maximum value of the change in radius due to the rust formation is equal to $\Delta r = 0.2234$ mm while the corrosion current density reads as $i_{corr} = 9.02 \cdot 10^{-3}$ [A/m^2] with a ratio $[O_2]_r/[O_2]_b = 0.95$ and is registered in the last elements affected by the corrosion process since the initial oxygen supply in their proximity has not been significantly reduced during the cathodic corrosion semi-reaction.

The next representative step is reported in fig. 5.9 which corresponds to the spalling of the left portion of the concrete cover at t = 11940 days ($\sim$ 32.7 years). The damage field is reported in fig. 5.9(f). A single long crack is formed, starting from the bottom side and running through the specimen height to the top side of the section. A clear separation of the left portion of the concrete cover is observed in 5.9(g). Additionally, damage affects the entirety of the rebar since to corrosion interest the whole steel surface with rust deposits covering the entirety of the rebar as shown in figs. 5.9(d),(e). The maximum value for the change in radius is equal to $\Delta_r = 0.6042$ mm with a current density of $i_{corr} = 7.5 \cdot 10^{-3}$ [A/m^2]. It is possible to observe from the lower value of the corrosion current density that the corrosion process changed from concentration controlled to diffusion controlled. The corrosion rate is now governed by the capability of the oxygen to diffuse through the rust layer surrounding the steel rebar, causing the corrosion rate to reduce of approximately $\sim$20%. The carbonation front reported in fig. 5.9(b) highlights the negative effects tied to the intake of the carbon dioxide through cracks (fig. 5.9(a)). In fact, the carbonation process affected the inner portion of the specimen covering the entirety of the concrete surrounding the rebar thus causing the depassivation of the entire surface of the steel rebar.

Lastly, complete spalling of the concrete is reached at t = 18315 days ($\sim$ 50.2 years) leaving the rebar completely open to the outer environment effects. A thick rust layer corresponding to an increase of the rebar radius of $\Delta_r = 0.9764$ mm covers the entirety of the rebar, causing the formation of an additional crack branch starting from the rebar and reaching the right side of the specimen leading to the complete spalling of the concrete cover (fig. 5.10(f)). The displacement field reports the full separation of the concrete cover in fig.

5.10(g). As a result of the loss of the cover, the carbonation front reaches the internal section of the concrete elements (5.10(b)) due to the free access of the carbon dioxide.

The numerical simulation for the corner rebar test has been performed using an Intel i7-11800H. The total time required to perform a single run of the corner rebar test solving algorithm is equal to 24855 ms. The % of the total time required for each single portion of the solving algorithm are reported in Table 5.5. It is possible to observe that the most time consuming portion of the algorithm is occupied by the solution of the elasticity problem, due to displacement being vector field. The solution of the various scalar field problems requires a comparable portion of total time. The evaluation of the rebar corrosion process occupies the least amount of time as it is calculated using a for loop over the degrees of freedom of the cells within depassivated portion of steel rebar.

Section of the algorithm	% of the run time
Moisture transport	6.83%
CO_2 diffusion-reaction	3.46%
Rebar corrosion	1.07%
Displacement sub-problem iteration	80.68%
Damage sub-problem iteration	7.96%

Table 5.5: Average run time % for each section of the algorithm for the corner rebar test.

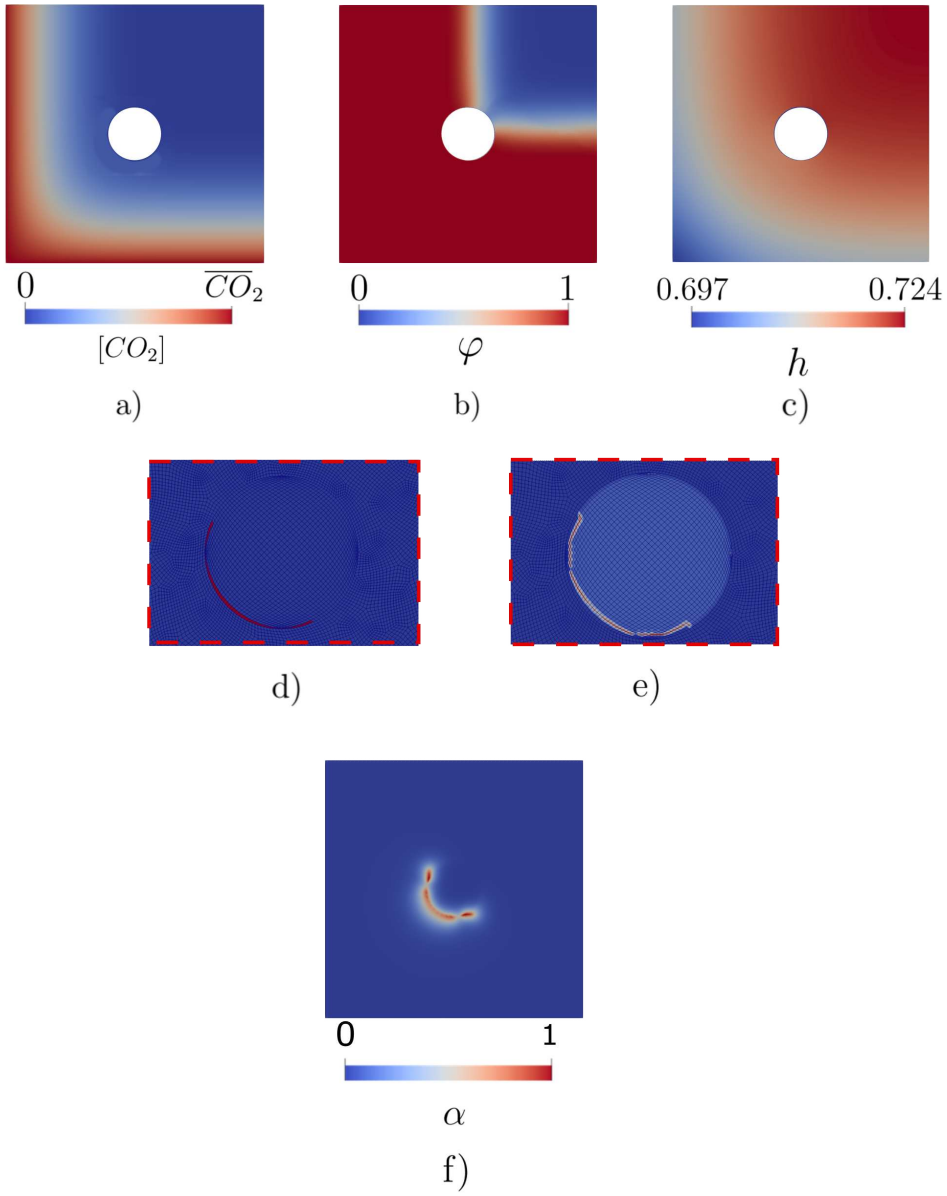

Figure 5.7: Corner rebar test: crack nucleation around the steel rebar (t = 5342 days). a) Carbon dioxide concentration; b) Carbonation front; c) relative humidity; d) zoom on the elements marked as rust; e) zoom on the steel rebar showing the portion of the steel surface under corrosion process; f) damage field.

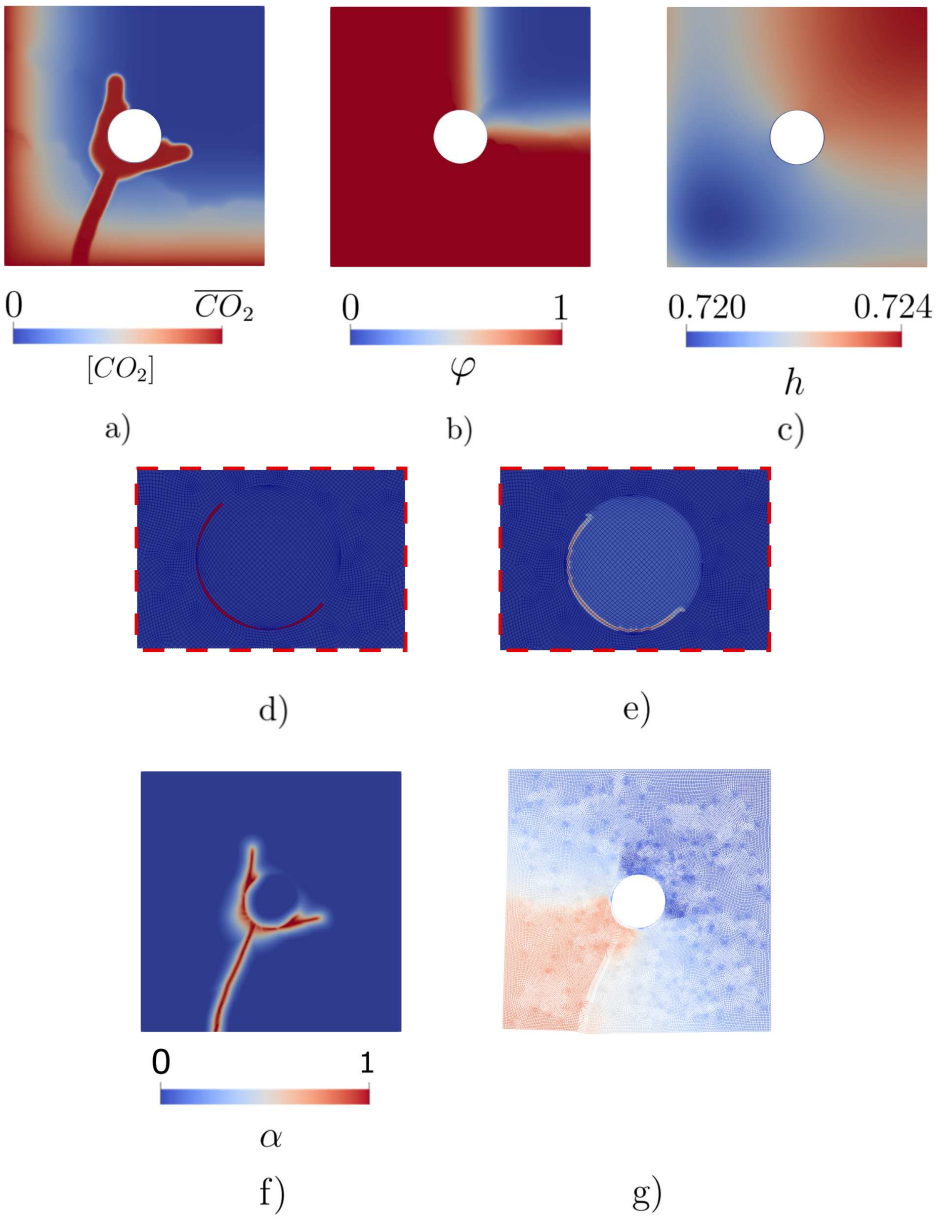

Figure 5.8: Corner rebar test: first cracking of the full depth of the rebar (t = 6598 days). a) Carbon dioxide concentration; b) carbonation front; c) relative humidity; d) zoom on the elements marked as rust; e) zoom on the steel rebar showing the portion of the steel surface under corrosion process; f) damage field; g) deformed configuration of the damaged specimen.

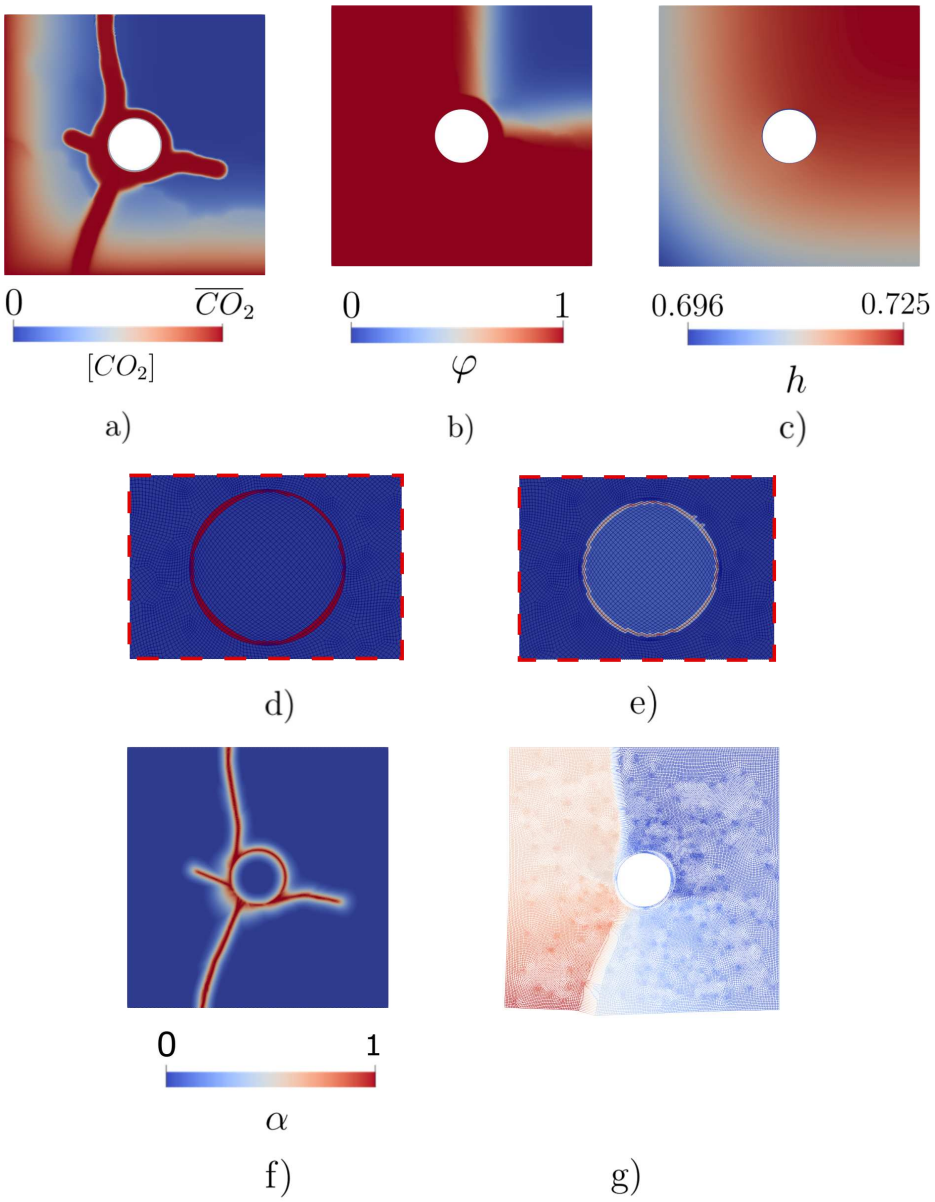

Figure 5.9: Corner rebar test: spalling of the left portion of the concrete cover (t = 11940 days). a) Carbon dioxide concentration; b) Carbonation front; c) relative humidity; zoom on the elements marked as rust; e) zoom on the steel rebar showing the portion of the steel surface under corrosion process; f) damage field; g) deformed configuration of the damaged specimen.

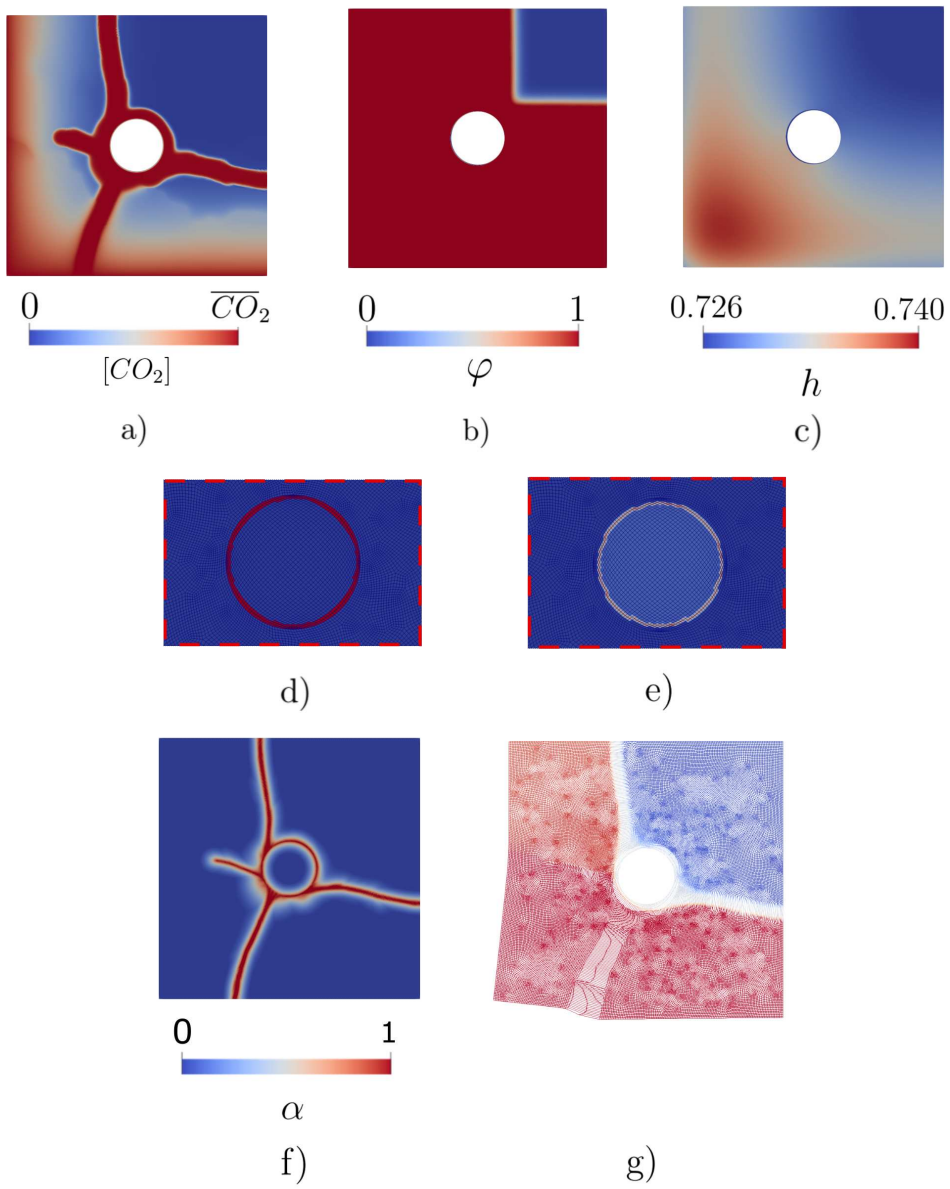

Figure 5.10: Corner rebar test: complete spalling of the concrete cover (t = 18315 days). a) Carbon dioxide concentration; b) Carbonation front; c) relative humidity; d) zoom on the elements marked as rust; e) zoom on the steel rebar showing the portion of the steel surface under corrosion process; f) damage field; g) deformed configuration of the damaged specimen.

5.3 Numerical test: Multi rebars specimen

Lastly, a multi rebars square specimen containing four rebar is studied. The test aims to investigate the degradation process for a realistic reinforced concrete elements in which the interaction between multiple corrosion processes affects the concrete cover cracking and/or spalling.

5.3.1 Test setup and initial condition

A square specimen of standard OPC concrete with w/c = 0.5 of dimensions L = H = 142 mm containing four rebars of diameter 16 mm (labelled as re_i, i = 1, 2, 3, 4) is considered. The mesh discretization of the physical domain has been obtained using 154624 quadrilateral elements with an average cell size of 0.22 mm. Concrete, steel and rust material properties for concrete are reported in table 5.4 while the corrosion parameters values in table 5.3. The inital conditions for the diffusion of the carbon dioxide, moisture transport and oxygen diffusion are given in eq. 5.2. Boundary conditions for moisture transport are presented in eq. 5.3 with the values for $\overline{h}_{en}$ reported in table 2.1. The carbon dioxyde and oxygen diffusion boundary conditions are expressed in eq. 5.4 while for the mechanical problem the boundary conditions from eq. 5.5 are used. Constant temperature of 25 °C is considered throughout the test. The specimen geometry, boundary conditions and the label assigned to each rebar are shown in fig. 5.11. The simulation has been stopped once full spalling of the concrete cover is observed and a time step $\Delta t = 1$ day has been used.

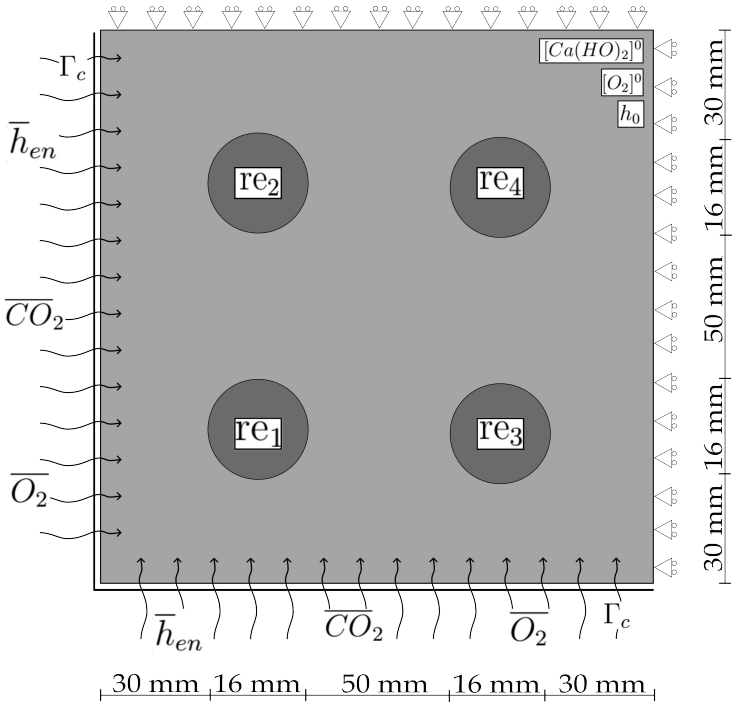

Figure 5.11: Test setup for the multiple rebar specimen test.

5.3.2 Numerical results

The results for the multi rebar specimen are reported in figs. 5.12 through 5.18. Each figure reports the results at a significant time of the degradation process, namely:

- start of the corrosion process at rebar re_1;
- nucleation of cracks in the concrete surrounding the rebar re_1;
- first crack propagation to the left boundary;
- rupture of the concrete around rebar re_1;
- crack propagation from re_1 toward re_2;
- crack propagation to the top boundary of the specimen;
- complete spalling of the cover;

Fig. 5.12 reports the results corresponding to the start of the corrosion process for rebar re_1 at time t = 3127 days ($\sim$ 8.5 years). From fig. 5.12(b) it is possible to observe that a similar carbonation profile compared to the corner rebar test from fig. 5.6(a) is obtained. Carbonation front penetration rate is approximately of 3.50 mm/year. Rust elements are formed accordingly to the direction from which the carbon dioxide enters the specimen, therefore the passive layer dissolves in the lower left portion of the rebar re_1 as visible in 5.12(d). The relative humidity profile is reported in 5.12(c).

In fig. 5.13 the results at time t = 4383 days ($\sim$ 12 years) where the accumulation of the rust over the rebar surface cause the nucleation of cracks on the concrete surrounding re_1. The carbon dioxide, carbonation front and relative humidity are reported in fig. 5.13(a),(b) and (c) respectively. As previously reported, a decrease of the carbonation front penetration rate is observed due to the reduction of the porosity of concrete and the longer path to be covered to reach non-carbonated areas of the specimen. The damage profile is reported in fig. 5.13(e) showing cracks nucleation on the concrete. The rust elements and the rebar surface affected by the corrosion process are reported in fig. 5.13(d). The maximum change in radius associated to rust formation is equal to $\Delta_{r1} = 0.1501$ mm while the maximum corrosion current density at the current time is equal to $i_{corr,1} = 8.13 \cdot 10^{-3}$ [A/m^2]. The oxygen concentration at the steel rebar surface is equal to $[O_2]_r = 8.69 \cdot 10^{-9}$ [mol/mm^2] corresponding to a ratio $[O_2]_r/[O_2]_b = 0.92$.

The first cracking phenomenon is observed at time t = 5041 days ($\sim$ 13.8 years). Fig. 5.14(g) shows the crack propagation from rebar re_1 to the left boundary of the specimen, affecting the whole depth of the concrete cover. The displacement field is reported in fig. 5.14(h) highlighting the opening in the concrete cover due to cracking. Carbon dioxide and oxygen can freely penetrate through the frecture reaching inner portion of the concrete specimen as reported in fig. 5.14(a). Carbonation front and the relative humidity are reported in fig. 5.14(b) and (c) respectively. Fig. 5.14(d),(e) and (f) shows the rust elements and the surface affected by the corrosion current of rebars re_1, re_2 and re_3. A higher portion of re_1 surface is affected by the corrosion process. The maximum change in radius is equal to $\Delta_{r1} = 0.1978$ mm with a maximum value of the corrosion current density equal to $i_{corr,1} = 8.46 \cdot 10^{-3}$ [A/m^2], corresponding to an oxygen concentration ratio of $[O_2]_r/[O_2]_b = 0.89$. Additionally, a small portion of the passive layer of re_2 and re_3 is dissolved, marking the start of the corrosion process for the other two rebars.

Eventually at t = 9426 days ($\sim$ 25.8 years), due to the free access of the carbon dioxide through the crack (5.15(a)), the carbonation profile affected the whole concrete surrounding the rebar as shown in fig. 5.15(b) causing the complete steel surface to depassivate. Rust is formed over the whole circumference of re_1 (fig. 5.15(d)) leading to the debonding between concrete and the rebar as visible in the damage field of fig. 5.15(g). The maximum registered change in radius for re_1 is equal to $\Delta_{r1} = 0.357$ mm while the maximum corrosion current density registered over the rebar surface is equal to $i_{corr,1} = 7.02 \cdot 10^{-3}$ [A/m^2] ($[O_2]_r/[O_2]_b = 0.75$). As previously observed, the formation of rust around the steel rebar partially limit the access of oxygen at the metal surface thus limiting the corrosion current density. Due to corrosion process in rebars re_2 and re_3, rust deposits (fig. 5.15(e),(f)) cause the nucleation of cracks in the concrete surrounding the two rebars as reported in fig. 5.15(g). The changes in radius are respectively $\Delta_{r2} = 0.12$ mm and $\Delta_{r3} = 0.102$ mm.

As the corrosion process continues, delamination of the left portion of the concrete cover is observed at time t = 12308 days ($\sim$ 33.7 years). Due to the free diffusion of the carbon dioxide (fig. 5.16(a)) and oxygen through the concrete cracks, the carbonation (fig. 5.16(b)) and corrosion process (fig. 5.16(d)) exacerbates. Rust formation increases in rebar re_1 with a maximum change in radius equal to $\Delta_{r1} = 0.48$ mm and with a maximum value of the corrosion current density registered on the metal surface equal to $i_{corr,1} = 8.71 \cdot 10^{-3}$ [A/m^2] ($[O_2]_r/[O_2]_b = 0.93$). Accordingly, cracks propagate from re_1 toward re_2 causing the delamination of the left portion of the concrete cover as reported in fig. 5.16(g). Due to the delamination, carbon dioxide can reach rebar re_2 through the new path opened resulting in a larger portion of the rebar affected by corrosion (fig. 5.16(e)) compared to rebar r_3 fig. 5.16(f)). Maximum value of change in radius due to rust deposits are respectively $\Delta_{r2} = 0.28$ mm and $\Delta_{r3} = 0.15$ mm.

Cracking of the top side of the specimen is observed at t = 16024 mm ($\sim$ 43 years). Since the carbon dioxide has now a free path connecting the outer environment to both re_1 and re_2 rebars (5.17(a)), the concrete surrounding the two rebars is completely affected by the carbonation process (5.17(b)). Therefore, corrosion of re_1 and re_2 caused a noticeable increase in the rust deposits as visible from fig. 5.17(d),(e) with a maximum value of the change in radius equal to $\Delta_{r1} = 0.62$ mm and $\Delta_{r2} = 0.34$ mm. The maximum corrosion current density value around rebar re_1 is equal to $i_{corr,1} = 8.53 \cdot 10^{-3}$ [A/m^2] ($[O_2]_r/[O_2]_b = 0.90$). Due to the increase in the rust deposit volume cracks propagate to reach the top boundary of the specimen (fig. 5.17(g)) causing the separation of the left side of the cover as shown in fig. 5.17(h).

Lastly, complete spalling of the concrete cover develops at t = 19301 days ($\sim$ 52.8 years). Carbonation profile has completely covered all the three rebars (fig. 5.17(b)) causing their complete depassivation as visible in figs. 5.18(d),(e),(f). Rust is produced over the whole circumference of the three rebars with changes in radius equal to $\Delta_{r1} = 0.83$ mm, $\Delta_{r2} = 0.5$ mm and $\Delta_{r3} = 0.3$ mm. As a result, cracks propagate from rebar re_1 toward re_3 reaching the right boundary of the specimen (5.18(g)) causing the complete spalling of the cover as visible from the displacement field reported in fig. 5.18(h). Some numerical difficulties manifested during the resolution of this test, as some excessive diffusion of the damage field is evidenced in fig. 5.18(g). This phenomenon, already been documented in [71], does not compromise the quality of the solution and occurs over the concrete surrounding rebar re_1 once spalling of a portion of the concrete cover is observed. A way to overcome this drawback is under investigation.

The numerical simulation for the multi rebar test has been performed using an Intel

i7-11800H. The total time required to perform a single run of the multi rebar test solving algorithm is equal to 127263 ms. The % of the total time required for each single portion of the solving algorithm are reported in Table 5.6. Similarly from the results reported for the corner rebar test, the elasticity problem occupies the largest amount of the run time while the scalar problem solution requires similar times. The least amount of time is required to evaluate the corrosion process over the depassivated portion of the rebar.

Section of the algorithm	% of the run time
Moisture transport	7.51%
CO_2 diffusion-reaction	5.16%
Rebar corrosion	0.34%
Displacement sub-problem iteration	76.80%
Damage sub-problem iteration	10.19%

Table 5.6: Average run time % for each section of the algorithm for the multi rebar test.

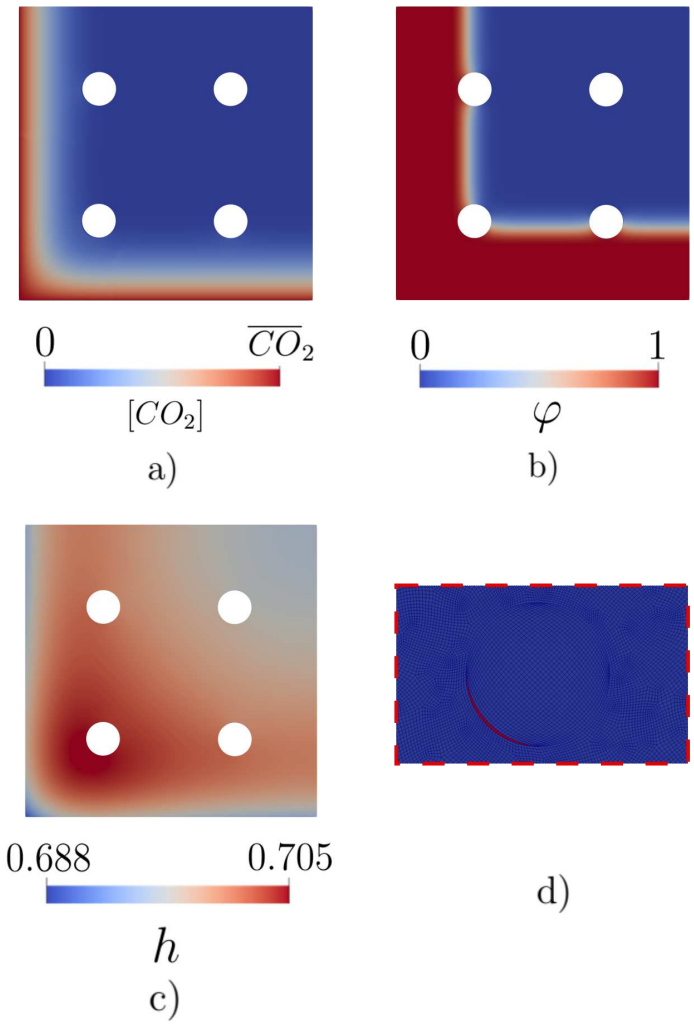

Figure 5.12: Multi rebars test: results at the start of the corrosion process (t = 3127 days). a) Carbon dioxide concentration; b) carbonation front; c) relative humidity; d) zoom of the elements marked as rust for rebar re_1.

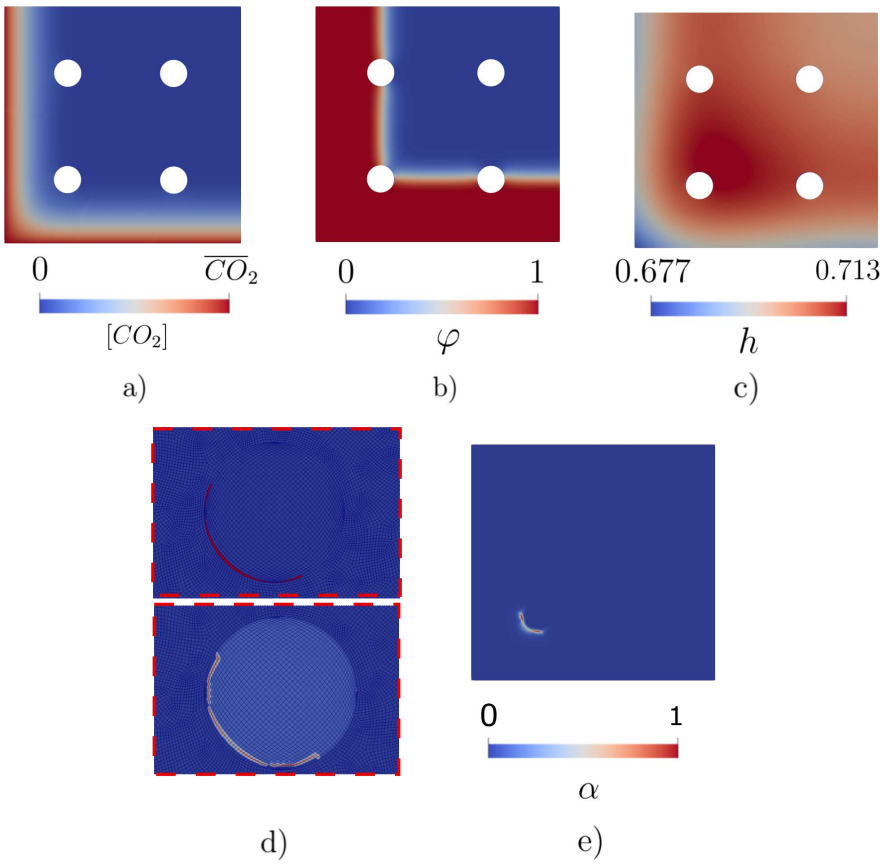

Figure 5.13: Multi rebars test: crack nucleation in the concrete around rebar re_1 (t = 4383 days). a) Carbon dioxide concentration; b) carbonation front; c) relative humidity; d) zoom on the rust elements (top) and on the portion of the steel surface affected by corrosion (bot) of rebar re_1; e) damage field.

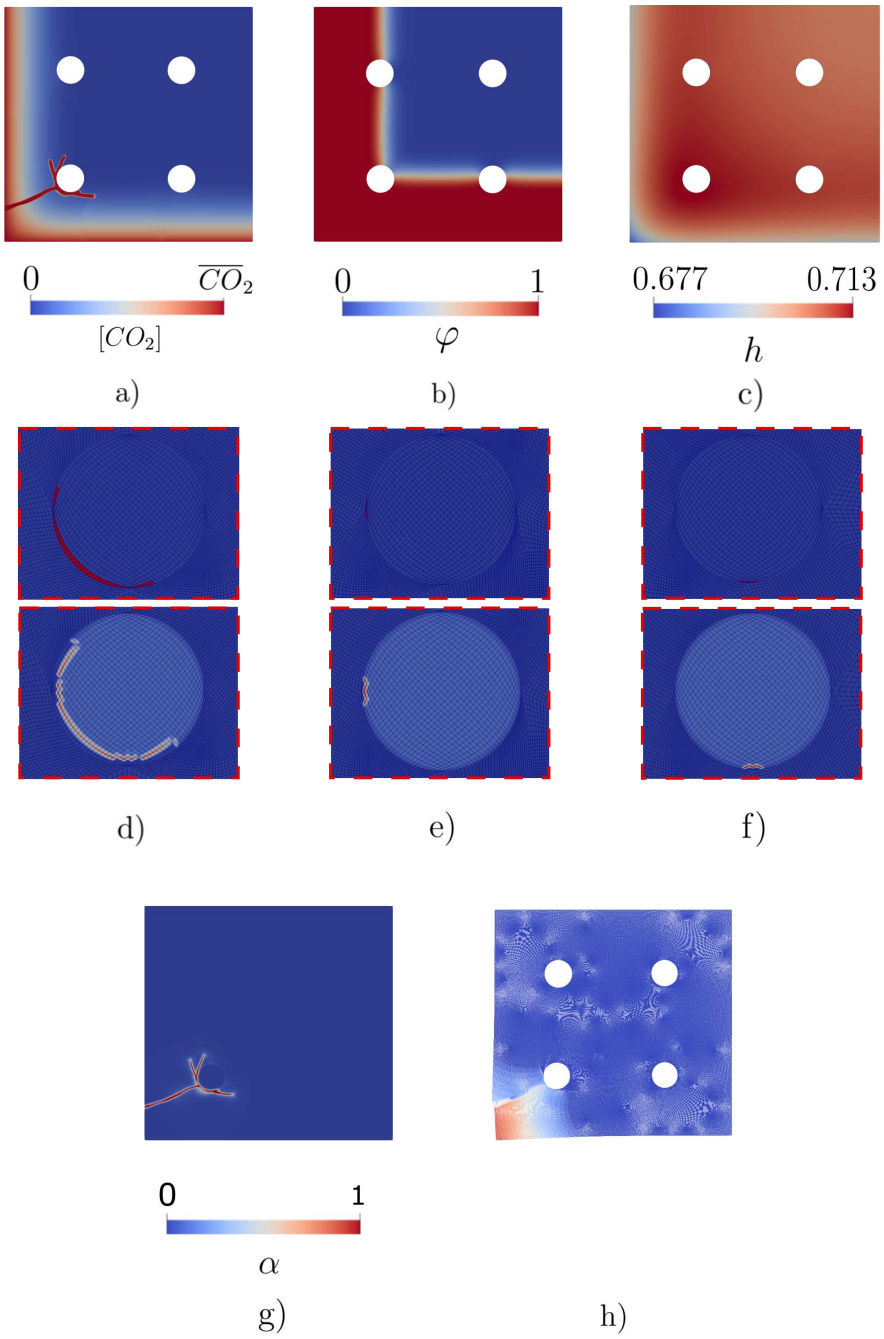

Figure 5.14: Multi rebars test: crack propagation to the left side of the boundary (t = 5041 days). a) Carbon dioxide concentration; b) carbonation front; c) relative humidity; d) zoom on the rust elements (top) and on the portion of the steel surface affected by corrosion (bot) of rebar re_1; e) zoom on the rust elements (top) and on the portion of the steel surface affected by corrosion (bot) of rebar re_2; f) zoom on the rust elements (top) and on the portion of the steel surface affected by corrosion (bot) of rebar re_3; g) damage field; h) displacement filed.

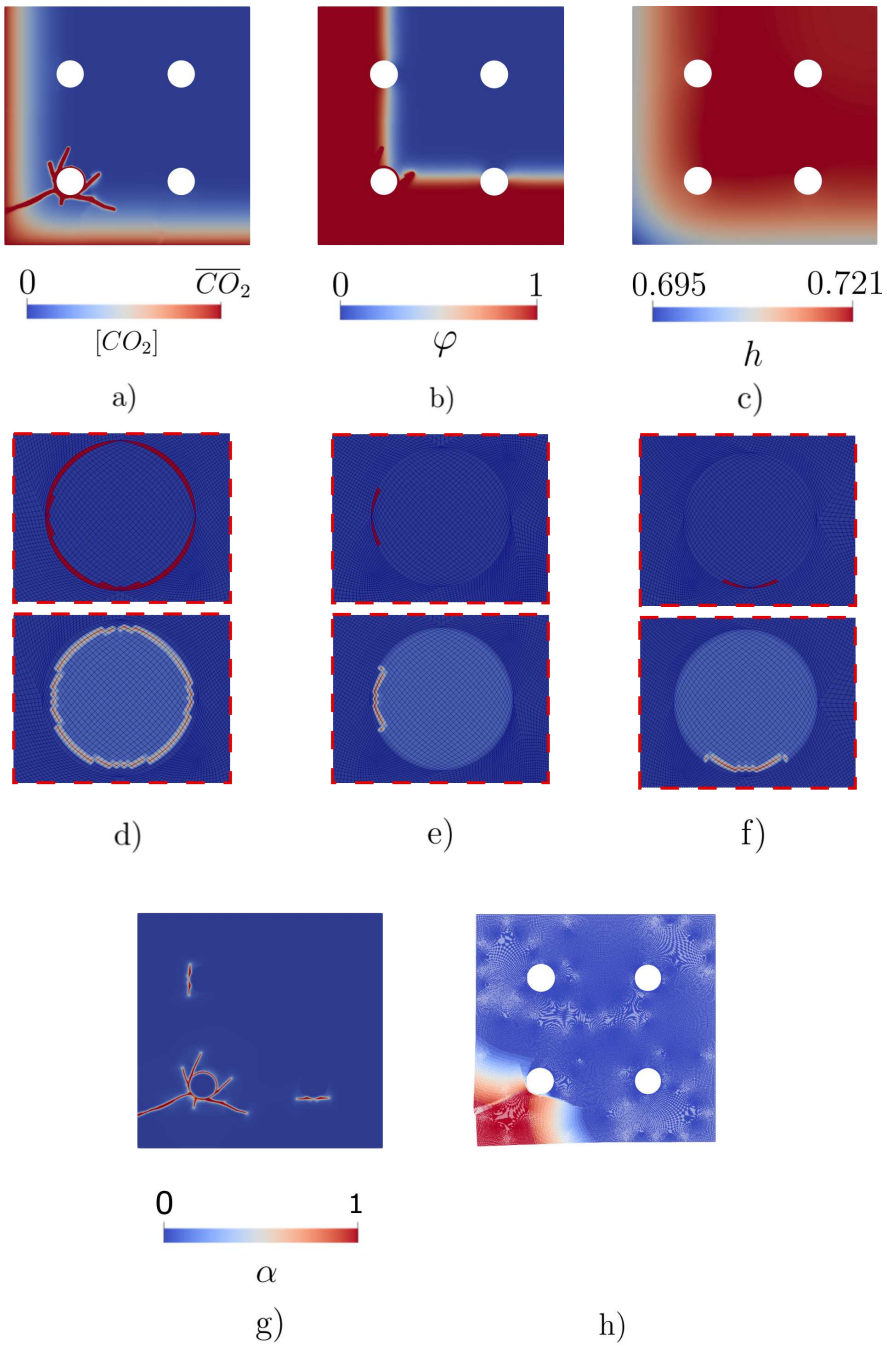

Figure 5.15: Multi rebars test: rupture of concrete around re_1 (t = 9426 days). a) Carbon dioxide concentration; b) carbonation front; c) relative humidity; d) zoom on the rust elements (top) and on the portion of the steel surface affected by corrosion (bot) of rebar re_1; e) zoom on the rust elements (top) and on the portion of the steel surface affected by corrosion (bot) of rebar re_2; f) zoom on the rust elements (top) and on the portion of the steel surface affected by corrosion (bot) of rebar re_3; g) damage field; h) displacement filed.

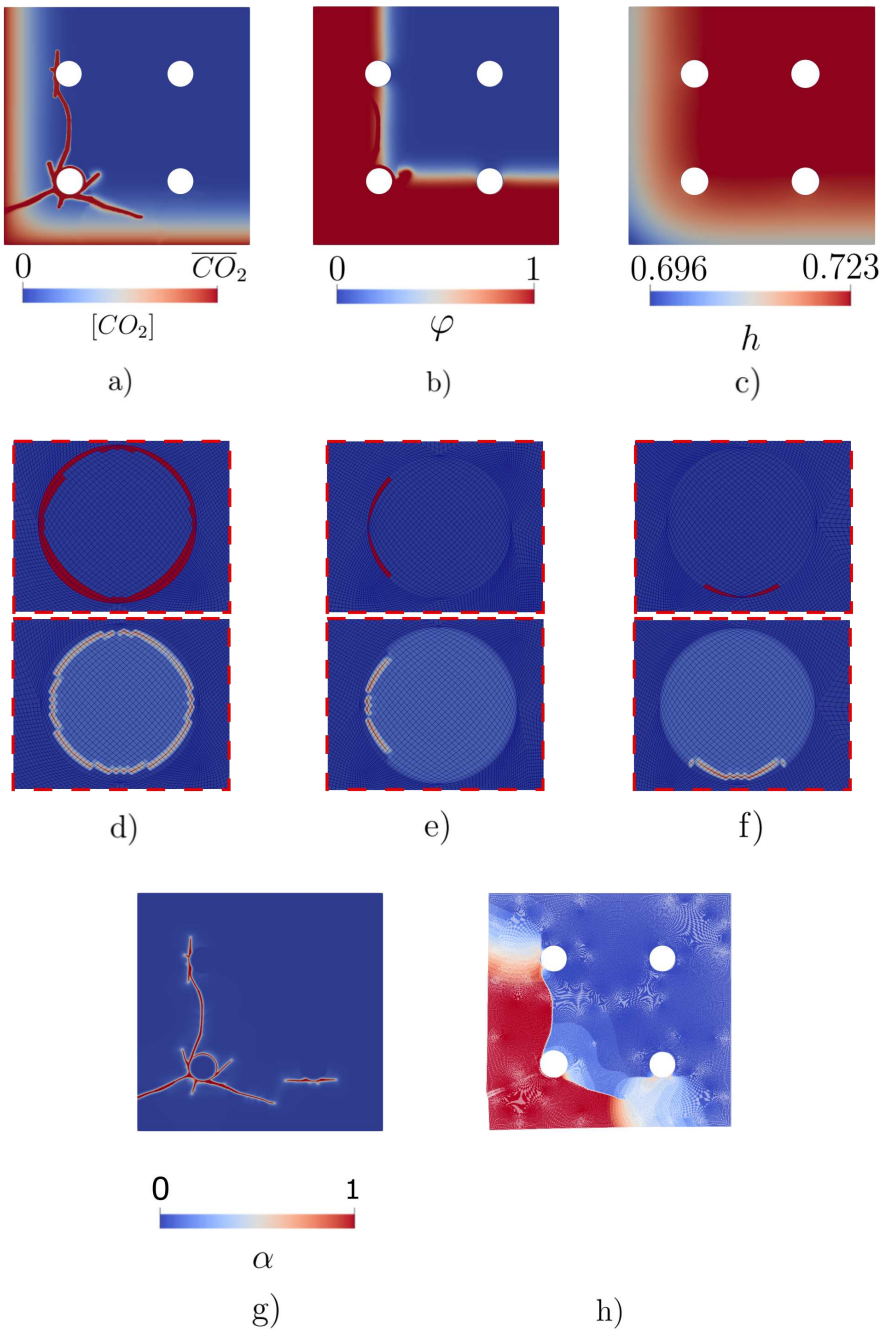

Figure 5.16: Multi rebars test: crack propagation from re_1 to re_2 (t = 12308 days). a) Carbon dioxide concentration; b) carbonation front; c) relative humidity; d) zoom on the rust elements (top) and on the portion of the steel surface affected by corrosion (bot) of rebar re_1; e) zoom on the rust elements (top) and on the portion of the steel surface affected by corrosion (bot) of rebar re_2; f) zoom on the rust elements (top) and on the portion of the steel surface affected by corrosion (bot) of rebar re_3; g) damage field; h) displacement filed.

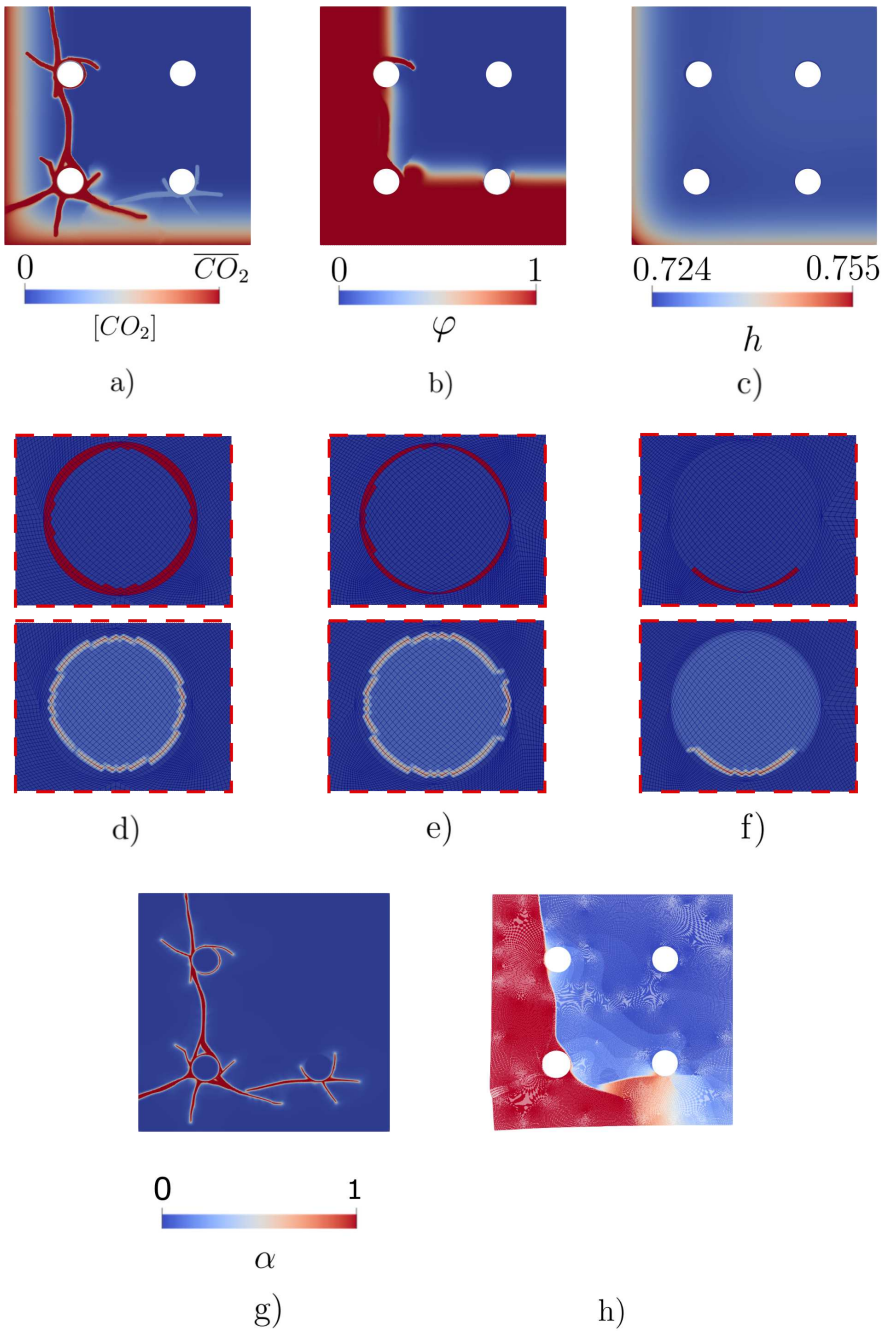

Figure 5.17: Multi rebars test: crack propagation to the top side of the boundary (t = 16024 days). a) Carbon dioxide concentration; b) carbonation front; c) relative humidity; d) zoom on the rust elements (top) and on the portion of the steel surface affected by corrosion (bot) of rebar re_1; e) zoom on the rust elements (top) and on the portion of the steel surface affected by corrosion (bot) of rebar re_2; f) zoom on the rust elements (top) and on the portion of the steel surface affected by corrosion (bot) of rebar re_3; g) damage field; h) displacement filed.

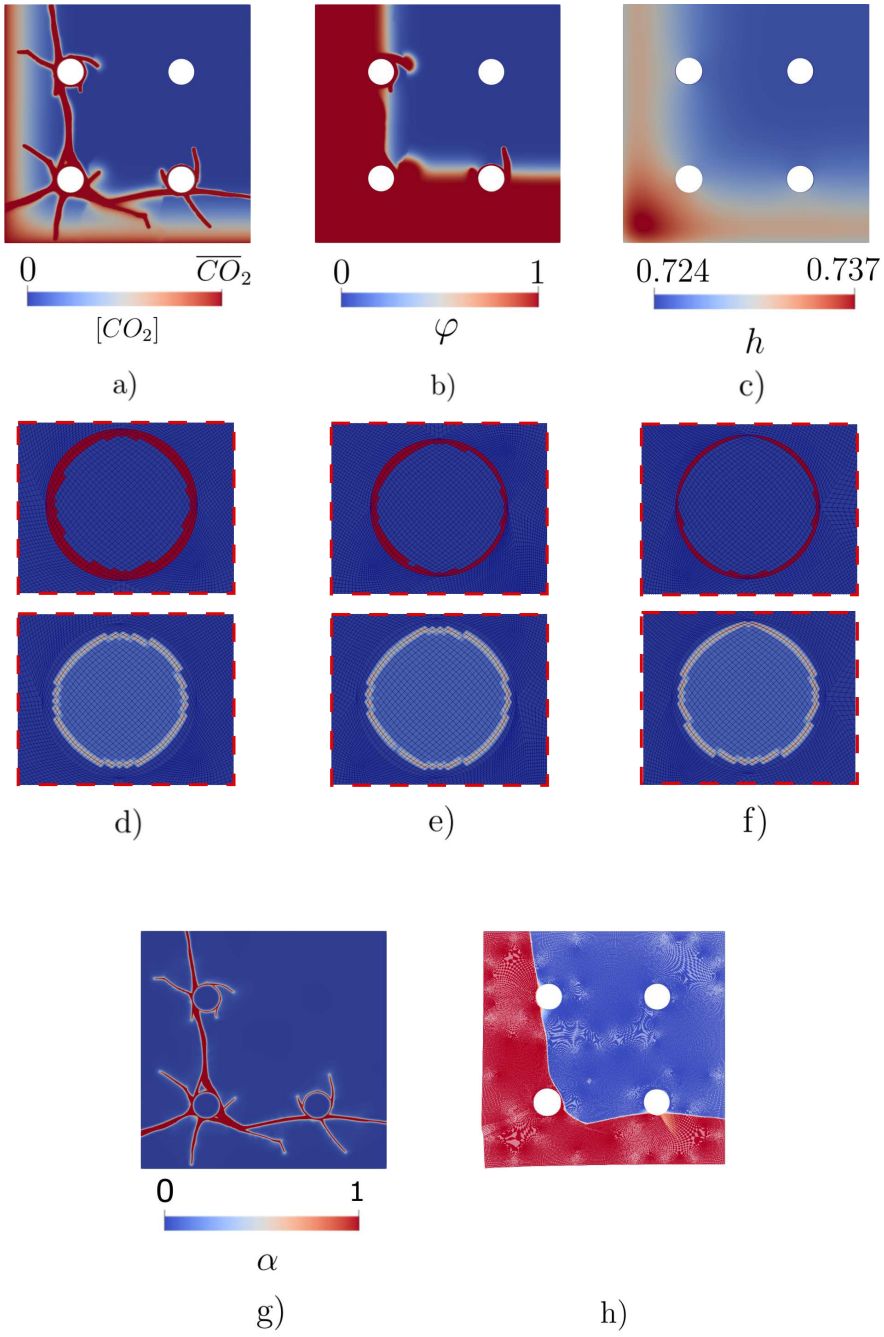

Figure 5.18: Multi rebars test: spalling of the concrete cover (t = 19301 days). a) Carbon dioxide concentration; b) carbonation front; c) relative humidity; d) zoom on the rust elements (top) and on the portion of the steel surface affected by corrosion (bot) of rebar re_1; e) zoom on the rust elements (top) and on the portion of the steel surface affected by corrosion (bot) of rebar re_2; f) zoom on the rust elements (top) and on the portion of the steel surface affected by corrosion (bot) of rebar re_3; g) damage field; h) displacement filed.

Chapter 6

Conclusions

6.1 Conclusions

The carbonation corrosion degradation phenomena in reinforced concrete elements has been analysed via the development of a predictive numerical model.

Carbon dioxide diffusion process through concrete pores has been studied and the chemical reactions that define carbonation process described. Coupling the diffusion-reaction of the CO_2 with moisture transport within concrete pores, allowed to account for the variations in the penetration rate of carbonation process due to changes in the relative humidity content of concrete. Modifications to material porosity due to the formation of calcium carbonate has been considered, and the porosity reduction has been accounted while describing carbon dioxide, oxygen and moisture diffusion processes within concrete pores. Changes to the mechanical material properties have been introduced into the formulation via the usage of a linear function which depends on the carbonation state of the material.

Modelling of the pH drop within the concrete pores allowed to describe precisely the depassivation of steel rebar due to carbonation process, identifying the portions of the rebar on which corrosion initiates. A pointwise evaluation of the corrosion current density has been performed over the depassivated areas. Description of the rust deposits formation has been performed accounting for the moisture and oxygen presence on each point of rebar surface. Additionally, as the corrosion products are formed, the change of steel cross section of rebar has been tracked to define the correct steel elements, underlying the rust deposits, on which evaluation of the corrosion current density has been performed. Reduction effects on the corrosion rate due to rust formation, which creates a layer that moisture and oxygen need to penetrate in order to reach the new metal surface, have been considered. Different trigger mechanisms are considered for the portion of the rebar whose elements are adjacent to concrete elements (pH controlled) and the portion of the rebar elements adjacent to rust rust elements(moisture and oxygen diffusion controlled). Lastly, from the value of swelling of rebar associated with volume expansion due to rust formation, the damage mechanism of the concrete cover has been described using the phase field model for fracture.

Each process has been validated against experimental evidences from the literature. Both natural and accelerated carbonation results have been considered highlighting the capability of the model to account changes to carbonation front penetration rate due to different environmental concentration of carbon dioxide. Description of moisture transport within the model reflects correctly experimental results. Values obtained for the corrosion rate due to carbonation correspond to those present in the literature. Two representative examples have

been investigated, a corner rebar specimen and a four rebars specimen. The simple setting of the first test allowed to present in detail the interactions between moisture, carbonation, corrosion and cracking. As the carbonation front advances within the concrete cover reaching the steel rebar, the drop in the pH value causes the initiation of the corrosion process. The rust formation around the circumference of the rebar accurately follows the advancement of the carbonation profile as the passive layer is dissolved over an increasing portion of the rebar. Variations on the corrosion current density based on the oxygen access to the underlying metal surface have also been reported. Lastly, propagation of cracks due to formation of rust proved to be a highly detrimental effect to the concrete specimen as once openings to the external environment are formed, the carbonation process rapidly affected completely the concrete around the steel rebar. Eventually, spalling of the concrete cover is observed. The multi rebars test allowed to investigate the capabilities of the model to describe a more complex scenario in which the interactions that rise from the presence of multiple rebars are analysed. In particular, once cracks are formed around the corner rebar and propagate toward the top rebar, delamination of the concrete is observed and an exacerbation of the degradation process is observed compared to the bottom right rebar. However, as debonding and delamination phenomena are observed, an increase of the carbonation rate is reported due to the free access of carbon dioxide to inner portions of concrete specimen until complete spalling of the concrete cover is observed.

6.2 Future work

The current work can be considered as a starting point for the creation of a more complete model to describe the complex process which is the degradation of reinforced concrete elements due to corrosion. Therefore, possible extensions to be incorporated in the analysis are:

1 - addition of a more accurate description of the effects of drying-wetting hysteresis cycle in the model as presented in [63] to obtain a more strong correlation between variations of moisture content within concrete and changes to the corrosion current density;

2 - following [197, 101], consideration of moisture presence within cracks and the resulting effects on the diffusion properties of carbon dioxide and oxygen in the broken areas of the specimen can be added to describe a more realistic diffusion behaviour though cracks;

3 - as recently presented in [198], description of ferrous and ferric ions transport and precipitation within the concrete pores permits to describe the formation of overpressures within the concrete pores thus affecting the cracking behaviour of the concrete cover;

4 - investigations on the damage field diffusive behaviour which manifests once the complete spalling of concrete cover is observed as reported in sec. 5.3.2 and in [71];

5 - introduction of chloride ions into the model to describe the synergistic degradation effects of both uniform and pitting corrosion in reinforced concrete elements;

6 - perform experimental tests to have accurate laboratory results for the various processes of the carbonation corrosion process to accurately calibrate the parameters of the developed model for different environmental scenarios;

7 - application of the model for the investigation of the condition of existing structures. Since the model should describe extremely large domains, usage of mesh adaptive refinement techniques such as [163, 191] are required to lower the computational costs.

Bibliography

[1] G. Mays, Durability of Concrete Structures: Investigation, repair, protection, CRC Press, 1991. URL: https://books.google.it/books?id=EJT2-NbzYFwC.

[2] L. Bertolini, B. Elsener, P. Pedeferri, E. Redaelli, R. Polder, Corrosion of Steel in Concrete: Prevention, Diagnosis, Repair, Wiley, 2014. URL: https://books.google.it/books?id=Nf7IAgAAQBAJ.

[3] C. Meyer, Concrete as a green building material., Construction Materials Mindess Symposium (2005).

[4] A. Kumar, J. S. Rattan, N. R. Kapoor, A. Kumar, R. Kumar, Structural health monitoring of existing reinforced cement concrete buildings and bridge using nondestructive evaluation with repair methodology, in: A. Kaboli, S. Shirowzhan (Eds.), Advances and Technologies in Building Construction and Structural Analysis, IntechOpen, Rijeka, 2021. URL: https://doi.org/10.5772/intechopen.101473. doi:10.5772/intechopen.101473.

[5] F. I. H. Sakiyama, F. Lehmann, H. Garrecht, Structural health monitoring of concrete structures using fibre-optic-based sensors: a review, Magazine of Concrete Research 73 (2021) 174–194.

[6] W. Habel, 4 - structural health monitoring systems for reinforced concrete structures, in: C. Maierhofer, H.-W. Reinhardt, G. Dobmann (Eds.), Non-Destructive Evaluation of Reinforced Concrete Structures, volume 2 of *Woodhead Publishing Series in Civil and Structural Engineering*, Woodhead Publishing, 2010, pp. 63–94. URL: https://www.sciencedirect.com/science/article/pii/B978184569950550004X. doi:https://doi.org/10.1533/9781845699604.1.63.

[7] F. Freddi, L. Mingazzi, A predictive phase-field approach for cover cracking in corroded concrete elements, Theoretical and Applied Fracture Mechanics 122 (2022) 103657.

[8] V. G. Papadakis, C. G. Vayenas, M. N. Fardis, Fundamental modeling and experimental investigation of concrete carbonation, Materials 88 (1991) 363–373.

[9] O. Burkan Isgor, A. Razaqpur, Finite element modeling of coupled heat transfer, moisture transport and carbonation processes in concrete structures, Cement and Concrete Composites 26 (2004) 57–73.

[10] B. Huet, V. L'hostis, G. Santarini, D. Feron, H. Idrissi, Steel corrosion in concrete: Determinist modeling of cathodic reaction as a function of water saturation degree, Corrosion Science 49 (2007) 1918–1932.

[11] P. Pedeferri, L. Lazzari, M. Pedeferri, Corrosion Science and Engineering, Engineering materials, Springer, 2018. URL: https://books.google.it/books?id=GtXXwQEACAAJ.

[12] J.-Y. Wu, V. P. Nguyen, C. T. Nguyen, D. Sutula, S. Sinaie, S. Bordas, Phase-field modelling of fracture, Adv. Appl. Mech. (2019).

[13] F. Freddi, G. Royer-Carfagni, Regularized variational theories of fracture: A unified approach, Journal of the Mechanics and Physics of Solids 58 (2010) 1154 – 1174.

[14] N. Renne, P. Kara De Maeijer, B. Craeye, M. Buyle, A. Audenaert, Sustainable assessment of concrete repairs through life cycle assessment (lca) and life cycle cost analysis (lcca), Infrastructures 7 (2022).

[15] M. Furinghetti, A. Pavese, F. Lunghi, D. Silvestri, Strategies of structural health monitoring for bridges based on cloud computing, Journal of Civil Structural Health Monitoring 9 (2019).

[16] K. Tuutti, Corrosion of Steel in Concrete, CBI forskning, Swedish Cement and Concrete Research Institute, 1982. URL: https://books.google.it/books?id=WTE3AQAAIAAJ.

[17] A. A. Leòn Baldelli, On fracture of thin films : a variational approach, Ph.D. thesis, 2013. URL: http://www.theses.fr/2013PA066514, thèse de doctorat dirigée par Marigo, Jean-Jacques et Maurini, Corrado Mécanique Paris 6 2013.

[18] O. B. Isgor, A durability model for chloride and carbonation induced steel corrosion in reinforced concrete members, 2001.

[19] D. Breysse, 3 - deterioration processes in reinforced concrete: an overview, in: C. Maierhofer, H.-W. Reinhardt, G. Dobmann (Eds.), Non-Destructive Evaluation of Reinforced Concrete Structures, volume 1 of *Woodhead Publishing Series in Civil and Structural Engineering*, Woodhead Publishing, 2010, pp. 28–56. URL: https://www.sciencedirect.com/science/article/pii/B9781845695606500039. doi:https://doi.org/10.1533/9781845699536.1.28.

[20] J. Bai, 16 - durability of sustainable construction materials, in: J. M. Khatib (Ed.), Sustainability of Construction Materials (Second Edition), Woodhead Publishing Series in Civil and Structural Engineering, second edition ed., Woodhead Publishing, 2016, pp. 397–414. URL: https://www.sciencedirect.com/science/article/pii/B9780081003701000160. doi:https://doi.org/10.1016/B978-0-08-100370-1.00016-0.

[21] L. Bertolini, B. Elsener, P. Pedeferri, E. Redaelli, R. B. Polder, Corrosion of Steel in Concrete: Prevention, Diagnosis, Repair, 2nd Edition, 2nd ed., Wiley-VCH, 2013.

[22] Ministero delle Infrastrutture e dei Trasporti, Norme tecniche per le costruzioni, NTC, Rome, 2008.

[23] EN 1992-1-1 Eurocode 2: Design of concrete structures - Part 1-1: General ruels and rules for buildings, EN, CEN, Brussels, 2004.

[24] J. Guo, W. Sun, Y. Xu, W. Lin, W. Jing, Damage mechanism and modeling of concrete in freeze-thaw cycles: A review, Buildings 12 (2022).

[25] J. Duchesne, A. Bertron, Leaching of Cementitious Materials by Pure Water and Strong Acids (HCl and HNO3), Springer Netherlands, Dordrecht, 2013, pp. 91–112. URL: https://doi.org/10.1007/978-94-007-5413-3_4. doi:10.1007/978-94-007-5413-3_4.

[26] W. G. Hime, B. Mather, "sulfate attack," or is it?, Cement and Concrete Research 29 (1999) 789–791.

[27] W. Chen, B. Huang, Y. Yuan, M. Deng, Deterioration process of concrete exposed to internal sulfate attack, Materials 13 (2020).

[28] B. Fournier, M.-A. Bérubé, Alkali-aggregate reaction in concrete: a review of basic concepts and engineering implications, Canadian Journal of Civil Engineering 27 (2000) 167–191.

[29] A. Neville, Chloride attack of reinforced concrete: an overview, Materials and Structures 28 (1995).

[30] B. Šavija, M. Luković, Carbonation of cement paste: Understanding, challenges, and opportunities, Construction and Building Materials 117 (2016) 285–301.

[31] E. Kangni-Foli, S. Poyet, P. Le Bescop, T. Charpentier, F. Bernachy-Barbé, A. Dauzères, E. L'Hôpital, J.-B. d'Espinose de Lacaillerie, Carbonation of model cement pastes: The mineralogical origin of microstructural changes and shrinkage, Cement and Concrete Research 144 (2021) 106446.

[32] M. Richardson, Fundamentals of Durable Reinforced Concrete, Modern Concrete Technology, Taylor & Francis Limited, 2019. URL: https://books.google.it/books?id=J4RezAEACAAJ.

[33] I. Yuksel, G. B. Sakcalı, Effects of reinforcement corrosion on reinforced concrete buildings, Proceedings of the Institution of Civil Engineers - Structures and Buildings 175 (2022) 244–258.

[34] C. Andrade, P. Merino, X. Nóvoa, M. Pérez, L. Soler, Passivation of reinforcing steel in concrete, in: Electrochemical Methods in Corrosion Research V, volume 192 of *Materials Science Forum*, Trans Tech Publications Ltd, 1995, pp. 891–898. doi:10.4028/www.scientific.net/MSF.192-194.891.

[35] N. V. Rao, T. Meena, A review on carbonation study in concrete, IOP Conference Series: Materials Science and Engineering 263 (2017) 032011.

[36] U. Angst, F. Moro, M. Geiker, S. Kessler, H. Beushausen, C. Andrade, J. Lahdensivu, A. Köliö, K. ichi Imamoto, S. V. Greve-Dierfeld, M. Serdar, Corrosion of steel in carbonated concrete: mechanisms, practical experience, and research priorities – a critical review by RILEM TC 281-CCC, RILEM Technical Letters 5 (2020) 85–100.

[37] J. González, C. Andrade, C. Alonso, S. Feliu, Comparison of rates of general corrosion and maximum pitting penetration on concrete embedded steel reinforcement, Cement and Concrete Research 25 (1995) 257–264.

[38] K. Akpanyung, R. Loto, Pitting corrosion evaluation: a review, Journal of Physics: Conference Series 1378 (2019) 022088.

[39] J. Blunden, T. Boyer, State of the climate in 2020, Bulletin of the American Meteorological Society 102 (2021) S1–S475.

[40] J. M. Chi, R. Huang, C. C. Yang, Effects of carbonation on mechanical properties and durability of concrete using accelerated testing method, Journal of Marine Science and Technology 10 (2002).

[41] M. A. Sanjuán, C. Andrade, M. Cheyrezy, Concrete carbonation tests in natural and accelerated conditions, Advances in Cement Research 15 (2003) 171–180.

[42] D. Ho, R. Lewis, Carbonation of concrete and its prediction, Cement and Concrete Research 17 (1987) 489–504.

[43] K. You, H. Jeong, W. Hyung, Effects of accelerated carbonation on physical properties of mortar, Journal of Asian Architecture and Building Engineering 13 (2014) 217–221.

[44] K. Suda, S. Misra, K. Motohashi, Corrosion products of reinforcing bars embedded in concrete, Corrosion Science 35 (1993) 1543–1549.

[45] V. G. Papadakis, C. G. Vayenas, M. N. Fardis, Physical and chemical characteristics affecting the durability of concrete, Materials 88 (1991) 186–196.

[46] A. V. Saetta, B. A. Schrefler, R. V. Vitaliani, The carbonation of concrete and the mechanism of moisture, heat and carbon dioxide flow through porous materials, Cement and Concrete Research 23 (1993) 761–772.

[47] A. V. Saetta, R. V. Scotta, R. V. Vitaliani, Analysis of chloride diffusion into partially saturated concrete, ACI Materials Journal 90 (1993).

[48] O. Burkan Isgor, A. Razaqpur, Finite element modeling of coupled heat transfer, moisture transport and carbonation processes in concrete structures, Cement and Concrete Composites 26 (2004) 57–73.

[49] Z. Bažant, L. Najjar, Drying of concrete as a nonlinear diffusion problem, Cement and Concrete Research 1 (1971) 461–473.

[50] Y. Xi, Z. P. Bažant, H. M. Jennings, Moisture diffusion in cementitious materials adsorption isotherms, Advanced Cement Based Materials 1 (1994) 248–257.

[51] Y. Xi, Z. P. Bažant, L. Molina, H. M. Jennings, Moisture diffusion in cementitious materials moisture capacity and diffusivity, Advanced Cement Based Materials 1 (1994) 258–266.

[52] M. Chapwanya, W. Liu, J. Stockie, A model for reactive porous transport during re-wetting of hardened concrete, Journal of Engineering Mathematics 65 (2009) 53–73.

[53] G. Bretti, M. Ceseri, R. Natalini, A moving boundary problem for reaction and diffusion processes in concrete: Carbonation advancement and carbonation shrinkage, 2022. URL: /article/id/6253facc2d80b72b3d8d6e9a. doi:10.3934/dcdss.2022092.

[54] G. Bretti, M. Ceseri, R. Natalini, M. C. Ciacchella, M. L. Santarelli, G. Tiracorrendo, A forecasting model for the porosity variation during the carbonation process, International Journal on Geomathematics 13 (2022).

[55] Q. T. Phung, N. Maes, D. Jacques, G. D. Schutter, G. Ye, J. Perko, Modelling the carbonation of cement pastes under a CO2 pressure gradient considering both diffusive and convective transport, Construction and Building Materials 114 (2016) 333–351.

[56] A. Muntean, M. Böhm, J. Kropp, Moving carbonation fronts in concrete: A moving-sharp-interface approach, Chemical Engineering Science 66 (2011) 538–547.

[57] Z. P. Bažant, Physical model for steel corrosion in concrete sea structures—theory, Journal of the Structural Division 105 (1979) 1137–1153.

[58] O. B. Isgor, A. G. Razaqpur, Modelling steel corrosion in concrete structures, Materials and Structures 39 (2006).

[59] J. Ge, O. Isgor, Effects of tafel slope, exchange current density and electrode potential on the corrosion of steel in concrete, Materials and Corrosion 58 (????) 573–582.

[60] C.-Y. Kim, J.-K. Kim, Numerical analysis of localized steel corrosion in concrete, Construction and Building Materials 22 (2008) 1129–1136.

[61] G. Zhang, Y. Zhu, X. Lin, Y. Tian, H. Ye, X. Jin, N. Jin, D. Yan, F. Xiao, K. Yao, J. Chen, Numerical simulation of electrochemical mechanism of steel rebar corrosion in concrete under natural climate with time-varying temperature and humidity, Construction and Building Materials 306 (2021) 124873.

[62] B. Martin-Perez, Service life modelling of r.c. highway structures exposed to chlorides, 1999.

[63] M. Stefanoni, U. Angst, B. Elsener, The mechanism controlling corrosion of steel in carbonated cementitious materials in wetting and drying exposure, Cement and Concrete Composites 113 (2020) 103717.

[64] C. Andrade, C. Alonso, F. J. Molina, Cover cracking as a function of bar corrosion: Part i-experimental test, Materials and Structures 26 (1993) 453–464.

[65] F. J. Molina, C. Alonso, C. Andrade, Cover cracking as a function of bar corrosion: Part 2 - numerical model, Materials and Structures 26 (1993) 532–548.

[66] M. Stefanoni, U. Angst, B. Elsener, Corrosion rate of carbon steel in carbonated concrete – a critical review, Cement and Concrete Research 103 (2018) 35–48.

[67] Q. T. Nguyen, A. Millard, S. Caré, V. L'Hostis, Y. Berthaud, Fracture of concrete caused by the reinforcement corrosion products, Journal de Physique IV (Proceedings) 136 (2006) 109–120.

[68] J. Zhao, Z. Chen, J. Mehrmashhadi, F. Bobaru, A stochastic multiscale peridynamic model for corrosion-induced fracture in reinforced concrete, Engineering Fracture Mechanics 229 (2020) 106969.

[69] Y. Zhang, R. K. L. Su, Corner cracking model for non-uniform corrosion-caused deterioration of concrete covers, Construction and Building Materials 234 (2020) 117410.

[70] F. Freddi, L. Mingazzi, Phase-field simulations of cover cracking in corroded RC beams, Procedia Structural Integrity 33 (2021) 371–384.

[71] F. Freddi, L. Mingazzi, A predictive phase-field approach for cover cracking in corroded concrete elements, Theoretical and Applied Fracture Mechanics 122 (2022) 103657.

[72] A. A. Griffith, The phenomena of rupture and flow in solids, Philosophical Transactions of the Royal Society of London A221 (1921) 163–198.

[73] L. Ambrosio, V. M. Tortorelli, Approximation of functionals depending on jumps by elliptic functionals via Γ-convergence, Comm. Pure Appl. Math. 43 (1990) 999–1036.

[74] L. Chen, R. de Borst, Phase-field modelling of cohesive fracture, European Journal of Mechanics - A/Solids 90 (2021) 104343.

[75] Y. Feng, J. Li, Phase-field cohesive fracture theory: A unified framework for dissipative systems based on variational inequality of virtual works, Journal of the Mechanics and Physics of Solids 159 (2022) 104737.

[76] H. Amor, J.-J. Marigo, C. Maurini, Regularized formulation of the variational brittle fracture with unilateral contact: Numerical experiments, Journal of the Mechanics and Physics of Solids 57 (2009) 1209 – 1229.

[77] F. Freddi, G. Royer-Carfagni, Variational fracture mechanics to model compressive splitting of masonry-like materials, Annals of Solid and Structural Mechanics 2 (2011) 57–67.

[78] A. Chambolle, S. Conti, G. A. Francfort, Approximation of a brittle fracture energy with a constraint of non-interpenetration, Arch. Rational Mech. Anal. 228 (2018) 867–889.

[79] G. Lancioni, G. Royer-Carfagni, The variational approach to fracture mechanics. a practical application to the french panthéon in paris, Journal of Elasticity 95 (2009) 1–30.

[80] M. Cervera, M. Chiumenti, C. A. de Saracibar, Shear band localization via local j2 continuum damage mechanics, Computer Methods in Applied Mechanics and Engineering 193 (2004) 849–880.

[81] R. Alessi, F. Freddi, L. Mingazzi, Phase-field numerical strategies for deviatoric driven fractures, Computer Methods in Applied Mechanics and Engineering 359 (2020) 112651.

[82] R. Alessi, F. Freddi, Failure and complex crack patterns in hybrid laminates: A phase-field approach, Compos. Part. B-Eng. 179 (2019).

[83] A. A. León Baldelli, J. F. Babadjian, B. Bourdin, D. Henao, C. Maurini, A variational model for fracture and debonding of thin films under in-plane loadings, Journal of the Mechanics and Physics of Solids 70 (2014) 320–348.

[84] R. Alessi, F. Freddi, Phase-field modelling of failure in hybrid laminates, Composite Structures 181 (2017) 9 – 25.

[85] F. Freddi, L. Mingazzi, Phase field simulation of laminated glass beam, Materials 13 (2020) 3218.

[86] R. Alessi, J.-J. Marigo, S. Vidoli, Gradient Damage Models Coupled with Plasticity and Nucleation of Cohesive Cracks, Archive for Rational Mechanics and Analysis 214 (2014) 575–615.

[87] F. Freddi, G. Royer-Carfagni, Plastic flow as an energy minimization problem. Numerical experiments, Journal of Elasticity 116 (2014) 53–74.

[88] F. Freddi, G. Royer-Carfagni, Phase-field slip-line theory of plasticity, Journal of the Mechanics and Physics of Solids 94 (2016) 257–272.

[89] M. Ambati, T. Gerasimov, L. De Lorenzis, Phase-field modeling of ductile fracture, Comput. Mech. 55 (2015) 1017–1040.

[90] R. Alessi, M. Ambati, T. Gerasimov, S. Vidoli, L. D. Lorenzis, Comparison of phase-field models of fracture coupled with plasticity, in: Computational Methods in Applied Sciences, Springer International Publishing, 2017, pp. 1–21. URL: https://doi.org/10.1007/978-3-319-60885-3_1. doi:10.1007/978-3-319-60885-3_1.

[91] R. Alessi, J.-J. Marigo, C. Maurini, S. Vidoli, Coupling damage and plasticity for a phase-field regularisation of brittle, cohesive and ductile fracture: One-dimensional examples, International Journal of Mechanical Sciences (2017).

[92] C. Chukwudozie, B. Bourdin, K. Yoshioka, A variational phase-field model for hydraulic fracturing in porous media, Computer Methods in Applied Mechanics and Engineering 347 (2019) 957–982.

[93] J.-Y. Wu, W.-X. Chen, On the phase-field modeling of fully coupled chemo-mechanical deterioration and fracture in calcium leached cementitious solids, International Journal of Solids and Structures 238 (2022) 111380.

[94] T.-T. Nguyen, D. Waldmann, T. Q. Bui, Phase field simulation of early-age fracture in cement-based materials, International Journal of Solids and Structures 191-192 (2020) 157–172.

[95] T. Wu, L. De Lorenzis, A phase-field approach to fracture coupled with diffusion, Comput. Methods Appl. Mech. Engrg 312 (2016) 196–223.

[96] S. Yu, H. Jin, Modeling of the corrosion-induced crack in concrete contained transverse crack subject to chloride ion penetration, Construction and Building Materials 258 (2020) 119645.

[97] X. Fang, Z. Pan, A. Chen, Phase field modeling of concrete cracking for non-uniform corrosion of rebar, Theoretical and Applied Fracture Mechanics 121 (2022) 103517.

[98] X. Hu, H. Xu, X. Xi, P. Zhang, S. Yang, Meso-scale phase field modelling of reinforced concrete structures subjected to corrosion of multiple reinforcements, Construction and Building Materials 321 (2022) 126376.

[99] B. Johannesson, Nonlinear transient phenomena in porous media with special regard to concrete and durability, Advanced Cement Based Materials 6 (1997) 71–75.

[100] T. Wu, L. De Lorenzis, A phase-field approach to fracture coupled with diffusion, Computer Methods in Applied Mechanics and Engineering 312 (2016) 196–223. Phase Field Approaches to Fracture.

[101] C. Miehe, S. Mauthe, Phase field modeling of fracture in multi-physics problems. part iii. crack driving forces in hydro-poro-elasticity and hydraulic fracturing of fluid-saturated porous media, Computer Methods in Applied Mechanics and Engineering 304 (2016) 619–655.

[102] P. Liu, Y. Chen, Z. Yu, Effects of temperature, relative humidity and carbon dioxide concentration on concrete carbonation, Magazine of Concrete Research 72 (2020) 936–947.

[103] M. Elsalamawy, A. R. Mohamed, E. M. Kamal, The role of relative humidity and cement type on carbonation resistance of concrete, Alexandria Engineering Journal 58 (2019) 1257–1264.

[104] B. Johannesson, Modelling of transport processes involved in service life prediction of concrete : Important principles, 1998.

[105] A. Neville, Properties of Concrete, A Pitman international text, Pitman Pub., 1981. URL: https://books.google.it/books?id=P75RAAAAMAAJ.

[106] A. Buis, The atmosphere: Getting a handle on carbon dioxide – climate change: Vital signs of the planet, 2022. URL: https://climate.nasa.gov/news/2915/the-atmosphere-getting-a-handle-on-carbon-dioxide/.

[107] J. Shen, Q. Xu, Effect of moisture content and porosity on compressive strength of concrete during drying at 105 °c, Construction and Building Materials 195 (2019) 19–27.

[108] K. C. Hover, The influence of water on the performance of concrete, Construction and Building Materials 25 (2011) 3003–3013.

[109] M. Shubaili, A. Elawadi, S. Orton, Y. Tian, Time-dependent behavior of reinforced concrete beams under high sustained loads, Applied Sciences 12 (2022).

[110] P. Gao, Y. Chen, H. Huang, Z. Qian, E. Schlangen, J. Wei, Q. Yu, Effect of relative humidity on drying-induced damage in concrete: A comparative study of digital image correlation and lattice modelling, Materials & Design 196 (2020) 109128.

[111] X. Wang, P. Zhu, S. Yu, H. Liu, Y. Dong, X. Xu, Effect of moisture content on tunnel fire resistance of self-compacting concrete coated with aerogel mortar, Magazine of Concrete Research 73 (2021) 1071–1080.

[112] S. Steiner, B. Lothenbach, T. Proske, A. Borgschulte, F. Winnefeld, Effect of relative humidity on the carbonation rate of portlandite, calcium silicate hydrates and ettringite, Cement and Concrete Research 135 (2020) 106116.

[113] Y. F. Houst, The role of moisture in the carbonation of cementitious materials, Internationale Zeitschrift für Bauinstandsetzen und Baudenkmalpflege 2 (1996) 49–66.

[114] Z. P. Bažant, L. J. Najjar, Nonlinear water diffusion in nonsaturated concrete, Matériaux et Construction 5 (1972) 106116.

[115] S. Brunauer, P. H. Emmett, E. Teller, Adsorption of gases in multimolecular layers, Journal of the American Chemical Society 60 (1938) 309–319.

[116] A. Hillerborg, A modified absorption theory, Cement and Concrete Research 15 (1985) 809–816.

[117] J. Hagymassy, I. Odler, M. Yudenfreund, J. Skalny, S. Brunauer, Pore structure analysis by water vapor adsorption. iii. analysis of hydrated calcium silicates and portland cements, Journal of Colloid and Interface Science 38 (1972) 20–34.

[118] L. E. COPELAND, R. H. BRAGG, Self desiccation in portland cement pastes, Proc. Amer. Soc. for Testing Materials 204 (1955).

[119] Z. P. Bažant, W. Thonguthai, Pore pressure and drying of concrete at high temperature, Journal of the Engineering Mechanics Division 104 (1978) 1059–1079.

[120] A. V. Saetta, B. A. Schrefler, R. V. Vitaliani, 2 — d model for carbonation and moisture/heat flow in porous materials, Cement and Concrete Research 25 (1995) 1703–1712.

[121] A. V. Saetta, R. V. Vitaliani, Experimental investigation and numerical modeling of carbonation process in reinforced concrete structures: Part i: Theoretical formulation, Cement and Concrete Research 34 (2004) 571–579.

[122] R. François, S. Laurens, F. Deby, 1 - steel corrosion in reinforced concrete, in: R. François, S. Laurens, F. Deby (Eds.), Corrosion and its Consequences for Reinforced Concrete Structures, Elsevier, 2018, pp. 1–41. URL: https://www.sciencedirect.com/science/article/pii/B9781785482342500019. doi:https://doi.org/10.1016/B978-1-78548-234-2.50001-9.

[123] A. Poursaee, 2 - corrosion of steel in concrete structures, in: A. Poursaee (Ed.), Corrosion of Steel in Concrete Structures, Woodhead Publishing, Oxford, 2016, pp. 19–33. URL: https://www.sciencedirect.com/science/article/pii/B978178242381200002X. doi:https://doi.org/10.1016/B978-1-78242-381-2.00002-X.

[124] R. Rodrigues, S. Gaboreau, J. Gance, I. Ignatiadis, S. Betelu, Reinforced concrete structures: A review of corrosion mechanisms and advances in electrical methods for corrosion monitoring, Construction and Building Materials 269 (2021) 121240.

[125] Macrocell and microcell corrosion of steel in ordinary portland cement and high performance concretes, Cement and Concrete Research 36 (2006) 2098–2102.

[126] Z. P. Bažant, Physical model for steel corrosion in concrete sea structures theory, Journal of the Structural Division 105 (1979) 1137–1153.

[127] J. Broomfield, Corrosion of Steel in Concrete: Understanding, Investigation and Repair, Second Edition, Taylor & Francis, 2006. URL: https://books.google.it/books?id=kjTzl9NVHsQC.

[128] G. L. Cox, B. E. Roetheli, Effect of oxygen concentration on corrosion rates of steel and composition of corrosion products formed in oxygenated water, Industrial & Engineering Chemistry 23 (1931) 1012–1016.

[129] R. R. Hussain, T. Ishida, M. Wasim, Oxygen transport and corrosion of steel in concrete under varying concrete cover, w/c, and moisture, ACI Materials Journal 109 (2012).

[130] M. Raupach, Investigations on the influence of oxygen on corrosion of steel in concrete—part i, Materials and Structures 29 (1996) 174–184.

[131] M. Raupach, Investigations on the influence of oxygen on corrosion of steel in concrete—part 2, Materials and Structures 29 (1996) 226–232.

[132] C. Alonso, C. Andrade, J. González, Relation between resistivity and corrosion rate of reinforcements in carbonated mortar made with several cement types, Cement and Concrete Research 18 (1988) 687–698.

[133] C. Andrade, C. Alonso, A. M. García, Oxygen availability in the corrosion of reinforcements, Advances in Cement Research 3 (1990) 127–132.

[134] G. R. Irwin, Analysis of Stresses and Strains Near the End of a Crack Traversing a Plate, J. Appl. Mech. (1957).

[135] T. Anderson, T. Anderson, Fracture Mechanics: Fundamentals and Applications, Third Edition, Taylor & Francis, 2005. URL: https://books.google.it/books?id=MxrtsC-ZooQC.

[136] G. A. Maugin, The Thermomechanics of Plasticity and Fracture, Cambridge Texts in Applied Mathematics, Cambridge University Press, 1992. doi:10.1017/CBO9781139172400.

[137] E. Gdoutos, Fracture Mechanics Criteria and Applications, Engineering Applications of Fracture Mechanics, Springer Netherlands, 1990. URL: https://books.google.it/books?id=XPz2xFJP6eUC.

[138] L. O. A. Affonso, 4 - ductile and brittle fractures, in: L. O. A. Affonso (Ed.), Machinery Failure Analysis Handbook, Gulf Publishing Company, 2006, pp. 33–42. URL: https://www.sciencedirect.com/science/article/pii/B9781933762081500094. doi:https://doi.org/10.1016/B978-1-933762-08-1.50009-4.

[139] S. Freiman, J. Mecholsky, The Fracture of Brittle Materials: Testing and Analysis, Wiley, 2012. URL: https://books.google.it/books?id=5wgqwFCS8nMC.

[140] P. Thomason, Ductile Fracture of Metals, Pergamon Press, 1990. URL: https://books.google.it/books?id=Sw1SAAAAMAAJ.

[141] J. Rice, D. Tracey, Computational fracture mechanics, in: S. J. FENVES, N. PERRONE, A. R. ROBINSON, W. C. SCHNOBRICH (Eds.), Numerical and Computer Methods in Structural Mechanics, Academic Press, 1973, pp. 585–623. URL: https://www.sciencedirect.com/science/article/pii/B9780122532504500312. doi:https://doi.org/10.1016/B978-0-12-253250-4.50031-2.

[142] H. Liebowitz, J. Sandhu, J. Lee, F. Menandro, Computational fracture mechanics: Research and application, Engineering Fracture Mechanics 50 (1995) 653–670.

[143] M. Aliabadi, D. Rooke, Numerical Fracture Mechanics, Solid Mechanics and Its Applications, Springer Netherlands, 1991. URL: https://books.google.it/books?id=GNxETacuKtUC.

[144] P. Dechaumphai, S. Phongthanapanich, T. Sricharoenchai, Combined delaunay triangulation and adaptive finite element method for crack growth analysis, Acta Mechanica Sinica 19 (2003).

[145] A. Trädegård, F. Nilsson, S. Östlund, Fem-remeshing technique applied to crack growth problems, Computer Methods in Applied Mechanics and Engineering 160 (1998) 115–131.

[146] N. Moës, J. Dolbow, T. Belytschko, A finite element method for crack growth without remeshing, International Journal for Numerical Methods in Engineering 46 (????) 131–150.

[147] I. S. Aranson, V. A. Kalatsky, V. M. Vinokur, Continuum field description of crack propagation, Phys. Rev. Lett. 85 (2000) 118–121.

[148] B. Bourdin, G. A. Francfort, J.-J. Marigo, The variational approach to fracture, J. Elasticity 91 (2008) 5–148.

[149] R. de Borst, C. V. Verhoosel, Gradient damage vs phase-field approaches for fracture: Similarities and differences, Computer Methods in Applied Mechanics and Engineering 312 (2016) 78–94. Phase Field Approaches to Fracture.

[150] D. Dugdale, Yielding of steel sheets containing slits, J. Mech. Phys. Solids 8 (1960) 100–108.

[151] G. I. Barenblatt, The mathematical theory of equilibrium cracks in brittle fracture, in: Advances in Applied Mechanics, Vol. 7, Academic Press, New York, 1962, pp. 55–129.

[152] G. A. Francfort, J.-J. Marigo, Revisiting brittle fracture as an energy minimization problem, J. Mech. Phys. Solids 46 (1998) 1319–1342.

[153] S. Silling, Reformulation of elasticity theory for discontinuities and long-range forces, Journal of the Mechanics and Physics of Solids 48 (2000) 175–209.

[154] T. Li, Gradient-damage modeling of dynamic brittle fracture : variational principles and numerical simulations, Ph.D. thesis, 2016. URL: http://www.theses.fr/2016SACLX042, thèse de doctorat dirigée par Marigo, Jean-Jacques Mécanique des solides Université Paris-Saclay (ComUE) 2016.

[155] L. Evans, R. Gariepy, Measure Theory and Fine Properties of Functions, Revised Edition, 1st ed., Chapman and Hall/CRC, 2015. doi:https://doi.org/10.1201/b18333.

[156] B. Bourdin, G. A. Francfort, J.-J. Marigo, Numerical experiments in revisited brittle fracture, J. Mech. Phys. Solids 48 (2000) 797–826.

[157] E. Tanné, T. Li, B. Bourdin, J.-J. Marigo, C. Maurini, Crack nucleation in variational phase-field models of brittle fracture, Journal of the Mechanics and Physics of Solids 110 (2018) 80 – 99.

[158] K. Pham, H. Amor, J.-J. Marigo, C. Maurini, Gradient damage models and their use to approximate brittle fracture, International Journal of Damage Mechanics 20 (2011) 618–652.

[159] C. Miehe, F. Welschinger, M. Hofacker, Thermodynamically consistent phase-field models of fracture: Variational principles and multi-field fe implementations, International Journal for Numerical Methods in Engineering 83 (2010) 1273–1311.

[160] J.-Y. Wu, V. P. Nguyen, H. Zhou, Y. Huang, A variationally consistent phase-field anisotropic damage model for fracture, Computer Methods in Applied Mechanics and Engineering 358 (2020) 112629.

[161] J.-J. Marigo, C. Maurini, K. Pham, An overview of the modelling of fracture by gradient damage models, Meccanica 51 (2016).

[162] F. Freddi, Fracture energy in phase field models, Mechanics Research Communications 96 (2019) 29 – 36.

[163] F. Freddi, L. Mingazzi, Mesh refinement procedures for the phase field approach to brittle fracture, Computer Methods in Applied Mechanics and Engineering 388 (2022) 114214.

[164] M. de Jong, W. Chen, T. Angsten, A. Jain, R. Notestine, A. Gamst, M. Sluiter, C. Krishna Ande, S. van der Zwaag, J. J. Plata, C. Toher, S. Curtarolo, G. Ceder, K. A. Persson, M. Asta, Charting the complete elastic properties of inorganic crystalline compounds, Scientific Data 2 (2015).

[165] Z. Zhang, M. Thiery, V. Baroghel-Bouny, Numerical modelling of moisture transfers with hysteresis within cementitious materials: Verification and investigation of the effects of repeated wetting–drying boundary conditions, Cement and Concrete Research 68 (2015) 10–23.

[166] R. Montoya, V. Nagel, Capillary water absorption and chloride transport into mortar samples: A finite element analysis, Frontiers in Materials 7 (2020).

[167] H. Huang, G. Ye, K. Breugel, Numerical simulation on moisture transport in cracked cement-based materials in view of self-healing of crack, Journal of Wuhan University of Technology-Mater Sci Ed 25 (2010) 1077–1081.

[168] J. Bao, R. Zheng, J. Wei, P. Zhang, S. Xue, Z. Liu, Numerical and experimental investigation of coupled capillary suction and chloride penetration in unsaturated concrete under cyclic drying-wetting condition, Journal of Building Engineering 51 (2022) 104273.

[169] O. B. Isgor, W. J. Weiss, A nearly self-sufficient framework for modelling reactive-transport processes in concrete, Materials and Structures 52 (2018).

[170] C.-Y. Kim, J.-K. Kim, Numerical analysis of localized steel corrosion in concrete, Construction and Building Materials 22 (2008) 1129–1136.

[171] C. Cao, M. M. Cheung, Non-uniform rust expansion for chloride-induced pitting corrosion in rc structures, Construction and Building Materials 51 (2014) 75–81.

[172] Numerical simulation of electrochemical mechanism of steel rebar corrosion in concrete under natural climate with time-varying temperature and humidity, Construction and Building Materials 306 (2021) 124873.

[173] L. Berto, P. Simioni, A. Saetta, Numerical modelling of bond behaviour in rc structures affected by reinforcement corrosion, Engineering Structures 30 (2008) 1375–1385.

[174] M. J. Molina, M. C. Alonso, C. A. Perdrix, Cover cracking as a function of rebar corrosion: Part 2—numerical model, Materials and Structures 26 (1993).

[175] A. Jamali, U. Angst, B. Adey, B. Elsener, Modeling of corrosion-induced concrete cover cracking: A critical analysis, Construction and Building Materials 42 (2013) 225–237.

[176] J. Zhao, Z. Chen, J. Mehrmashhadi, F. Bobaru, A stochastic multiscale peridynamic model for corrosion-induced fracture in reinforced concrete, Engineering Fracture Mechanics 229 (2020) 106969.

[177] Y. Zhang, R. K. L. Su, Corner cracking model for non-uniform corrosion-caused deterioration of concrete covers, Construction and Building Materials 234 (2020) 117410.

[178] T.-T. Nguyen, D. Waldmann, T. Q. Bui, Phase field simulation of early-age fracture in cement-based materials, International Journal of Solids and Structures 191-192 (2020) 157–172.

[179] F. Freddi, L. Mingazzi, Phase-field simulations of cover cracking in corroded rc beams, Procedia Structural Integrity 33 (2021) 371–384. 26th International Conference on Fracture and Structural Integrity.

[180] X. Fang, Z. Pan, A. Chen, Phase field modeling of concrete cracking for non-uniform corrosion of rebar, Theoretical and Applied Fracture Mechanics 121 (2022) 103517.

[181] T. Hughes, The Finite Element Method: Linear Static and Dynamic Finite Element Analysis, Dover Civil and Mechanical Engineering, Dover Publications, 2000. URL: https://books.google.it/books?id=yarmSc7ULRsC.

[182] A. Quarteroni, Numerical Models for Differential Problems, MS&A, Springer Milan, 2010. URL: https://books.google.it/books?id=0gCRhwrnEO4C.

[183] A. Quarteroni, R. Sacco, F. Saleri, Numerical Mathematics, Texts in Applied Mathematics, Springer, 2007. URL: https://books.google.it/books?id=Y7grAAAAYAAJ.

[184] W. Hundsdorfer, J. Verwer, Numerical Solution of Time-Dependent Advection-Diffusion-Reaction Equations, Springer Series in Computational Mathematics, Springer Berlin Heidelberg, 2010. URL: https://books.google.it/books?id=l5kEkgAACAAJ.

[185] D. Arndt, W. Bangerth, D. Davydov, T. Heister, L. Heltai, M. Kronbichler, M. Maier, J.-P. Pelteret, B. Turcksin, D. Wells, The deal.ii finite element library: Design, features, and insights, Computers & Mathematics with Applications 81 (2021) 407–422. Development and Application of Open-source Software for Problems with Numerical PDEs.

[186] W. Bangerth, R. Hartmann, G. Kanschat, Deal.ii—a general-purpose object-oriented finite element library, ACM Trans. Math. Softw. 33 (2007) 24–es.

[187] P. Farrell, C. Maurini, Linear and nonlinear solvers for variational phase-field models of brittle fracture, International Journal for Numerical Methods in Engineering 109 (2017) 648–667. Nme.5300.

[188] C. Miehe, M. Hofacker, F. Welschinger, A phase field model for rate-independent crack propagation: Robust algorithmic implementation based on operator splits, Computer Methods in Applied Mechanics and Engineering 199 (2010) 2765–2778.

[189] L. De Lorenzis, T. Gerasimov, Numerical Implementation of Phase-Field Models of Brittle Fracture, Springer International Publishing, Cham, 2020, pp. 75–101.

[190] T. Gerasimov, L. D. Lorenzis, On penalization in variational phase-field models of brittle fracture, Computer Methods in Applied Mechanics and Engineering 354 (2019) 990–1026.

[191] F. Freddi, L. Mingazzi, A fenics implementation of the phase field method for quasi-static brittle fracture with adaptive refinement, Submitted for review at: Applications in Engineering Science (2023).

[192] S. Balay, S. Abhyankar, M. F. Adams, J. Brown, P. Brune, K. Buschelman, L. Dalcin, A. Dener, V. Eijkhout, W. D. Gropp, D. Kaushik, M. G. Knepley, D. A. May, L. C. McInnes, R. T. Mills, T. Munson, K. Rupp, P. Sanan, B. F. Smith, S. Zampini, H. Zhang, H. Zhang, PETSc Web page, 2018. URL: http://www.mcs.anl.gov/petsc.

[193] Q. Huang, Z. Jiang, X. Gu, W. Zhang, B. Guo, Numerical simulation of moisture transport in concrete based on a pore size distribution model, Cement and Concrete Research 67 (2015) 31–43.

[194] A. D. M. Arachchige, Influence of cement content on corrosion resistance, Proceedings of the Institution of Civil Engineers - Construction Materials 161 (2008) 31–39.

[195] V. G. Papadakis, C. G. Vayenas, M. N. Fardis, A reaction engineering approach to the problem of concrete carbonation, AIChE Journal 35 (1989) 1639–1650.

[196] D. Darwin, S. Barham, R. Kozul, S. Luan, Fracture energy of high-strength concrete, Aci Materials Journal 98 (2001) 410–417.

[197] J. Choo, W. Sun, Cracking and damage from crystallization in pores: Coupled chemo-hydro-mechanics and phase-field modeling, Computer Methods in Applied Mechanics and Engineering 335 (2018) 347–379.

[198] E. Korec, M. Jirásek, H. Wong, E. Martínez-Pañeda, A phase-field chemo-mechanical model for corrosion-induced cracking in reinforced concrete, Submitted to Construction and Building Materials (2023).